Reports on Progress in Physics

REVIEW

Review: knots and other new topological effects in liquid crystals and colloids

To cite this article: Ivan I Smalyukh 2020 *Rep. Prog. Phys.* **83** 106601

IOP Publishing Reports on Progress in Physics
Rep. Prog. Phys. **83** (2020) 106601 (46pp) https://doi.org/10.1088/1361-6633/abaa39

Review

Review: knots and other new topological effects in liquid crystals and colloids

Ivan I Smalyukh

Department of Physics, Department of Electrical, Computer and Energy Engineering, Materials Science and Engineering Program and Soft Materials Research Center, University of Colorado, Boulder, CO 80309, United States of America
Renewable and Sustainable Energy Institute, National Renewable Energy Laboratory and University of Colorado, Boulder, CO 80309, United States of America

E-mail: ivan.smalyukh@colorado.edu

Received 16 January 2020, revised 23 June 2020
Accepted for publication 28 July 2020
Published 8 September 2020

Abstract

Humankind has been obsessed with knots in religion, culture and daily life for millennia, while physicists like Gauss, Kelvin and Maxwell already involved them in models centuries ago. Nowadays, colloidal particles can be fabricated to have shapes of knots and links with arbitrary complexity. In liquid crystals, closed loops of singular vortex lines can be knotted by using colloidal particles and laser tweezers, as well as by confining nematic fluids into micrometer-sized droplets with complex topology. Knotted and linked colloidal particles induce knots and links of singular defects, which can be interlinked (or not) with colloidal particle knots, revealing the diversity of interactions between topologies of knotted fields and topologically nontrivial surfaces of colloidal objects. Even more diverse knotted structures emerge in nonsingular molecular alignment and magnetization fields in liquid crystals and colloidal ferromagnets. The topological solitons include hopfions, skyrmions, heliknotons, torons and other spatially localized continuous structures, which are classified based on homotopy theory, characterized by integer-valued topological invariants and often contain knotted or linked preimages, nonsingular regions of space corresponding to single points of the order parameter space. A zoo of topological solitons in liquid crystals, colloids and ferromagnets promises new breeds of information displays and a plethora of data storage, electro-optic and photonic applications. Their particle-like collective dynamics echoes coherent motions in active matter, ranging from crowds of people to schools of fish. This review discusses the state of the art in the field, as well as highlights recent developments and open questions in physics of knotted soft matter. We systematically overview knotted field configurations, the allowed transformations between them, their physical stability and how one can use one form of knotted fields to model, create and imprint other forms. The large variety of symmetries accessible to liquid crystals and colloids offer insights into stability, transformation and emergent dynamics of fully nonsingular and singular knotted fields of fundamental and applied importance. The common thread of this review is the ability to experimentally visualize these knots in real space. The review concludes with a discussion of how the studies of knots in liquid crystals and colloids can offer insights into topologically related structures in other branches of physics, with answers to many open questions, as well as how these experimentally observable knots hold a strong potential for providing new inspirations to the mathematical knot theory.

Keywords: liquid crystal, topological soliton, colloids, knotted fields, singular defect, nematic, self-assembly

(Some figures may appear in colour only in the online journal)

1. Introduction

Topological concepts are currently at the research frontier of modern condensed matter physics, with the exciting recent developments promising to revolutionize the future of many technologies, ranging from quantum computing to pre-engineered mechanics of materials [1, 2]. Although topological knot-related ideas are found in early works by Gauss, Kelvin, Tait and Maxwell [3–7], it is only recently that the concepts of topology have been successful in explaining entirely new types of physical behavior of condensed matter systems [1, 2], including phenomena that cannot be interpreted otherwise. Various types of knots are studied in practically all fields of physics [1–11]. The mathematical knot theory, once inspired by early models in physics [3], has become a major branch of topology with connections to statistical mechanics, models of exotic states in Bose–Einstein condensates, theories in elementary particle and nuclear physics, quantum field theory, quantum computing, solid-state physics and many other exciting frontiers of physics research [8–11]. The knots and links in these theories are beautiful mathematical constructs that, however, typically do not manifest themselves as physical objects accessible to experiments. This review concerns the studies of physical knots in condensed matter systems such as liquid crystals (LCs) and colloids [12–15]—ones that exist in the three-dimensional (3D) space of these ubiquitous soft materials, that can be manipulated by laser tweezers and that can be directly observed through a microscope.

Recognizing some of the key milestones in understanding the role of topology in physical behavior, the 2016 Nobel prize was awarded for theoretical discoveries of topological phase transitions and topological phases of matter [16–18], where many of the original breakthroughs resulted from considering two-dimensional (2D) systems. The situation is even more complex in 3D, where various knot-like structures can be supported, localized spatially and stabilized energetically, including both knotted filaments (vortex lines/defects/singularities) and knotted nonsingular textures such as skyrmions and hopfions [6–11]. Topological solitons are well studied in theoretical models of high-energy physics [6, 7] aiming to describe the behavior of fundamental particles and atomic nuclei. This review considers such structures in ordered soft condensed matter systems, which can be realized and characterized in detail experimentally, like in the cases of LCs and colloids. Although quantum phenomena and hard condensed matter systems received much of the recent attention in applying topology-related ideas [1], potentially an even greater playground for deploying topological concepts exists in soft condensed matter. While topological effects in soft matter encompass a much broader spectrum of phenomena [2, 19, 20], here we focus on knotted structures of the order parameter fields and their interaction with topologically nontrivial surfaces in LCs and colloids.

Historically, knotted fields in modern physics emerged in classical and quantum field theories [6, 7, 21, 22] and in branches ranging from optics to chemistry, materials science, particle physics, fluid mechanics and cosmology [19, 20, 23–32]. Recently, knotted fields found many experimental and theoretical embodiments, including both nonsingular solitons and knotted vortices [32–48]. Knots often arise in electromagnetic fields [28, 37]. For example, researchers found solutions to Maxwell's equations with knotted and linked field lines [37]. Recent developments in optical holography and microlithography make it possible to structure the flow of light in free space, whereas the rich vectorial and phase structure of sculpted light allows for different kinds of knotted and linked light beams. For example, knotted optical vortices have been embedded into laser beams by Dennis and coworkers [28]. Understanding the knots which can be embedded in holograms [28] has even led to the new classes of knots now being studied in the knot theory [8–11]. Moreover, unlike in various material systems [24, 26], knot structures in electromagnetic fields could be hosted in free space, therefore arising in completely linear systems, including knotted field lines, optical vortices and knotted textures in polarization [37, 38]. Numerical studies [19, 20] have revealed characteristic cascades of fluid knot topologies, and explicit forms of knotted flow fields with tunable helicity have been shown [39]. At the same time, Irvine and collaborators developed techniques [19, 20, 27] to embed knotted vortex filaments in fluids experimentally. In Bose–Einstein condensates, knotted topological solitons were realized as the initial 'imprinted' states that then decayed, revealing interesting dynamics [40, 41]. In magnetic hard condensed matter systems, knot solitons could be stabilized as free-energy minima in thin films and discs of non-centrosymmetric magnets [42], as well as in the bulk of chiral materials with crystalline anisotropy [43] or helicoidal structures [44]. Studies of various knots and related topological effects are highly interdisciplinary in nature, and equally important for understanding synthetic macromolecules and biopolymers [45–47] and quantum material systems [48].

This brief and non-exhaustive overview of exciting new developments in studies of knots shows how the manifestations of knotted fields penetrate different branches of science and how theoretical and experimental explorations can now go hand-in-hand in these systems, something that was far from possible in the past, when knots were mainly a subject of theoretical curiosity. The knots that are part of this review are realized in soft condensed matter media [12–15], which make them significantly more experimentally accessible, even though these systems can exhibit an exceptionally broad range of accessible symmetries and degrees of freedom at the same

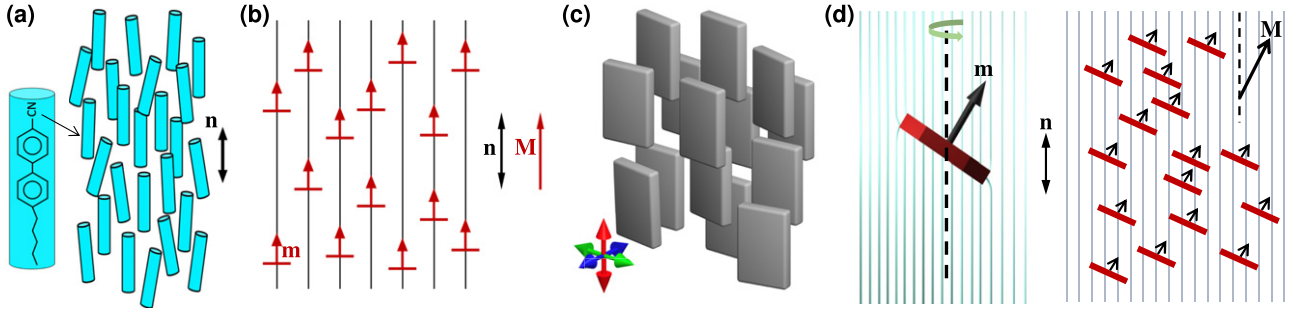

Figure 1. Orientationally ordered soft matter systems. (a) A schematic of a uniaxial LC made of rod-like molecular mesogens. (b) Dispersion of monodomain magnetic colloidal nanoplates with magnetic moments **m** and macroscopic magnetization **M** aligning with **n** (black lines), effectively 'vectorizing' the nonpolar director field **n**(**r**) by **M**(**r**) by selecting one of the directions parallel to it. (c) Biaxial nematic phase with orthorhombic D_{2h} point group symmetry characterized by three mutually perpendicular nonpolar directors (red, green and blue double arrows). (d) A schematic of a ferromagnetic hexagonal nanoplate in a nematic host with its magnetic moment tilted away from the LC ordering direction (left) and biaxial ferromagnetic LC colloids with magnetization **M** tilted with respect to the director **n** (right), forming a monoclinic biaxial ferromagnetic LC.

time. While focusing on various knotted fields in soft matter, the article draws the attention of the readers to related recent developments in other branches of physics, as well as emphasizes how soft matter media like colloids and LCs can serve as model systems to predict topologically related structures in other branches of science.

What is soft condensed matter? Nobel laureate de Gennes defined soft matter [12, 49] as a broad combination of systems with strong response functions, which are capable of strong responses to weak external stimuli. These strong responses originate largely from the fact that the competing, behavior-defining interactions between the constituent building blocks of soft matter are weak and comparable in strength to thermal fluctuations [13]. Another defining feature of soft matter is that it often combines fluidity and ordering [12–15], with a very broad range of intermediate mesophases (phases in-between the fully ordered crystalline and disordered fluid states) with the order parameter fields possibly being scalar, vectorial and tensorial. LCs and colloids are classic examples of soft matter [12–15] and will be the focus of this review. The soft matter systems offer the possibility of laboratory realization and modeling of effects that are typically hard to probe. For example, order–disorder transitions in nematic LCs allowed for probing the Kibble mechanism of cosmic string dynamics in the models of early Universe cosmology [50], whereas colloids were used to model and probe the dynamics of dislocation defects and glass formation in atomic and molecular systems [14, 51, 52]. In a similar way, the power of soft matter can be extended to modeling the topology of singular and solitonic knotted fields. LC colloids, where molecular LCs serve as the host medium for colloidal particles [53–55], are of particular interest from this standpoint as they combine the complexity of molecular and colloidal LC systems. Figure 1 shows examples of soft matter systems with vectorial and different tensorial order parameters, including uniaxial nonpolar nematic (figure 1(a)) and ferromagnetic (figure 1(b)) LCs, as well as orthorhombic (figure 1(c)) and polar non-orthorhombic ferromagnetic (figure 1(d)) biaxial LCs. What kinds of knots can be realized in such fields? The answer, which can be experimentally tested using LCs and colloids, has a fundamental importance spanning well beyond condensed matter because topology and free energy potentials can be mapped to that of related problems in other physical systems. Having soft matter systems as host media with facile responses to external stimuli [12, 13] for these knotted fields also enables various types of control by external fields, boundary conditions, light and so on. The main goal of this review is to describe the recent progress in realizing zoos of knotted fields in LCs and colloids, as well as to emphasize how this can aid in similar explorations in other branches of physics.

Below the review article proceeds with a brief historic overview (section 2), which is followed by a discussion of general classifications of different types of knots and links and topologically nontrivial field configurations (section 3). The article then continues by overviewing the recent progress in studies of various topologically nontrivial structures in nematic colloids and drops, where singular defects are commonplace (section 4). The structure, topology and self-assembly of solitonic knots in LC and colloidal soft matter systems are discussed in section 5. Section 6 is devoted to emergent out-of-equilibrium behavior of such knotted fields and particle-like topological solitons. The review article then concludes with a brief discussion of open questions, opportunities and perspectives in this research area (section 7).

2. Historic remarks

Humankind has long been fascinated with knots and has used them for both practical and spiritual needs throughout history [4, 56–58]. Over the last several millennia, knots often served as decorations, signs, religious symbols and, in a more prosaic daily life, just as the ubiquitous means to hold things together (figure 2) [4, 8, 57, 58]. The diversity of knots allowed them to be used in rather different contexts, ranging from recording information on ropes and strings to writing, boat sailing, climbing, netting, textile manufacturing and so on [4, 57, 58], and of course to tie shoelaces. As decorations and symbols, knots are important components of Tibetan, Roman, Celtic, Byzantine, Coptic, Islamic, Kievan Rus', Ethiopian, Chinese and Indian cultures, among many others (figure 2) [4, 56, 57].

For example, the so-called eternal knot (also known as the 'endless' knot) is a symbol of the ultimate unity of everything, one of the Eight Auspicious Signs endemic to Hinduism, Jainism and Buddhism religions [4, 56, 57]. In different cultures, many other types of knots were widely used to symbolize love, family, eternity, union, weddings and so on [4, 57]. These special cultural and religious uses of knots as symbols coexisted with their widespread uses for practical and, recently, scientific needs. For example, after joining the ends, the common overhand knot becomes a trefoil knot (figures 2(a) and (b)), the simplest nontrivial knot in the mathematical knot table that is also found in the Celtic Book of Kells (figure 2(c)) and nowadays is often used for the identification with Celtic culture. This very same trefoil knot is also a symbol of the Trinity in Christianity, and different variants of it played important roles in Japanese, Korean and Tibetan cultures [4]. The Solomon link and Borromean rings (figures 2(d) and (e)) are two more out of many other examples of knots that are important in the mathematical and physics theories but also have a history of being used as important symbols [4]. While being part of Chinese history for several millennia, knots like the one shown in figure 2(f) are also widely used as decorations in East Asian countries nowadays. The Gordian Knot legend is an example showing how, historically, knots could be associated with challenging problems and nontrivial solutions to them, in this case involving Alexander the Great in 333 BC [4, 57]. Knotty problems are associated with challenging issues not just in different branches of science (where knots actually often materialize in polymer chains, molecular structures, field configurations and many other embodiments), but also in politics, various legal practices, relations and so on [4].

An important branch of modern mathematics is knot theory, which also has an interesting history [3–8]. In 1833, Carl Friedrich Gauss introduced the linking integral for computing the linking number of two knots and, together with his student Johann Benedict Listing, did important early studies of knots from a mathematical viewpoint [4]. A very strong interest in studies of knots was sparked by early models of vortex atoms developed slightly later in Scotland, where Sir William Thomson (Lord Kelvin) had an interesting hypothesis that atoms were knots of swirling vortices [3–8]. Long before even the very existence of atoms was widely accepted, Kelvin and his colleagues in Edinburgh (among whom the most prominent ones were James Clerk Maxwell and Peter Guthrie Tait) classified various closed-loop knots into tables that they were hoping could match the periodic table of chemical elements, where different elements would correspond to topologically distinct knots [3–5]. Experimentally, Tait and Maxwell created smoke rings and links as simple model systems accessible at that time [3–6]. The researchers even hoped that the systematic classification of all possible knots would explain how atoms absorb and emit light [3–5]. Despite failing to explain the nature of atoms, these early works of Kelvin, Tait and Maxwell became a nucleus for the development of the modern mathematical knot theory [4, 8], an important foundation for understanding various types of knots that eventually emerged in different branches of physics, biology, chemistry and cosmology [3–11]. Throughout history, cross-pollinating

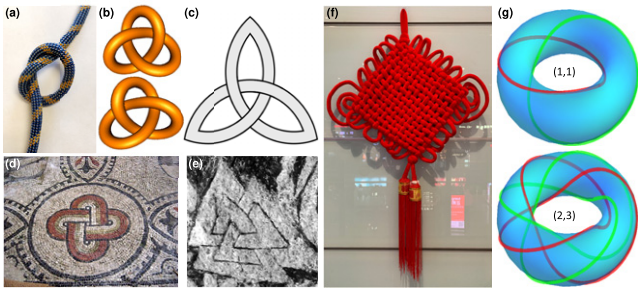

Figure 2. Knots in history, culture and science. (a) A common overhand knot. (b) A trefoil knot in two embodiments of opposite handedness, which can be obtained by connecting the ends of the overhand knot; these knots were generated using the KnotPlot freeware (https://knotplot.com). (c) The symbol of interlaced triquetra [Madboy74/CC BY-SA (https://creativecommons.org/licenses/by-sa/4.0)] is a trefoil knot. (d) and (e) Ancient decorations in the forms of (d) the Solomon link (Aquileia, Basilica. Photo by Giovanni Dall'Orto) and (e) the Borromean link [Valknut detail from Stora Hammar stone. Adapted from https://en.wikipedia.org/wiki/Valknut. CC BY-SA 3.0 (https://creativecommons.org/licenses/by-sa/3.0)]. (f) Used for millennia in Chinese culture [6,8–11], knots are also very common decorations nowadays, with this Chinese knot decoration, for example, being commonplace in Beijing airport. (g) Many closed-loop mathematical knots belong to the class of torus knots and can be confined to surfaces of a torus; the examples provided here are the unknots (top) and trefoil knots (bottom) featuring different numbers of windings around the circular axis and axis of rotation of the torus provided in brackets. Note that the two unknots (top) and the two trefoil knots (bottom) shown by red and green colors in each case are further linked with each other while residing on the tori in each case, forming different two-component links.

connections between the knot theory and physics emerged many times. For example, inspired by Kelvin's model of atoms [59], Skyrme proposed a topological model of subatomic particles with different baryon numbers [21, 59, 60]. As another connection between the knot theory and physics, Ed Witten was awarded the Fields Medal partly for bringing new insights into the knot theory based on quantum physics [61]. Witten also established connections between the Skyrme model and quantum chromodynamics [60].

Another important concept that is a subject of this review, the soliton, also has important historic roots in 19th-century Scotland, where it was first observed in 1834 by John Scott Russell [62, 63]. A solitary wave called a 'soliton' is typically associated with a propagating self-reinforcing wave packet that persists for a long time. Such solitary waves have been observed in many branches of physics, with perhaps the other most known example beyond the solitons in fluid dynamics being the optical solitons that take the form of self-focusing, non-spreading laser beams that propagate without diverging due to nonlinear optical effects [62, 63]. From a more general standpoint, solitons are solutions of nonlinear partial differential equations describing different physical systems and they often have a topologically nontrivial nature, with the subclass of topological solitons often exhibiting various knotted structures in physical fields and order parameter spaces [7, 62, 63]. Such topological solitons in higher spatial dimensions can be stable and stationary in nature, or exhibit a host of different types of translational and rotational motions and other

dynamics. The topology-related ideas in studies of solitons were introduced by Skyrme [21], who was inspired by the works of Kelvin and Russell at the same time [7, 59], and these studies also relate to other physics concepts, such as instantons and singular topological defects.

Remarkably, ideas that knots in fields could emerge and behave like particles persistently recurred throughout history, with the knotted fields of Gauss in the early 1830s to Kelvin, Maxwell and Tait later in the 19th century, and Skyrme and Witten in the second half of the 20th century being just several particularly interesting examples [3–7]. With many roots in history, fundamental studies of knotted fields nowadays promise a means to realize new materials with pre-engineered properties that differ from those of naturally occurring ones, and they may provide new inspirations to the mathematical knot theory and physics models in many branches of science, well beyond condensed matter physics. This review article will show how knots in soft matter systems indeed behave like particles, resembling the behavior of atoms, molecules and other particles, being capable of forming crystals and even exhibiting active matter behavior.

3. Mathematical foundations

3.1. Diversity of knots and links

In exploring diverse manifestations of knots in physics it is important to systematically classify them. Starting from the times of Kelvin and Tait [6], this is done by creating tables of knots (figure 3), where distinct knots are labeled by knot properties, such as the crossing number [4]. In the most common Alexander–Briggs notation, each distinct knot is labeled by its crossing number (the minimum number of double points in the knot's planar projections). An additional subscript used in this notation is a numbering index for each knot of that crossing number (figure 3), though this subscript has no special significance because the order is arbitrary [4, 6]. For example, the simplest object of knot theory, the unknot, is labeled as 0_1, whereas the simplest knot distinct from the unknot, the trefoil knot, is denoted as 3_1 [3–6]. Similar notations classify multicomponent links of closed curves without common points (figure 4), including linked unknots and various interlaced knots within the 3D space [6]. A widely known subclass of knots are torus knots that (in one of their embodiments) fully reside on surfaces of tori (figure 2(g)), with the simplest of the torus knots again being the trefoil 3_1 knot (figure 2(b)) [6]. Each torus knot can be further uniquely specified by two integers p_T and q_T (figure 2(g)) [3, 4]. The notation $T(p_T,q_T)$ implies that the knot winds q_T times around a circle in the interior of the torus, and p_T times around its axis of rotational symmetry, though different notations are used as well. A $T(p_T,q_T)$ knot is equivalent to a $T(q_T,p_T)$ torus knot and the crossing number is found as $\min\{p_T(q_T-1), q_T(p_T-1)\}$, establishing the relation between the different notations and characteristics of torus knots. As an example, a trefoil knot in this notation can be labeled as $T(2,3)$ or $T(3,2)$ (figure 2(g)) [6]. Depending on a convention, the signs of p_T and q_T define the directions in which the strands of the knot wrap around the torus, where,

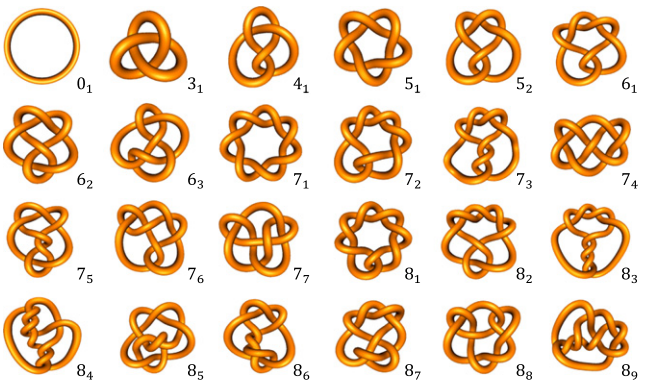

Figure 3. A table of knots. Only the first simplest 24 knots are shown [6], with their Alexander–Briggs notations given in the bottom-right of each knot. Knots were generated using the KnotPlot freeware (https://knotplot.com).

most commonly, $p_T q_T > 0$ corresponds to the right-handed knot configuration [6, 8].

Like knots, links can be distinguished by their crossing numbers [4, 8]. One way of classifying the links is the Rolfsen table of the prime links labeled as C^n_p by the crossing number C, the number of closed-loop components n and the order number p among the links with C crossings within the table (figure 4(a)) [6, 8]. Multicomponent unknots and knots can be interlaced with each other in much more nontrivial ways than just the direct linking. For example, a series of Brunnian links with three or more components can be inseparable from each other without a direct linking of each of the components (figure 4(b)) [6]. A widely known example is Borromean rings with six crossings, though similar inseparability of closed loops is achieved in other configurations of three or more components with different crossing numbers (figure 4(b)) [4, 8]. Similar to knots, a torus link is a multicomponent link geometrically situated on the surface of a torus and is realized when p_T and q_T are not relatively prime (figure 2(g)). Knots and links are chiral when they are not equivalent to their mirror images (figure 2(b)). On the other hand, an oriented knot that cannot be distinguished from its mirror image is an amphichiral (achiral) knot [3–6]. Therefore, knot's properties can be specified further and, overall, there are five types of knot symmetries defined by chirality and invertibility [4, 8] whose manifestations in material systems potentially could be related to the ordered host medium's symmetry. Torus knots are chiral (see the examples of trefoil knots in figure 2(b)) [3–6].

What are the different ways in which knots and links could manifest themselves in soft matter systems? Biopolymers, synthetic macromolecules, proteins, DNA and even small molecule strands can take the shapes of different knots and links [64–68], either because of the chemical design or because of the random-walk-like processes. Colloids can be shaped as unknots, knots and links [34, 35, 69–72]. Singular vortices in LCs can take the shapes of knots [33] and various solitonic defects can be knotted too [24, 32, 73], with knots and links even emerging in the topologically nontrivial states of the order parameter. These knots and links play an important role in defining physical behavior of soft matter systems because of various types of topological

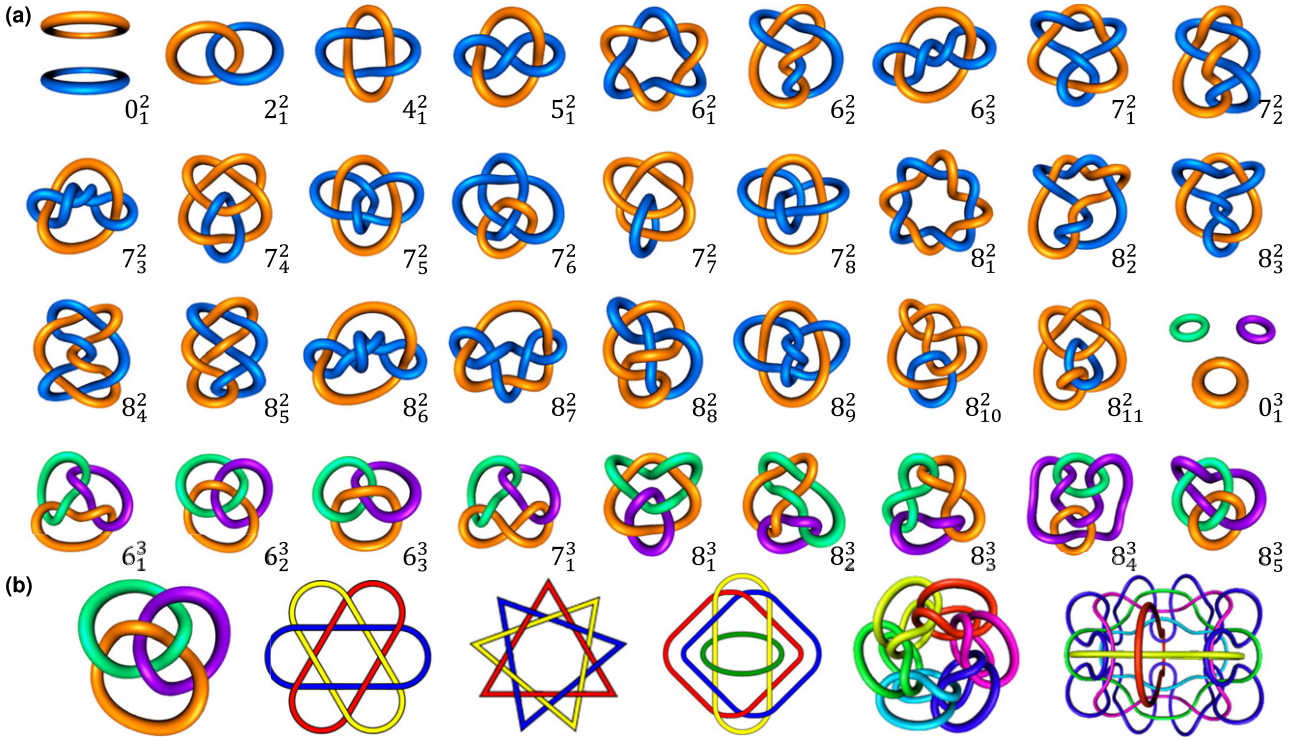

Figure 4. Multicomponent links. (a) A Rolfsen table of the first prime links, with the first 36 links shown along with the corresponding notations [6]. (b) Examples of Brunnian links with different numbers of components and crossing numbers, with the first being the three-component Borromean link. All links were generated using the KnotPlot freeware (https://knotplot.com).

protection associated with them. When creating knots on strings like in the case of shoelaces, such as the overhand knot in figure 2(a), we often intend undoing them at a later time. Such unknotting is possible by manipulating the loose ends of the string, but this would be impossible if the string were to be infinitely long or if its two ends were to be glued together to transform the overhand knot into a trefoil knot (figures 2(a) and (b)). All the knotted configurations shown in figures 3 and 4 cannot be unknotted or transformed one to another without cutting or gluing, similar to how one cannot inter-transform topologically distinct surfaces like a torus and a sphere. Throughout this review, we shall see examples of how such topological protection manifests itself when related to knotted topology of colloids and order parameter fields of various soft matter systems. Before we proceed, however, it is also useful to briefly review the homotopy theory [74].

3.2. Homotopy theory of topological solitons and singular defects

Topologically nontrivial field configurations can be of the singular type (singular topological defects), containing regions of physical space where the order parameter cannot be defined, or instead of the nonsingular type (topological solitons), within which the structure of the field is continuous everywhere, but it cannot be continuously morphed to a trivial uniform state without destroying the order or introducing singular defects. Much like (though not exhaustively) genus and Euler characteristics distinguish topologically distinct surfaces, various topological field configurations can be classified on the basis of mappings of these fields from the physical configuration spaces to the order parameter spaces (the manifolds of possible values of the order parameter) [74–76]. Typically, this is the mapping from spheres of various dimensions to the order parameter spaces that are often also spheres. Therefore, the homotopy groups of spheres classifying these mappings are the most common (figure 5) and are often utilized to label the different topologically distinct field configurations, though there are also other homotopy group examples relevant to LCs that will also be briefly discussed below in the review. Algebraic topology describes how such spheres of various dimensions can wrap around each other, which is systematically characterized by the homotopy groups that describe the structure of topological spaces (without considering the precise geometry) [6, 74]. In

	π_1	π_2	π_3	π_4
$\mathbb{S}^0$	0	0	0	0
$\mathbb{S}^1$	$\mathbb{Z}$	0	0	0
$\mathbb{S}^2$	0	$\mathbb{Z}$	$\mathbb{Z}$	$\mathbb{Z}_2$
$\mathbb{S}^3$	0	0	$\mathbb{Z}$	$\mathbb{Z}_2$
$\mathbb{S}^4$	0	0	0	$\mathbb{Z}$

Figure 5. Homotopy theory classification of singular and solitonic field configurations. The green, yellow and blue colors highlight different examples of topologically nontrivial field configurations discussed within this review, whereas the $\pi_3(\mathbb{S}^3) = \mathbb{Z}$ topological solitons (red) arise in high-energy and nuclear physics models of subatomic particles.

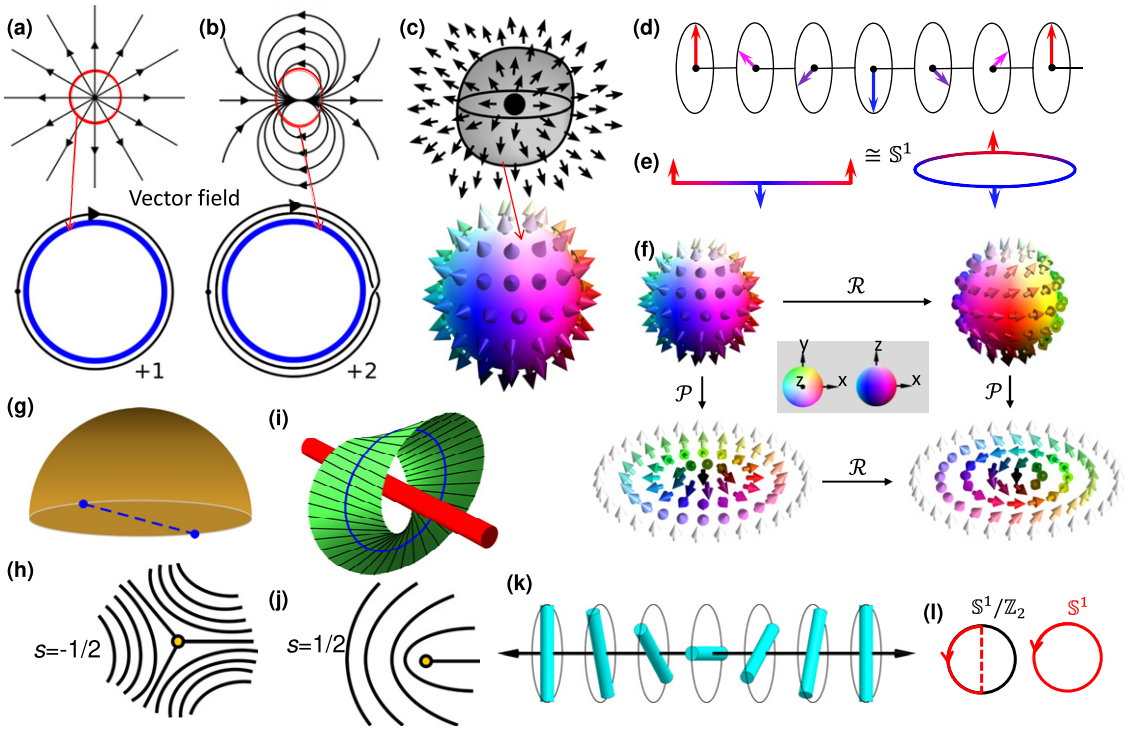

Figure 6. Topologically nontrivial structures of fields. (a) and (b) Examples of 2D $\pi_1(\mathbb{S}^1) = \mathbb{Z}$ singular defects classified by mapping the vector field from $\mathbb{S}^1$ surrounding the singularity to $\mathbb{S}^1$ order parameter space of vectors confined to a 2D plane, with the order parameter space covered once in (a) and twice in (b), yielding the corresponding winding numbers. (c) An elementary +1 radial point defect representing a family of point singularities with integer-valued hedgehog charges labeled as $\pi_2(\mathbb{S}^2) = \mathbb{Z}$. (d) An example of a $\pi_1(\mathbb{S}^1) = \mathbb{Z}$ topological soliton in the form of an elementary 1D solitonic wall with 360° unit vector rotation embedded in the uniform (vertical, pointing upwards) far-field background, which can be represented on $\mathbb{S}^1$, as shown in (e), where red–blue colors on $\mathbb{R}^1$ and $\mathbb{S}^1$ correlate with and depict vector orientations. (f) Skyrmions in $\mathbb{R}^2$ (bottom) can be mapped bijectively from field configurations in $\mathbb{S}^2$ (top) through stereographic projections ($\mathcal{P}$). The Neel-type (bottom-left) and Bloch-type (bottom-right) 2D skyrmions are related by a smooth rotation ($\mathcal{R}$) of vectors. The vector orientations are shown as arrows colored according to the corresponding points on the target $\mathbb{S}^2$ (inset). (Part (f) is reproduced with permission from [79]). (g) A schematic of the $\mathbb{S}^2/\mathbb{Z}_2$ order parameter space, with the diametrically opposite points of the circular base identified. (h)–(j) Half-integer defects in nonpolar 2D $\mathbf{n}(\mathbf{r})$, including wedge disclinations (h) and (j) that in 2D would be characterized by opposite $s = \pm 1/2$ winding numbers, and a twist disclination (i). In $\mathbb{R}^3$, there is only one type of topologically distinct disclinations different from a uniform state, with the topologically distinct states labeled $\pi_1(\mathbb{S}^2/\mathbb{Z}_2) = \mathbb{Z}_2$; local structures of defect lines like the ones shown in (h)–(j) can smoothly inter-transform one into another in 3D and correspond to a single, topologically equivalent state. (k) A twisted wall with 180° rotation of nonpolar $\mathbf{n}(\mathbf{r})$ embedded in a uniform background can be compactified on $\mathbb{S}^1/\mathbb{Z}_2 \cong \mathbb{S}^1$. (l) The mapped director field of the twisted wall winds around the order parameter space $\mathbb{S}^1/\mathbb{Z}_2$ once; since $\mathbb{S}^1/\mathbb{Z}_2 \cong \mathbb{S}^1$, 1D LC solitons are classified by $\pi_1(\mathbb{S}^1) = \mathbb{Z}$.

studies of topological solitons and singular defects, such classifications provide valuable means of summarizing topologically different structures in the order parameter fields, although the existence of a nontrivial element in the homotopy class does not guarantee their energetic stability or experimental observation [74]. The n-dimensional spheres (n-spheres, denoted as $\mathbb{S}^n$) are defined as sets of points equidistant from the origin in $n + 1$ dimension, with an $\mathbb{S}^1$ circle being the 1-sphere embedded in 2D space ($\mathbb{R}^2$), $\mathbb{S}^2$ being an ordinary sphere embedded in 3D space ($\mathbb{R}^3$) and $\mathbb{S}^0$ being a 0-sphere embedded in $\mathbb{R}^1$ that comprises two points equidistant from the origin in 1D, and so on [3–7, 77, 78]. The homotopy group labeled as $\pi_i(\mathbb{S}^n)$ is the ith homotopy group that enlists the topologically different maps from $\mathbb{S}^i$ into $\mathbb{S}^n$, where none of the distinct mappings can be continuously deformed to the other mappings (figure 5) [74–78]. Algebraic topology results are well established and depend on the integers i relative to n, with $\pi_i(\mathbb{S}^n) = 0$ for $i < n$ (figure 5), which means that the corresponding homotopy group is the trivial group [77, 78]. In mappings between spheres of the same dimension ($i = n$), $\pi_n(\mathbb{S}^n) = \mathbb{Z}$, so that the spheres can be wrapped around spheres an integer number of times for each map (figure 5). When $i > n$, a particularly interesting example of the mappings is called the Hopf fibration [77, 78] (figure 5), which wraps $\mathbb{S}^3$ around $\mathbb{S}^2$ an integer number of times, $\pi_3(\mathbb{S}^2) = \mathbb{Z}$. How can this abstract mathematical knowledge of mappings help with classifying topological defects in soft matter?

The procedures for utilizing homotopy theory for solitonic and singular defect field configurations differ slightly because of their different nature. Since the singular defects in fields are discontinuities in the form of walls, lines and points, with the order parameter varying continuously outside these singular regions, one can surround them with spheres of the corresponding dimensions (say $\mathbb{S}^1$ for line defects and $\mathbb{S}^2$ for point singularities) and characterize how the field, like the vector or director field, varies around these spheres (figure 6) [74–76]. The order parameter spaces often also take the form of spheres. For example, the order parameter space for unit vectors in 3D space $\mathbb{R}^3$ is $\mathbb{S}^2$ (describing all possible orientations of the unit vector), but it becomes $\mathbb{S}^1$ when these unit vectors are forced

to confine their orientations into a 2D plane $\mathbb{R}^2$ and becomes $\mathbb{S}^0$ when the unit vectors can only take orientations parallel or antiparallel to the positive direction in $\mathbb{R}^1$. Therefore, the topologically distinct singular defects in unit vector fields can be classified with the help of maps from the *i*-spheres surrounding them to *n*-spheres describing their order parameter spaces [74]. Some of the simplest examples are illustrated in figure 6. Just like one can wrap one circle around the other an integer number of times (imagine wrapping a closed-loop rubber band around a finger), the structure mapped from $\mathbb{S}^1$ around a singular defect in 2D can wrap the $\mathbb{S}^1$ order parameter circle an integer number of times, $\pi_1(\mathbb{S}^1) = \mathbb{Z}$, indicating that singular defects with integer winding numbers exist in this system (figures 6(a) and (b)). Also, the structures of a vector field mapped from $\mathbb{S}^2$ around a singular point defect in 3D can wrap the $\mathbb{S}^2$ order parameter sphere an integer number of times (figure 6(c)), $\pi_2(\mathbb{S}^2) = \mathbb{Z}$, again defining the charges of all possible singular point defects in this system (figure 6) [74–76]. On the other hand, the fact that $\pi_1(\mathbb{S}^2) = 0$ informs one that singular line defects in 3D unit vector fields are topologically unstable, so that they cannot be knotted or even exist because they can be smoothly morphed to a uniform topologically trivial state [74]. Likewise, since $\pi_2(\mathbb{S}^1) = 0$, one cannot form topologically nontrivial point defects when the unit vectors are forced to take orientations confined to a 2D plane [75].

What about nonsingular solitonic structures with different topologies? While they may seem to be rather different from singular defects, always having the field orientation well defined, they can be classified on the basis of the very same sphere-to-sphere maps (figure 5) [74–78]. In $\mathbb{R}^1$, a solitonic 360°-twist nonsingular wall in a unit vector field has the far-field vector pointing upwards, and, thus, this configuration space can be 'compactified' (by connecting the far-field regions of $\mathbb{R}^1$ with like-oriented unit vectors) into $\mathbb{S}^1$ (figures 6(d) and (e)) [7, 24, 79]. The topological class of the solitonic structures of this kind is then labeled by $\pi_1(\mathbb{S}^1) = \mathbb{Z}$, similar to the case of singular line defects for the 2D unit vector fields (figures 6(a), (b), (d) and (e)) [79]. The configuration space of solitonic topological structures embedded in the uniform far-field background in $\mathbb{R}^2$ can be compactified to $\mathbb{S}^2$ (e.g. by means of stereographic projection), so that the nontrivial result $\pi_2(\mathbb{S}^2) = \mathbb{Z}$ from algebraic topology (in addition to classifying singular point defects like the one shown in figure 6(c)) also informs us that all possible topologically nontrivial structures in this case are characterized by the integer-valued 2D skyrmion numbers (figure 6(f)) [80, 81]. Similarly, the configuration space in $\mathbb{R}^3$ with the uniform far field is compactified to $\mathbb{S}^3$ through a higher-dimensional analog of stereographic projection and the mathematical result from algebraic topology $\pi_3(\mathbb{S}^2) = \mathbb{Z}$ also informs us that the Hopf indices of 3D spatially localized solitons also take integer values [7].

Unit vector fields are not the only ones encountered in soft matter (figure 1), and, thus, the *n*-spheres cannot always represent the ground-state manifolds for the order parameters [74–77]. The LC unit director fields with nonpolar symmetry describe the average orientation of rod-like molecules, $\mathbf{n}(\mathbf{r}) \equiv -\mathbf{n}(\mathbf{r})$ (figure 1(a)). Because of the nonpolar nature, representing all orientations of $\mathbf{n}(\mathbf{r})$ on $\mathbb{S}^2$ requires only half the sphere and leaves diametrically opposite points non-distinguishable from each other (figure 6(g)) [74]. The order parameter space for $\mathbf{n}(\mathbf{r})$ is $\mathbb{S}^2/\mathbb{Z}_2 \equiv \mathbb{R}P^2$, a sphere with diametrically opposite points identified (figure 6(g)). One of the major differences when compared to unit vectors is that $\pi_1(\mathbb{S}^2/\mathbb{Z}_2) = \mathbb{Z}_2$, meaning that singular vortex lines (disclinations) can be stable in the 3D space of LCs [74, 75], though only one type of such defect lines can be realized that is topologically different from the uniform state. These defect lines can have different local structures when embedded in 3D samples, including that of wedge disclinations with opposite signs of winding numbers (figures 6(h) and (j)) (which are topologically distinct when realized in 2D) and twist disclinations (figure 6(i)). In 3D, however, the defect line structures shown in figures 6(h)–(j) can be smoothly morphed one to another within $\mathbb{R}^3$ and are therefore topologically the same, much like (though not exactly) the surfaces of a doughnut and of a coffee mug are characterized by the same value of genus $g = 1$ and (in one's imagination) can be morphed one into another without cutting or gluing [74]. In a similar way, unlike in vector fields, one can realize nonsingular twist domain walls with only 180° twist of nonpolar $\mathbf{n}(\mathbf{r})$ embedded in a uniform far-field background (figures 6(k) and (l)), which are labeled by $\pi_1(\mathbb{S}^1/\mathbb{Z}_2) \equiv \pi_1(\mathbb{S}^1) = \mathbb{Z}$ [79]. Solitonic structures that exist in lower dimensions can also be embedded in higher dimensions while being translationally invariant with respect to translations along them. For example, the $\pi_2(\mathbb{S}^2) = \mathbb{Z}$ solitons can be found as translationally invariant structures spanning $\mathbb{R}^3$ of LCs and magnets, either as individual spatially localized structures or periodic arrays [79]. When embedded in $\mathbb{R}^3$ in LC samples like glass cells of finite thickness, such solitons often terminate on $\pi_2(\mathbb{S}^2) = \mathbb{Z}$ point defects due to boundary conditions [79–82]. Similarly, translationally invariant solitonic walls $\pi_1(\mathbb{S}^1/\mathbb{Z}_2) = \mathbb{Z}$ are often embedded into finite-sized structures in 2D by singular defects of the same class $\pi_1(\mathbb{S}^1/\mathbb{Z}_2) = \mathbb{Z}$; in 3D samples with all 3D orientations of director allowed, such twist walls are described by $\pi_1(\mathbb{S}^2/\mathbb{Z}_2) = \mathbb{Z}$ and can be embedded into a uniform background by the $\pi_1(\mathbb{S}^2/\mathbb{Z}_2) = \mathbb{Z}$ disclinations, forming one type of the so-called 'cholesteric fingers' [79]. The examples above illustrate a more general rule for imbedding lower-dimensional solitonic structures into a uniform background in higher dimensions with the singular defects of a homotopy class matching that of solitons [79]. The soft matter topological solitons and defects have many topological counterparts in other branches of physics, ranging from elementary particle physics to cosmology. For example, $\pi_3(\mathbb{S}^3) = \mathbb{Z}$ Skyrme solitons (figure 5) are used to model subatomic particles in high-energy and nuclear physics [7, 21], which is also the reason for often referring to their $\pi_2(\mathbb{S}^2) = \mathbb{Z}$ low-dimensional analogs in LCs and magnets as 'baby skyrmions' [7, 24, 80].

Although exceptionally useful in classifying topologically distinct field configurations, homotopy theory does not provide the means for exploring the entirety of the topological complexity of fields in soft matter, even in cases when defects and solitons are embedded within a bulk of an ordered medium like LC [82–86]. For example, a closed loop of a half-integer $\pi_1(\mathbb{S}^2/\mathbb{Z}_2) = \mathbb{Z}_2$ disclination is equivalent to a point defect $\pi_2(\mathbb{S}^2/\mathbb{Z}_2) = \mathbb{Z}$ in the far field, but its hedgehog charge depends

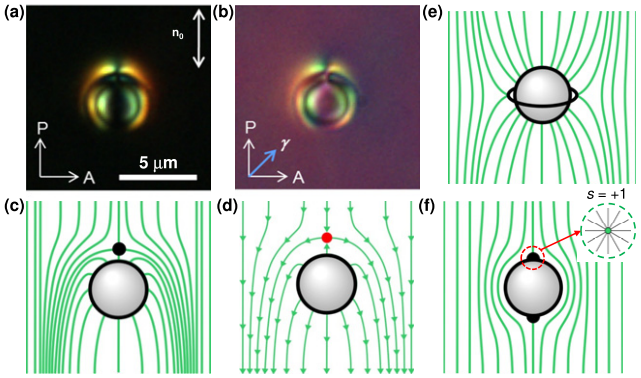

Figure 7. Nematic colloids comprising spherical particles. (a) and (b) Polarizing optical micrographs of an elastic dipole formed by spherical colloidal particles with perpendicular surface anchoring in a planar nematic LC cell. Orientations of the polarizer, analyzer and the slow axis of a full-wave 530 nm retardation plate are labeled 'P', 'A' and 'γ', respectively. (c) and (d) Schematics showing the corresponding (c) nonpolar and (d) vectorized $\mathbf{n}(\mathbf{r})$, with hyperbolic point defects shown by black (c) and red (d) filled circles. (e) and (f) Schematics of the quadrupolar $\mathbf{n}(\mathbf{r})$-configuration around particles with (e) homeotropic and (f) tangential surface boundary conditions. The black ring in (e) represents the 'Saturn ring' half-integer disclination loop. Boojums are marked as black-filled hemi-circles at the particle's poles along the far-field alignment. The inset in (f) shows the radial $\mathbf{n}_s(\mathbf{r})$ director field at the interface of an LC and colloidal sphere corresponding to each of the two boojums.

on how this disclination is closed on itself, its local structure, twisting, knotting and possible linking with other defect loops [82, 84–86]. Knowledge of this relation cannot be predicted solely by the homotopy theory, but can be understood by invoking the analysis of the disclination's structure along the loop, its twist and writhe [84, 85]. In other words, the homotopy theory identifies what the knotted fields can be comprised of, but not how to obtain field configurations with the desired $\pi_2(\mathbb{S}^2/\mathbb{Z}_2)$ hedgehog number by looping and knotting $\pi_1(\mathbb{S}^2/\mathbb{Z}_2)$ vortex lines or how to construct solitons with the desired $\pi_3(\mathbb{S}^2/\mathbb{Z}_2)$ Hopf index by looping and knotting 2D $\pi_2(\mathbb{S}^2/\mathbb{Z}_2)$ skyrmions. Moreover, when LCs and colloidal ferromagnets interact with surfaces due to various boundary conditions, the topology of the structures of these fields interplays with that of surfaces, which can be rather nontrivial and is a subject of ongoing studies. The sections below will overview illustrative examples showing how topology can define the behavior of soft matter systems like nematic colloids, LCs, emulsions, polymer–LC composites, colloidal ferromagnets and so on.

4. Topology of nematic colloids and drops

4.1. Spheres and handlebodies as colloidal particles and confinement surfaces

Colloids are an abundant type of soft matter consisting of tiny (typically nanometers-to-micrometers in dimensions) particles dispersed in chemically distinct host media. The shape of colloidal particles is usually spherical or topologically equivalent to a sphere, though recently colloids with surfaces that have a topology distinct to that of spheres have been developed [34]. When the dispersing medium of the colloidal system is the LC, many interesting forms of interactions between the topologies of surfaces and molecular alignment fields can arise due to the boundary conditions at the LC–particle interfaces. Figure 7 shows polarizing micrographs (figures 7(a) and (b)) of the so-called 'elastic dipole' director structure (figure 7(c)) [53–55, 87] formed by a solid spherical colloidal particle immersed into an aligned nematic LC medium. The particle is accompanied by a point defect, and one can immediately recognize that the topological defect effectively compensates for the radial structure of the director on the particle's surface (figures 7(c) and (d)) [53, 55, 87]. The boundary conditions on the colloidal inclusion's surfaces effectively act as a radial hedgehog point defect, being compensated by a hyperbolic point defect of the opposite hedgehog charge when embedded in the aligned LC (figure 7(d)). Such behavior is natural as the net charge of defects and particles embedded in a uniformly aligned background has to be zero, topologically neutral. Therefore, this structure not only has the dipolar-type elastic far-field perturbation of $\mathbf{n}(\mathbf{r})$ [87], but also features a topological dipole formed by colloidal and singular defect entities of opposite hedgehog charge. However, this simple example can also be further connected to the Poincare and Gauss topological theorems describing interactions of fields and surfaces. Consistent with these theorems, the topological hedgehog charge of the distorted 3D $\mathbf{n}(\mathbf{r})$ at the particle's surface is $\pm\chi/2 = \pm 1$, where $\chi = 2$ is the Euler characteristic of the sphere [30]. Indeed, by choosing to vectorize the director so that vectors point out of the surface of the sphere, one can see that the $m = -1$ topological charge of the particle-induced hedgehog point defect (black and red filled circles shown in figures 7(c) and (d)) compensates for the $+1$ charge of the colloidal particle and obeys the expected relation [55]. Had one chosen to globally vectorize $\mathbf{n}(\mathbf{r})$ so that the vectors point into the particle's surface, the charge of the particle-induced defect would be -1 (sink) and that of the hyperbolic point defect nearby would be $+1$ (source), showing that the hedgehog charges of point defects in nematics are defined up to the sign and that these signs reverse upon changing vectorization directions between the two antiparallel directions along $\mathbf{n}(\mathbf{r})$ [55]. For a nonpolar nematic $\mathbf{n}(\mathbf{r})$ field, inducing a hyperbolic hedgehog point defect is not the only way to embed the particle with perpendicular surface boundary conditions within an aligned LC. The other possible structure, shown in figure 7(e), is what is known as a nematic colloidal quadrupole (note the quadrupolar nature of elastic distortions away from it) with a so-called 'Saturn ring' disclination defect loop [87–91]. This disclination loop is an unknot of a vortex line, the simplest object in the knot tables (figure 3). Since both the hedgehog point defect and the disclination loop can compensate for the same radial structure of $\mathbf{n}(\mathbf{r})$ at the particle's surface, it appears that this particular disclination loop and the point defect must be topologically equivalent and assigned the same hedgehog charge [12, 90]. In the case where a colloidal sphere exhibits tangential boundary conditions, $\mathbf{n}(\mathbf{r})$ features two surface point defects capping the particle at north and south poles (figure 7(f)) [53, 54]. While here one can understand this axisymmetric structure from very

simple considerations of continuity of $\mathbf{n}(\mathbf{r})$ lines tangent to the colloidal sphere's surface, this is also a direct manifestation of the Hairy Ball theorem, which requires that the field lines tangent to $\mathbb{S}^2$ form defects with a net total winding number equal to $\chi = 2$. Indeed, the degrees (winding numbers) of the two $+1$ defects in the $\mathbf{n}_s(\mathbf{r})$ field tangent to the sphere's surface add to $+2$ (figure 7(f)) [54, 55]. Beyond tangential and perpendicular boundary conditions, the understanding of topological defects at the surfaces and in the bulk of LCs induced by spheres was recently extended to tilted and conically degenerate boundary conditions, where boojums and disclination rings tend to appear at the same time [92, 93].

Although the spherical nematic colloids are well studied and understood, topologically nontrivial colloidal particles, such as the ones with shapes of handlebodies, can be fabricated by means of photolithography, two-photon photopolymerization or wet chemical synthesis [34, 55, 69–71]. Such colloidal particles can be characterized by the Euler characteristic $\chi = 2 - 2g$, where g is the particle's genus determined by the number of holes in its surface [30]. Although the role of particle topology in determining the colloidal behavior remains to be understood in fundamental contexts related to Brownian motion, diffusion and self-assembly mediated by electrostatic, depletion and other interactions, most of the work carried out to date was reported for when such particles were introduced into a nematic LC [34, 55, 69–71, 91]. This interest in such nematic colloidal dispersions of topologically complex particles stems from this soft matter system's ability to probe interactions between surfaces and field configurations, where these particles induce topological defects dictated by colloidal topology. Surface functionalization of particles, such as the handlebodies of different genus g made from silica, gold or different polymers [34, 55, 69–71], allows one to define tangential, perpendicular and conically degenerate boundary conditions for the LC molecular alignment and $\mathbf{n}(\mathbf{r})$ [34, 55, 69–71, 92, 93]. The strength of these boundary conditions can be tuned by using different materials and surface functionalization approaches [94–98]. The $\mathbf{n}(\mathbf{r})$ around these handlebody colloids, which approaches the far-field director $\mathbf{n}_0$ at large distances, can be probed by conventional polarizing optical microscopy and different 3D director imaging techniques [99–102], including sub-diffraction-limited mapping of $\mathbf{n}(\mathbf{r})$ [103].

Like for spheres (figure 7), the interplay between the topology of colloidal surfaces and LC alignment field can be probed for ring-shaped and handlebody colloids with different boundary conditions on particle surfaces as well. For tangential surface anchoring, this interplay prompts the appearance of defects dubbed boojums (which we already encountered when discussing colloidal spheres, figure 7(f)), which are ubiquitous and form on the surfaces of ordered media like superfluids, LCs and Bose–Einstein condensates [104–108]. To minimize free energy due to $\mathbf{n}(\mathbf{r})$-distortions (figure 8), the nonspherical particles tend to align with their ring planes parallel to $\mathbf{n}_0$, although metastable configurations with ring planes perpendicular to $\mathbf{n}_0$ are also observed and can be reproducibly obtained by repetitive local melting of the LC by laser tweezers, followed by quenching it back to the nematic state [69]. Handlebody-shaped polymer particles with different genus g distort the nematic molecular alignment while obeying topological constraints to induce at least $2g - 2$ boojums, as revealed by characterizing 3D textures of $\mathbf{n}(\mathbf{r})$ using polarized nonlinear optical imaging (figure 8) [69]. Defects in the 2D $\mathbf{n}_s(\mathbf{r})$ director field at the LC–colloid interface have a net strength adding to χ [30] of the handlebody, although one often also encounters additional surface defects of opposite signs that self-compensate each other, providing additional ways of satisfying topological constraints at multiple stable or metastable particle orientations [69]. For example, a single colloidal torus with a ring plane parallel to $\mathbf{n}_0$ induces four boojums (figures 8(a)–(d)) in the most commonly observed structures [69]. A less frequently observed metastable configuration of a torus particle aligned perpendicular to $\mathbf{n}_0$ contains no boojums, but rather a nonsingular axisymmetric $\mathbf{n}(\mathbf{r})$ that satisfies tangential boundary conditions on the surface of the particle while approaching $\mathbf{n}_0$ at large distances from its surface [69]. The 2D 'surface' nematic director at the surface of a torus with tangentially degenerate boundary conditions contains no defects in the latter case, but four 2D defects (point disclinations) in the former case, two of strength (winding number) $+1$ and two of strength -1 (figures 8(a)–(d)), with winding numbers adding to zero, $\Sigma_i s_i = \chi = 0$, in both cases. In a similar way, handlebody colloids with $g > 1$ aligned with ring planes parallel to $\mathbf{n}_0$ induce several stable and metastable configurations of $\mathbf{n}(\mathbf{r})$ with different numbers and locations of boojums (figures 8(e)–(m)). The number of induced boojums for $g = 2$ is most commonly within 6 to 10, and the net winding number of defects in $\mathbf{n}_s(\mathbf{r})$ tangent to the particle's surface is always $\Sigma_i s_i = -2$ (figures 8(e)–(i)). For colloids of genus 3, 4 and 5 (figures 8(j)–(m)) and all other colloids, the total strength of the point disclinations piercing $\mathbf{n}_s(\mathbf{r})$ at the LC–colloidal interface also adds to the Euler characteristic, $\Sigma_i s_i = \chi$, in agreement with the Poincare–Hopf index theorem [69]. The $s = \pm 1$ point defects locally split into pairs of semi-integer disclinations of equivalent total strength of singularity (figure 8(i)). Rather interestingly, these split-core boojums have handle-shaped bulk disclination semi-loops terminating at the $\pm 1/2$ surface defects within $\mathbf{n}_s(\mathbf{r})$ (figure 8(i)) [69, 109, 110]. Although various stable and metastable states can be expected, colloidal surface topology dictates the presence of at least $2|\chi|$ half-integer defects or at least $|\chi|$ integer-strength boojums (or some combination of them) of a total strength equal to χ for strong and finite boundary conditions on particle surfaces. We note that this does not have to be the case for weak surface anchoring or for particles with dimensions approaching that of the size of singular defect cores (tens of nanometers), where surface boundary conditions can be violated so that the particles produce no or very little perturbations of the director [71].

Experiments reveal that colloidal handlebodies with perpendicular boundary conditions also tend to spontaneously align with ring planes either perpendicular or parallel to $\mathbf{n}_0$, which again is driven by minimizing the elastic energy costs of the particle-induced $\mathbf{n}(\mathbf{r})$ (figure 9) [34]. Handlebody colloidal particles with planes of rings parallel to $\mathbf{n}_0$ induce point defects, both inside and outside of the rings (figures 9(a)–(f)),

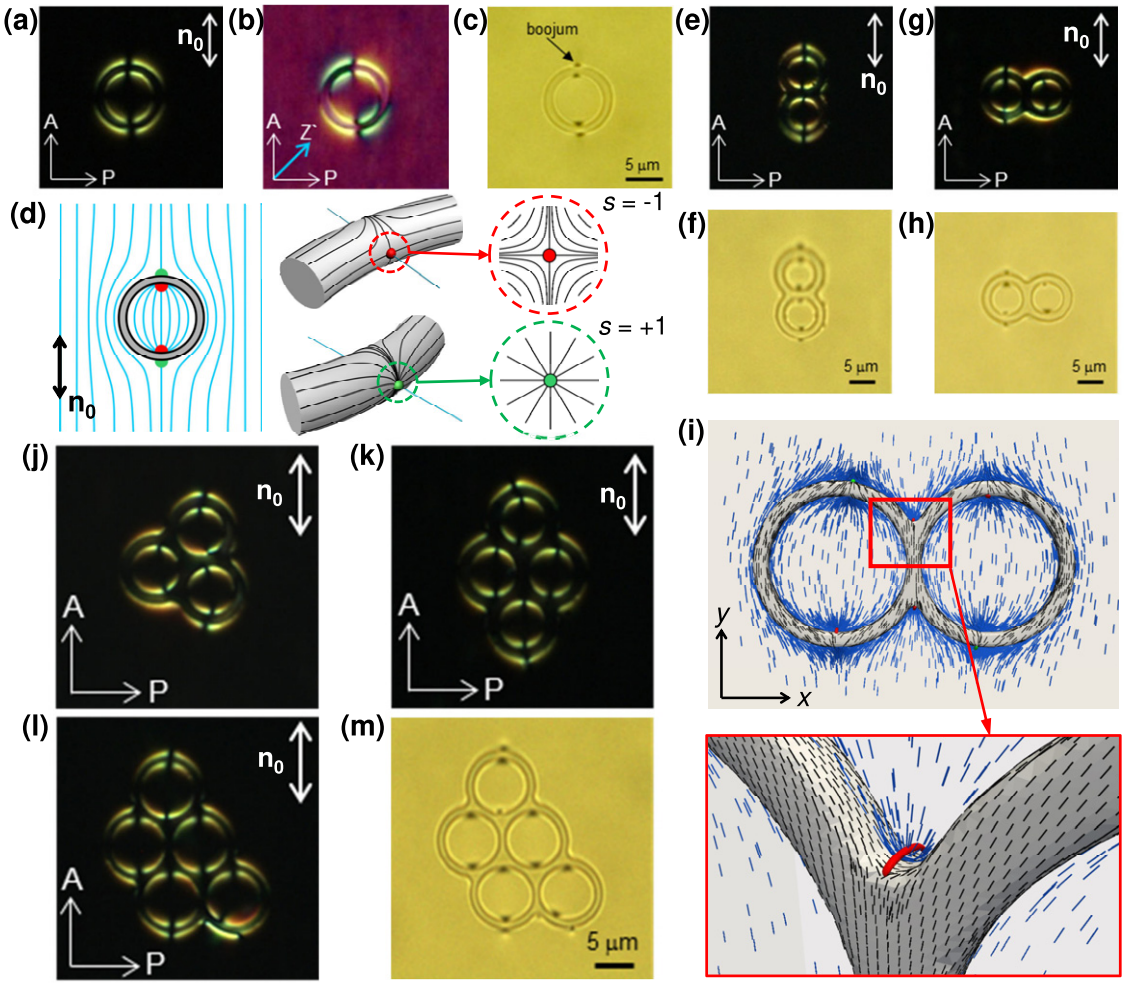

Figure 8. Colloidal tori and handlebodies with tangential boundary conditions. (a)–(d) A torus-shaped particle with tangential anchoring and the ring plane parallel to $\mathbf{n}_0$. Polarizing optical micrographs taken without (a) and with (b) a 530 nm retardation plate with a slow axis Z'. Orientations of the polarizer and analyzer are labeled 'P' and 'A', respectively. (c) A bright-field micrograph of a torus with four boojums visible as dark spots. (d) A schematic of $\mathbf{n}(\mathbf{r})$ in a plane containing the ring and $\mathbf{n}_0$. Insets schematically depict 2D defects in the director $\mathbf{n}_s(\mathbf{r})$ tangent to the particle's surface. Green and red semi-spheres and circles represent, respectively, $s = 1$ and $s = -1$ surface defects in $\mathbf{n}_s(\mathbf{r})$. (e)–(h) Colloidal handlebodies with $g = 2$. Polarizing optical micrographs (e) and (g) and corresponding bright-field (f) and (h) images of the handlebodies with ring planes parallel to $\mathbf{n}_0$ but with the axis connecting the centers of two rings at different orientations with respect to $\mathbf{n}_0$. (i) Numerically calculated $\mathbf{n}(\mathbf{r})$ in the LC bulk (blue rods) and $\mathbf{n}_s(\mathbf{r})$ on the surface (black rods) of the $g = 2$ colloidal handlebody; the inset shows a detailed view of $\mathbf{n}(\mathbf{r})$ and $\mathbf{n}_s(\mathbf{r})$ in the near-boojum regions marked in (i), with the isosurfaces of the constant reduced scalar-order parameter $Q = 0.25$ shown in red and visualizing a handle-shaped core structure of the boojum. (j)–(m) Colloidal handlebodies with genus of (j) 3, (k) 4 and (l) and (m) 5. Reproduced with permission from [69].

which manifest themselves as points of termination of dark and bright brushes in the polarizing optical micrographs (figures 9(g)–(i)). Handlebody colloids aligned perpendicular to $\mathbf{n}_0$ are all surrounded by single half-integer exterior disclination loops of hedgehog charge equal to unity (figures 9(j)–(n)). Additionally, each such genus-g particle has g defects in its holes, which are either singular disclination loops or hyperbolic point defects of elementary (unity) topological hedgehog charge (figures 9(j)–(n)). Disclination loops in the holes of each handlebody can be transformed into point defects and vice versa by melting the LC into an isotropic state using high-power focused laser light, showing that they correspond to stable or metastable structures (separated by energetic barriers) under the different conditions [34, 55]. Hedgehog charges of these defects have been determined for vector field lines pointing perpendicularly outward from the particle surfaces and mapping onto the $\mathbb{S}^2$ order parameter space for globally vectorized $\mathbf{n}(\mathbf{r})$. Like for spheres (figures 7(c) and (d)), since $\mathbf{n}(\mathbf{r})$ is nonpolar ($\mathbf{n} \equiv -\mathbf{n}$), one could have chosen the opposite direction of vectorizing, which would consequently reverse the signs of all hedgehog charges due to defects and surfaces of particles, all embedded within an aligned LC. Although the handlebodies orientated perpendicular and parallel to $\mathbf{n}_0$ induce very different $\mathbf{n}(\mathbf{r})$, the sum of hedgehog charges is always pre-determined by $\pm\chi/2 = \pm(1 - g)$. This finding is consistent with predictions of topological theorems [30] that define the charge of the $\mathbf{n}(\mathbf{r})$ on the surface of the handlebody of a given χ. The topological hedgehog due to $\mathbf{n}(\mathbf{r})$ on the particle's surface is compensated by the net charge of particle-induced defects $\sum_i m_i = \pm\chi/2$ (of opposite sign) in the LC bulk, as is needed to embed such a colloidal object into the uniformly aligned LC [34, 55]. This relation was found to hold

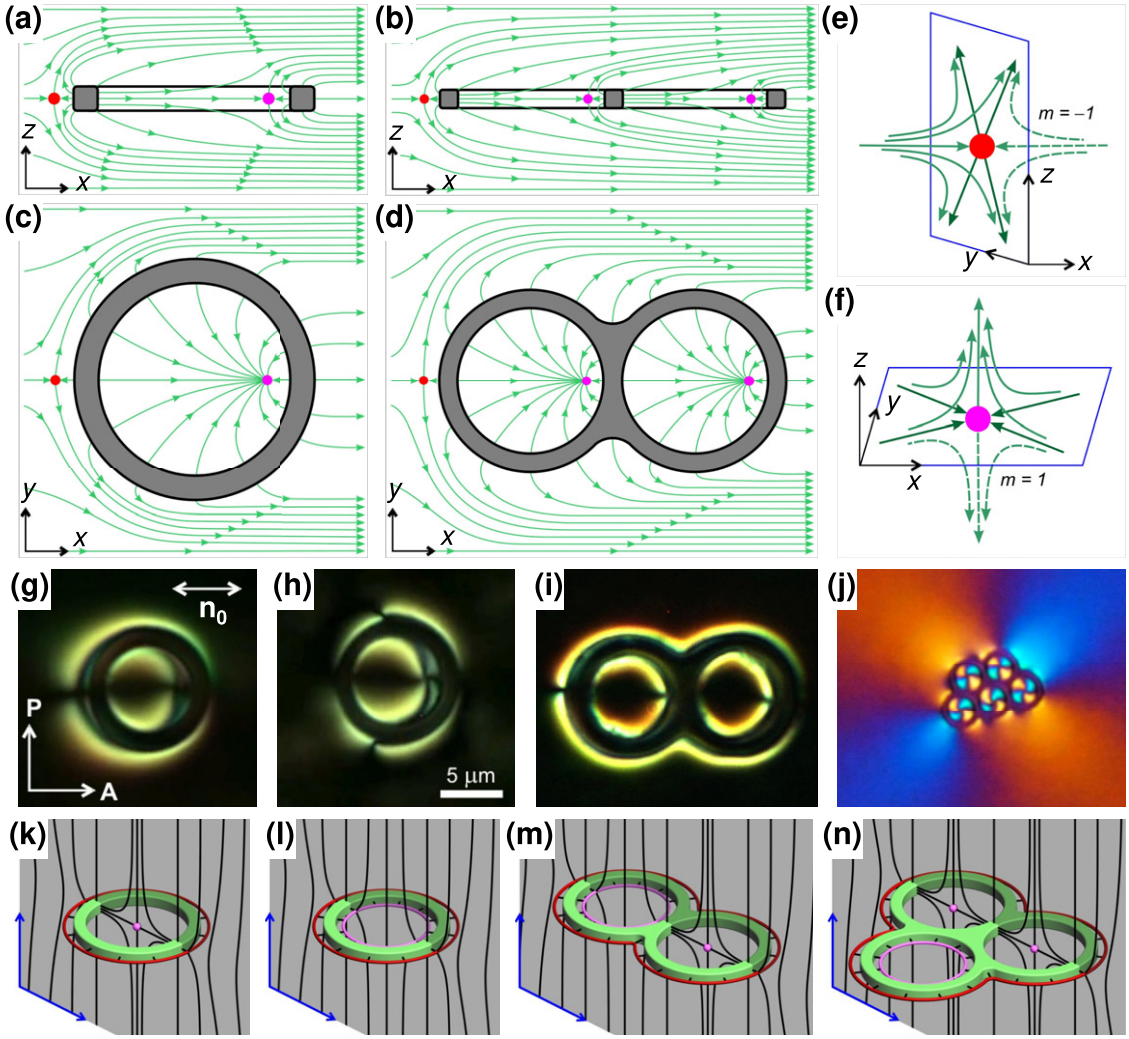

Figure 9. Colloidal handlebodies with perpendicular surface boundary conditions. (a)–(d) Schematics showing the vectorized-field representations of $\mathbf{n}(\mathbf{r})$ (green lines with arrows) around single ((a) and (c)) and double ((b) and (d)) colloidal handlebodies in the plane of the rings ((c) and (d)) and in planes orthogonal to them ((a) and (b)). (e) and (f) Diagrams of vectorized $\mathbf{n}(\mathbf{r})$ around hyperbolic topological point defects of negative (e) and positive (f) signs shown by red- and magenta-filled spheres, respectively. (g)–(j) Polarizing optical micrographs of $\mathbf{n}(\mathbf{r})$ for samples with different colloidal handlebodies. Orientations of the polarizer and analyzer are the same for all micrographs (g)–(j) and are labeled 'P' and 'A' in (g). Colors in (j) emerge from polarized interference of imaging light passing through the LC. (k)–(n) Schematics of $\mathbf{n}(\mathbf{r})$ (black lines) around colloidal handlebodies of different genus. Red and magenta lines show outer and inner disclination loops of hedgehog charges $m = -1$ and $m = +1$, respectively. Magenta spheres show the $m = +1$ hyperbolic point defects. Reproduced with permission from [34].

for handlebodies with $g = 1, 2, \ldots, 5$ (figure 9) and for spherical colloids with $g = 0$ (figure 7). Although perpendicular boundary conditions due to the handlebody-shaped particles in the LC with a uniform $\mathbf{n}_0$ can be satisfied by a minimum number of point or ring defects of the same sign with the total hedgehog charge of $\sum_i m_i = \pm\chi/2$, these field configurations are often energetically costly and tend to relax to topology-satisfying field configurations that minimize the elastic free energy but have additional self-compensating pairs of defects of opposite hedgehog charge. In the experimental systems, colloidal g-handlebodies typically induce $g + 1$ individual defects, from which two self-compensating defects have opposite signs and appear just to minimize free energy [55, 111]. These additional self-compensating defects are caused by energy minimization rather than topological requirements. The fact that these extra defects help by minimizing energy may sound strange because they are typically associated with high energy costs; it often turns out to be energetically beneficial to have such extra defects rather than much more severe bend-splay-twist deformations of the director that would be required to keep the overall number of defects at the topologically required minimum.

Examples in figures 7–9 show that, by building on the interplay of surface and field topologies with roots in Gauss, Hairy Ball and Poincare theorems, one can (on-demand) generate LC surface defects of total net winding number adding to $\pm\chi$ and bulk defects with hedgehog charges adding to $\pm\chi/2$ by using colloidal particles with various Euler characteristics. It is also interesting that colloidal unknots and handlebodies induce unknots or point defects in the forms of closed-loop disclination defects in their interior and exterior [34, 55], as well as that the energetically driven number of unknots or singular points

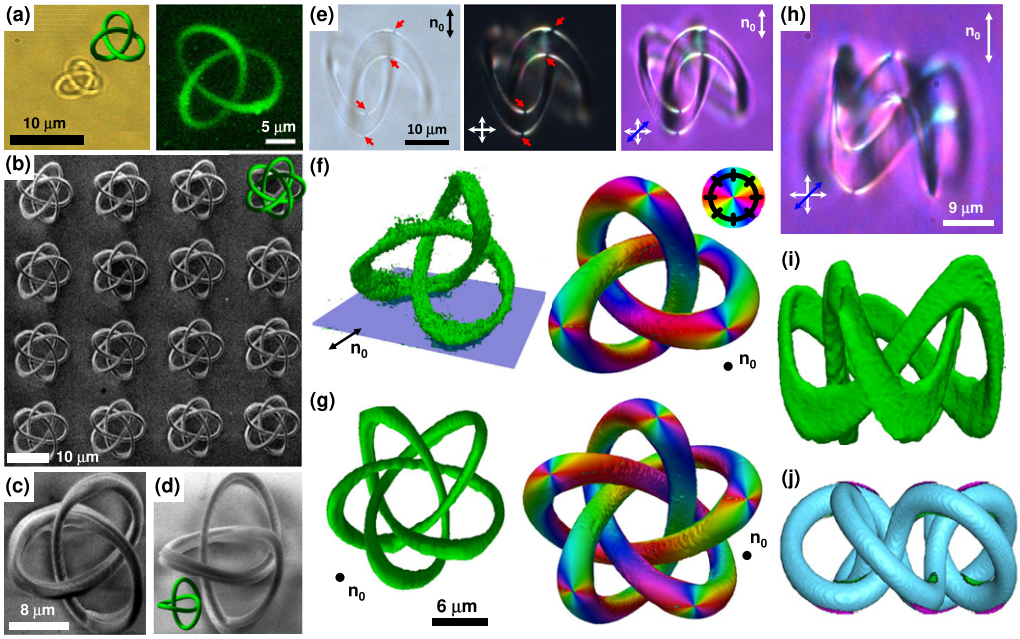

Figure 10. Nematic colloidal knots with tangential boundary conditions. (a) Trefoil colloidal knots shown in (left) an optical micrograph of a photopolymerized colloidal trefoil torus knot, with the corresponding 3D model shown in the inset, and (right) a nonlinear luminescence image of a particle fabricated by means of the spatially-resolved graphene oxide reduction with femtosecond laser light (left-side image reproduced with permission from [35]; right-side image reproduced with permission from [125]). (b)–(d) Scanning electron micrographs of a (b) 4×4 array of $T(5,3)$ torus knots and (c) and (d) a single $T(3,2)$ knot shown as viewed along the torus axis (c) and in an oblique direction (d). (e) Bright-field and polarizing optical micrographs taken without polarizers (left), between crossed polarizers (middle), and with an additional 530 nm retardation plate with its slow axis aligned as shown by the blue double arrow (right). Orientations of crossed polarizers are shown by white double arrows. Locations of boojums are marked by red arrows. (f) A 3D nonlinear fluorescence pattern (left) and representation of $\mathbf{n}(\mathbf{r})$ deviating away from $\mathbf{n}_0$ due to the incorporated trefoil knot particle (right). Colors depict the azimuthal orientation of $\mathbf{n}(\mathbf{r})$ when projected onto a plane orthogonal to $\mathbf{n}_0$ according to the scheme shown in the inset. The structure is visualized on a tube following the knotted particle's surface; points where colors meet are the boojum defects. (g) The same as in (f) but for the $T(5,3)$ particle. (h) An optical micrograph of the $T(5,2)$ knot particle obtained for crossed polarizers (white double arrows) and a phase retardation plate (blue double arrow) aligned with its slow axis at 45° to polarizers and $\mathbf{n}_0$. (i) The reconstructed 3D fluorescence pattern due to the $T(5,2)$ colloidal knot particle and $\mathbf{n}(\mathbf{r})$ induced by the particle as viewed perpendicular to the torus axis. (j) The corresponding numerical model showing boojums induced by the $T(5,2)$ particle. Green and magenta areas show the spatial regions of a reduced scalar-order parameter, corresponding to the $s = -1$ and $s = 1$ defects in the 2D $\mathbf{n}(\mathbf{r})$ at the LC–particle interface, respectively. Reproduced with permission from [35].

that a particle with perpendicular boundary conditions generates in a nematic LC increases with g. Even though some of these unknots are topologically self-compensating and some are being substituted by point defects to minimize energy [34], this interplay between the topology of colloids and defects poses a question whether various knotted vortices can be induced by colloidal particles with knot-like shapes, which is addressed in the next section.

4.2. Knots as colloidal particles

By taking advantage of two-photon photopolymerization [112] and other fabrication techniques [55], it is also possible to fabricate knot-shaped microparticles (figures 10(a)–(d)) and explore the interplay of topologies of the knotted surfaces and molecular alignment fields [35]. This knowledge may be used for understanding other experimentally less accessible physical systems with similar topological objects. On the other hand, such knotted colloids can be interesting building blocks of topological matter arising from the mesoscale self-organization of knotted colloidal 'atoms' driven by minimization of elastic energy and mutual entanglement of induced defects [35]. When dispersed in LCs, knotted colloids with controlled surface boundary conditions distort $\mathbf{n}(\mathbf{r})$, so that the minimization of free energy associated with these elastic distortions again plays a key role in the physical behavior. For example, to minimize elastic free energy, trefoil particle knots tend to align with their torus planes perpendicular to the undistorted far field $\mathbf{n}_0$. Particle-induced boojums at their surfaces are visible in bright-field micrographs as dark points due to scattering (figure 10(e)). A color-coded 3D representation of the azimuthal orientation of $\mathbf{n}(\mathbf{r})$ reveals 12 boojums around the particle (figure 10(f)), forming nearby regions with the largest local curvature of the trefoil knot's surface [35] and where the particle's surface is locally orthogonal to $\mathbf{n}_0$. These boojums can be characterized by a net winding number s of the defects in a 2D field $\mathbf{n}_s(\mathbf{r})$ at the LC–particle interface, just as in the case of colloidal handlebodies that were discussed above, obtaining $\Sigma_i s_i = \chi = 0$, where $\chi = 0$ for the knot particle's surface [30]. Although this topological constraint could be satisfied in many different ways that yield $\Sigma_i s_i = 0$, the one observed experimentally corresponds to a minimum of the total free energy, containing 12 surface point defects, out of which six $s = 1$ boojums localize on exterior tips of the knot and their six $s = -1$

counterparts reside on the diametrically opposite sides of the knotted tube along $\mathbf{n}_0$ [35]. Such characterization of particle-induced defects can be extended to other torus knots, as shown for another example in figures 10(g)–(j). Generally, colloidal torus knots with tangential anchoring induce boojums which obey the same topological constraint $\Sigma_i s_i = 0$ as their trefoil counterparts (figures 10(g)–(j)), since they all have $\chi = 0$. Typically the number of self-compensating surface defects in stable colloidal structures induced by torus-knot particles with tangential anchoring is four times the number of knot string's turns around the circular axis of the corresponding torus, though one occasionally also observes metastable states with different net numbers and locations of boojums with the winding number adding to $\chi = 0$ [35, 55].

Trefoil particle knots with perpendicular surface boundary conditions tend to align with a torus plane orthogonal to $\mathbf{n}_0$ in the ground state (figure 11), but can also exhibit metastable orientations, including those parallel to $\mathbf{n}_0$. Polarizing optical micrographs (figures 11(a) and (b)) and depth-resolved nonlinear optical 'slices' obtained for different polarizations of femtosecond excitation laser light (figures 11(d) and (e)) show the presence of defect lines and match the theoretical configuration (figures 11(c) and (f)) [35, 55]. These defect lines compensate for the director distortion imposed by the particle's surface (figures 11(c) and (f)). Two linear defects tracing the knotted particle's tube are also the basic feature of metastable states, although these states are often accompanied by disclination rewirings (figures 11(g)–(j)). This shows that knotted particles can generate defect loops in nematic fields in such a way that these singular loops are knotted too. For a trefoil knot particle shown in figures 11(a)–(f), the two defect loops are both trefoil knots linked with each other and with the particle knot (inset of figure 11(f)), effectively forming a three-component defect-particle composite link. Although the torus-knot particles with perpendicular boundary conditions are typically accompanied by two knotted half-integer defect lines, the topological constraints allow for flexibility in terms of precise ways of satisfying them because the knotted and interlinked loops can have different effective hedgehog charges that just need to add to zero because of the colloidal torus knot's surface with $\chi = 0$. These configurations can be selected by varying confinement, quenching of temperature and applying external fields, thus creating an experimental arena for controlling this behavior. Knotted defects can mediate colloidal self-assembly by means of both anisotropic elastic forces and entanglement. Therefore, by establishing general principles for the 3D control of defects, the demonstrated interplay of the topologies of knotted colloidal surfaces and nematic fields provides a basis for highly unusual forms of self-assembly [55].

Knotted structures of disclinations could also be induced by particles differing from knots, such as colloidal spheres [33, 113–115] with the perpendicular surface anchoring in twisted LC cells and by nonorientable colloidal surfaces [36]. It is very interesting that free-energy minimization and topological constraints in these cases can yield knotted vortices as stable or metastable structures in the presence of confinement, though

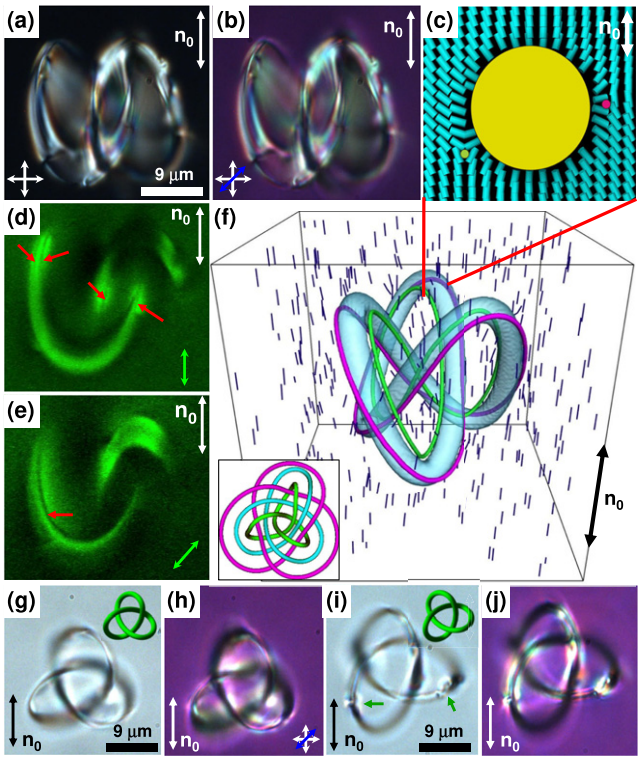

Figure 11. Colloidal knots with perpendicular boundary conditions. (a) and (b) Optical micrographs of a trefoil knot in an aligned nematic (a) taken between crossed polarizers (white double arrows) and (b) with a 530 nm retardation plate (blue double arrow) inserted with its slow axis at 45° to the polarizers. (c) Computer-simulated $\mathbf{n}(\mathbf{r})$ within a cross-section perpendicular to the knotted tube marked in (f). (d) and (e) Nonlinear polarized fluorescence images of $\mathbf{n}(\mathbf{r})$ around the knotted particle shown in (a) and (b), and for the femtosecond excitation-light polarizations (green double arrows) at different orientations with respect to $\mathbf{n}_0$. Red arrows mark the defect lines visible in the image plane. (f) Computer-simulated $\mathbf{n}(\mathbf{r})$ around a trefoil knot with perpendicular boundary conditions and the torus plane self-aligned orthogonally to $\mathbf{n}_0$. Green and magenta tubes show the regions with a reduced scalar-order parameter corresponding to the cores of the two knotted singular defect lines seen in the cross-sections (d) and (e). The bottom-left inset shows a topological schematic of the mutual linking between the particle knot (blue) and defect knots (green and magenta). (g)–(j) Bright-field micrographs of colloidal knots aligned with the torus plane parallel to $\mathbf{n}_0$, and taken without polarizers (g) and (i) and between crossed polarizers with an inserted full-wave retardation plate (h) and (j). Green arrows in (i) indicate regions of the defect line rewirings. Reproduced with permission from [35].

we will see later in the review that knotted vortices and solitons can arise in LCs as stable field configurations, even without colloids or confinement [73]. On the other hand, colloidal knots in isotropic solvents have been considered theoretically, as well as the potential to employ LC elastomeric knotted particles as topology-changing colloidal objects has been numerically explored [113, 114]. However, much more can be done as topology has potential impacts on all aspects of colloidal science, from self-assembly of crystals and quasi-crystals to out-of-equilibrium dynamics [116–120]. For example, one could combine topology and active matter paradigms in an effort to achieve topology-dictated nonequilibrium self-assembly of topologically distinct active particles [121–123]. Active

colloids are a distinct category of nonequilibrium matter in which energy uptake, dissipation and movement take place at the level of discrete microscopic constituents [121]. They are known to provide types of self-assembly not accessible in traditional equilibrium condensed matter systems [121]. However, only topologically trivial types of active colloids (spherical or topologically isomorphic to spheres) have been studied so far. The interplay of topologies of surfaces and flow fields due to the self-propulsion of active particles could result in highly unusual yet controlled and practically useful forms of self-assembly.

Large quantities of colloidal knots can be obtained by combining two-photon photopolymerization and structured shaping of femtosecond laser light with spatial light modulators [124]. In addition to polymer-based dielectric knot-shaped particles, researchers have fabricated colloidal objects through 3D-spatially-resolved laser reduction of graphene oxide nanoflakes [125]. Utilizing the particle's luminescence, the shapes of such knots could be reconstructed from 3D photoluminescence data (right-side of figure 10(a)) [125]. Because the internal orientation of reduced graphene oxide flakes within the colloidal structures matches that of the surrounding graphene oxide flakes, the fabricated knotted particles differ from the polymerized ones [35, 55] in that they do not induce noticeable director distortions or topological defects in the surrounding LC host [125]. This demonstrates that topological defects can be avoided when the boundary conditions for the director orientation on the surfaces of complex-shaped particles are weak or match the director of the surrounding LC, even when the colloidal inclusions exhibit nontrivial topology of knots. Super-paramagnetic knot-shaped colloidal particles have also been reported and used to induce stick-slip motion of surface defects [126]. These examples show that knot-shaped colloidal particles of different types are becoming accessible to the research community and offer great potential for advancing new soft matter science.

4.3. Linked composite colloids

Recent advances in particle fabrication have also enabled colloids with the topology of multicomponent links classified in figure 4, such as the two-component Hopf and Solomon links (figure 12) [55, 72]. What are the implications of topological linking on the behavior of the nematic colloidal systems? Micrometer-sized colloidal particles with differently linked components shaped as solid, rigid polymeric rings undergo Brownian motion both relative to each other and as a whole when dispersed in LCs [72]. These particles induce different director field configurations that define elastic coupling between the components, where certain relative orientations and positions of rings correspond to local or global free-energy minima determined by LC's orientational elasticity of corresponding $\mathbf{n}(\mathbf{r})$ structures (figure 12) [72]. As an example, colloidal Hopf links consist of two rings and are characterized by a linking number topological invariant $Lk = \pm 1$, representing the number of times that each closed colloidal loop winds around the other loop (figures 12(a)–(e)). In the colloidal Solomon's link of $Lk = \pm 2$ the two closed rings are doubly interlinked, so that this particle exhibits four

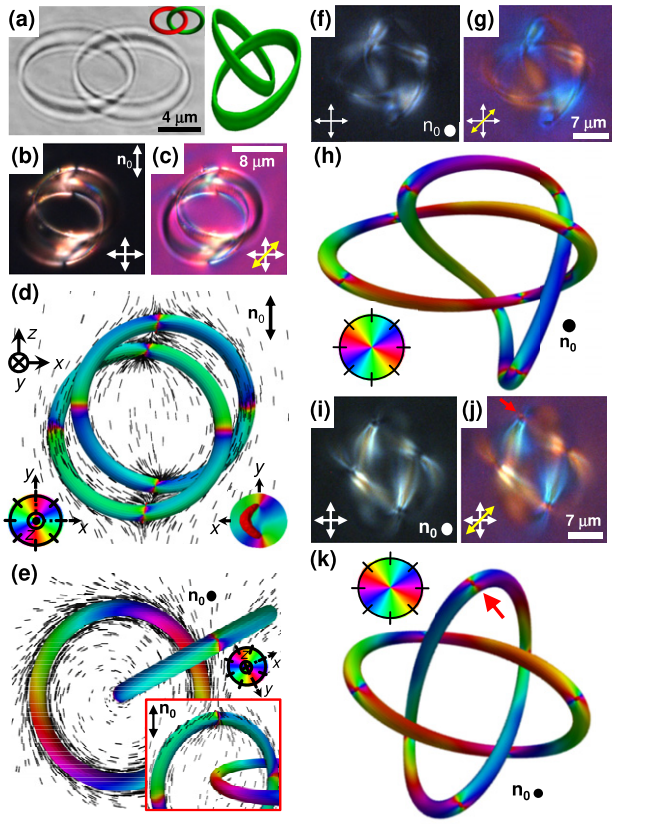

Figure 12. Nematic colloidal two-component links with tangential boundary conditions. (a) An optical bright-field micrograph (left) of a Hopf-link particle with its 3D model shown in the inset and a 3D nonlinear fluorescence image of the same particle (right). Red and green colors are used in the inset to distinguish the two different linked rings. (b) and (c) Optical micrographs of a colloidal Hopf link in a nematic, as viewed between crossed polarizers without (a) and with (b) an additional 530 nm wave plate (with its slow axis marked by the yellow double arrow). (d) Numerically simulated $\mathbf{n}(\mathbf{r})$ depicted using colors on the particle's surfaces and using rods in the LC bulk. Colors show azimuthal orientations of $\mathbf{n}(\mathbf{r})$ with respect to $\mathbf{n}_0$ according to the scheme shown in the lower-left inset; the lower-right inset shows details of the core structure of a boojum splitting into a semi-loop of a half-integer defect line with the handle-shaped region of the reduced scalar-order parameter shown in red. (e) Numerical $\mathbf{n}(\mathbf{r})$ depicted as in (d) but in a metastable state when the plane of one of the link's rings is normal to $\mathbf{n}_0$; the inset shows a different perspective view of the same link. (f) and (g) A colloidal Solomon link in a homeotropic nematic cell as viewed (f) between crossed polarizers and (g) between crossed polarizers and a waveplate (the yellow double arrow depicts orientation of the slow axis). (h) A numerical model of $\mathbf{n}(\mathbf{r})$ depicted using colors on the particle surfaces corresponding to the experimental images shown in (f) and (g). (i) and (j) Another configuration observed for a similar Solomon link viewed between (i) crossed polarizers without and (j) with an inserted wave plate. (k) The corresponding numerical $\mathbf{n}(\mathbf{r})$ depicted using colors on the particle surfaces. Crossed polarizers and the far-field director are marked by white double arrows, as labeled on the images. Reproduced with permission from [72].

crossings of the two loops interweaving under and over each other (figures 12(f)–(k)). Out of several stable and metastable $\mathbf{n}(\mathbf{r})$ configurations induced by the Hopf-link colloids with tangential anchoring, the most common one contains eight surface boojums (figures 12(b)–(d)), four on each of the linked colloidal rings tilted away from $\mathbf{n}_0$. Elastic director distortions

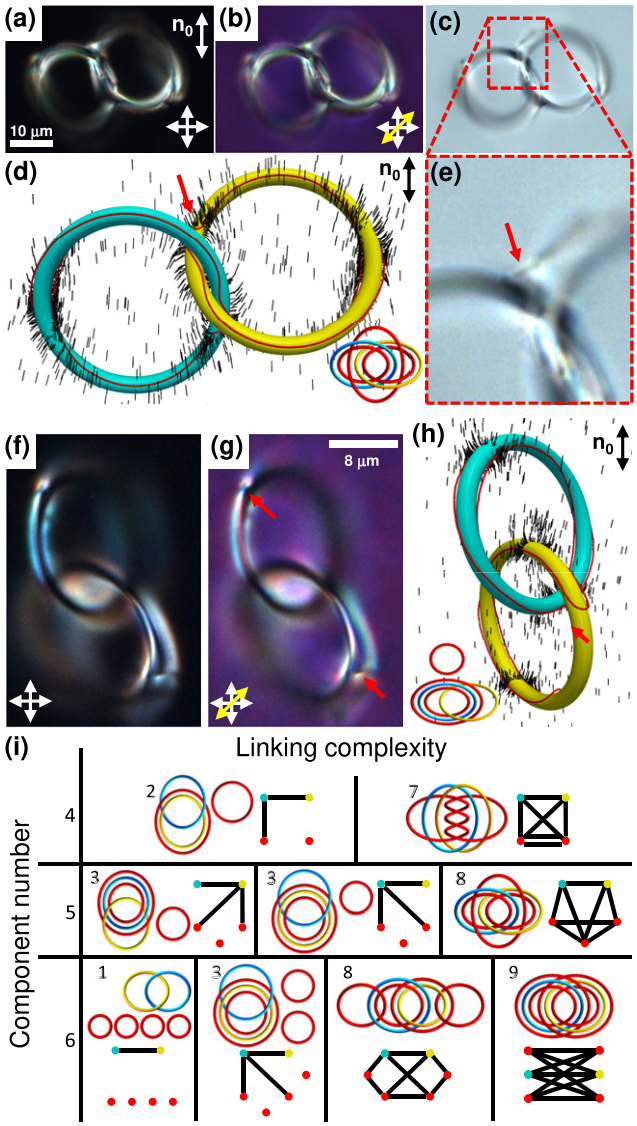

Figure 13. Nematic colloidal two-component links with perpendicular boundary conditions. (a)–(e) A colloidal Hopf link studied using optical micrographs taken (a) and (b) between crossed polarizers shown by white double arrows (a) without and (b) with an additional full-wave 530 nm retardation plate (the yellow double arrow shows its slow axis), and (c) in a bright-field mode. (d) A corresponding numerical model, with $\mathbf{n}(\mathbf{r})$ shown by rods and defect lines as the red tubes of the reduced scalar-order parameter. The inset shows a schematic of linked colloidal and defect loops. (e) A zoom-in view of (c) focusing on the jumping disclination seen in both experiments and theory, marked by red arrows in (d) and (e). (f)–(h) Another configuration of a similar Hopf link. (f) and (g) Optical micrographs of this particle taken under conditions as in (a) and (b). (h) A corresponding theoretical model; the inset shows a simplified topological skeleton. (i) Topological skeletons and graphical representations of Hopf-link particles and accompanying closed defect loops. The mutually linked physical-particle rings are shown in blue and yellow colors, and the defect line loops are shown in red. In the graphs, the individual links are indicated by black edges connecting the corresponding red–blue–yellow filled circles that represent colloidal or defect rings; the overall number of links is indicated next to the topological skeletons. Reproduced with permission from [72].

weakly couple the two linked components, defining the equilibrium center-to-center distance and locations at which these rings cross the planes of each other (figure 12(d)), as well as the equilibrium angle between the center-to-center separation vector connecting the linked components and $\mathbf{n}_0$. Anisotropic elastic forces also keep the linked particles apart, acting against touching of the linked component rings. Metastable colloidal and field configurations with other orientations of rings and different numbers of boojums are also observed [72]. For example, one of them (figure 12(e)) contains a boojum-free ring perpendicular to $\mathbf{n}_0$, linked to a ring with four boojums [72], both with well-defined orientations relative to $\mathbf{n}_0$. Boojums always appear in self-compensating pairs of opposite winding numbers in 2D $\mathbf{n}(\mathbf{r})$ at the LC–particle interfaces, consistent with the zero Euler characteristic of the rings of multicomponent particles. Colloidal Solomon links with tangential boundary conditions tend to induce twice as many boojums than their Hopf counterparts (figures 12(f)–(k)), with these surface point defects located at the tip points of the tubes along $\mathbf{n}_0$. A large number of stable and metastable mutual positions and orientations of the linked components, as well as their orientation with respect to $\mathbf{n}_0$, lead to diverse $\mathbf{n}(\mathbf{r})$ configurations differing by the number of the generated boojum–antiboojum pairs with opposite 2D winding numbers (figures 12(f)–(k)). These illustrative examples reveal that linked ring colloids inherit the diversity of structures that we have seen above for single rings (e.g. individually each ring component of the link can have no associated boojums or even numbers of self-compensating boojums), but now with the diversity of accessible metastable and stable structures boosted dramatically by different linking invariants, different relative orientations and positions of the rings, as well as their relative orientations with respect to $\mathbf{n}_0$.

Even more exotic behavior of linked colloids is observed when their surfaces impose perpendicular boundary conditions for $\mathbf{n}(\mathbf{r})$ (figure 13). These particles tend to induce closed loops (unknots) of singular defect lines [72]. In addition to the purely elastic coupling, colloidal components often get entangled by unknots of defect lines that act as elastic strings (figures 13(a)–(e)). Surfaces of colloidal links have $\chi = 0$, so that the hedgehog charge of $\mathbf{n}(\mathbf{r})$ on their surfaces is equal $\chi/2 = 0$, requiring no bulk defects to embed in the aligned LC and also imposing constraints on the overall zero bulk hedgehog charges of defects around such particles [30, 55]. However, free-energy minimization and the nonpolar nature of $\mathbf{n}(\mathbf{r})$, combined with the rich configuration space of the colloidal object itself, accommodate the boundary conditions on particle surfaces by forming a variety of topologically distinct configurations of closed defect loops (figure 13) [72]. Individually linked components of the defect-colloidal entity freely move with respect to each other due to thermal fluctuations. With field configurations governed by the elasticity of the nematic fluid, they exhibit relative separations and orientations corresponding to the free-energy minima (figures 13(a)–(h)) [72]. The simplest observed configuration involving a Solomon link

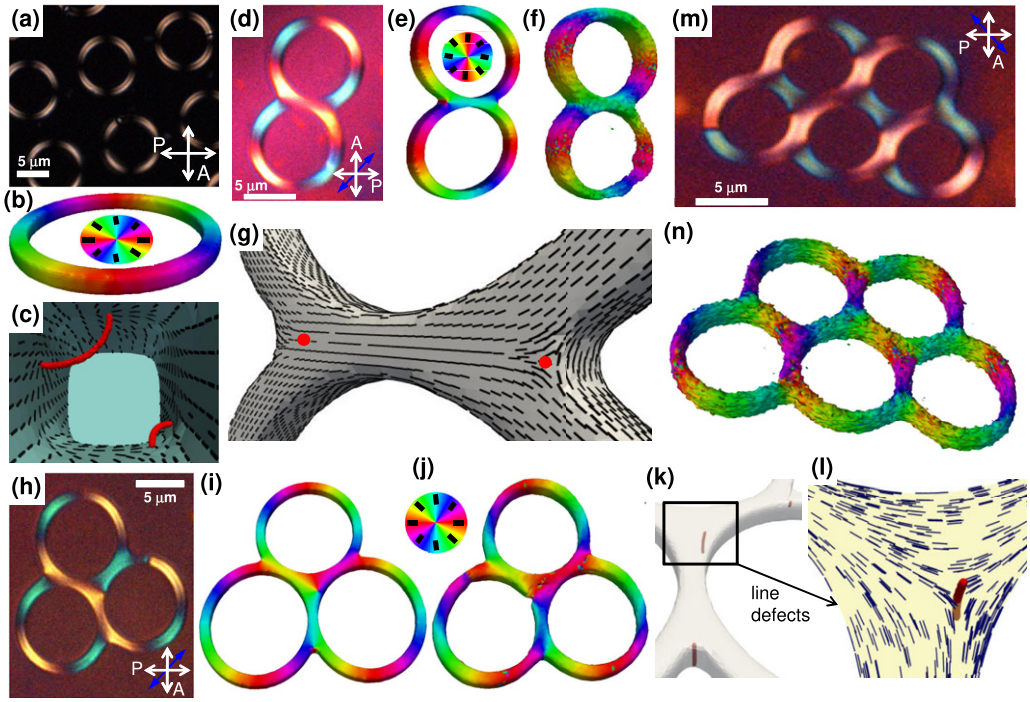

Figure 14. Topologically nontrivial polymer-dispersed LC drops with tangential anchoring. (a)–(c) A polymer matrix with $g = 1$ nematic drops (a) as observed in an optical polarizing micrograph and (b) depicted based on 3D numerical $\mathbf{n}(\mathbf{r})$ modeling (with the color-coded scheme of azimuthal orientations shown in the inset) and (c) with zoomed-in $\mathbf{n}(\mathbf{r})$ in the vicinity of self-compensating defects found in metastable states of some drops, as shown in the drop's interior. Disclinations are shown as red tubes and filled circles representing regions of the reduced scalar order parameter. (d)–(g) Nematic $g = 2$ drops (d) seen in a polarizing micrograph obtained with an additional 530 nm phase retardation plate, (e) and (f) in 3D representation of $\mathbf{n}(\mathbf{r})$ at the surface of a $g = 2$ drop based on (e) numerical modeling and (f) experiments. The color-coded scheme of azimuthal orientations is shown in the inset of (e). (g) Nematic configurations and defects at the junction of two tori, with $\mathbf{n}(\mathbf{r})$ at the LC–polymer interface depicted using rods and the line defect cores in the bulk of the $g = 2$ drop shown using (red) regions of the reduced scalar-order parameter. (h)–(l) Nematic $g = 3$ drops (h) as seen in an optical micrograph obtained between crossed polarizers and with an additional retardation plate and in ((i) and (j)) 3D representations of $\mathbf{n}(\mathbf{r})$ at the LC–polymer interface obtained (i) by numerical modeling and (j) experimentally; the color-coded scheme of azimuthal orientations is shown in the inset. (k) and (l) Defect lines at tori junctions seen as red tubes of reduced order parameter (k) and $\mathbf{n}(\mathbf{r})$ shown for one of them (l). (m) and (n) A polarizing optical micrograph of $g = 5$ drop obtained between crossed polarizers with an additional phase retardation plate (m) and corresponding 3D representation of $\mathbf{n}(\mathbf{r})$ at the drop's surface (n). For polarizing micrographs, white double arrows depict orientations of crossed polarizers and the blue double arrows show the orientation of a slow axis of the 530 nm retardation plate. Reproduced with permission from [142].

with perpendicular surface boundary conditions contains pairs of individual looped defect lines following each of the linked components. Interestingly, particles of the same linking number and perpendicular boundary conditions can induce configurations of defect loops which cannot be continuously transformed one to another. For example, the Hopf-link colloids were found exhibiting two to four unknots of half-integer defect lines, which can be linked with a single or both colloidal rings or with each other, which are summarized along with the corresponding graphs in figure 13(i). The graphs show that the number of the linking-connected inseparable graph entities can range from one, when all particle and defect rings are interlinked, to five, when Hopf-link particles are accompanied by four unlinked defect loops (figure 13(i)). These mixed defect-colloidal multicomponent links cannot be smoothly morphed one to another, having different total numbers of unknots (colloidal rings or defect loops) and numbers of links between them visible in simplified topological skeletons and graph representations (figure 13(i)). The configurations in figure 13(i) do not exhaust all the topology-admissible structural varieties of field configurations. Moreover, it is rather interesting that a single Hopf link of colloidal particles can be accompanied by different configurations of up to four defect loops with different links between them. This experimentally revealed topological diversity calls for one to apply techniques like those used in [82, 85] to reveal further details of this fascinating behavior. Due to inseparability of the linked particle components, pair and many-body interactions can exist among the linked components belonging to the same composite particle, constrained by the physical linking, or to different multicomponent particles. Sharing or linking of defect loops induced by the linked rings provides an additional colloidal interaction mechanism due to the line tension, which is of the order of 50–70 pN for singular half-integer defect lines [127], and which can alter the response of such particles to external stimuli like light [128, 129].

The nematic colloidal links and knots above exemplify the unexpected emergent topological complexity of defect structures that appear even when they are not required by the known topological theorems for particle surfaces with zero Euler characteristics. However, in addition to linked genus-one

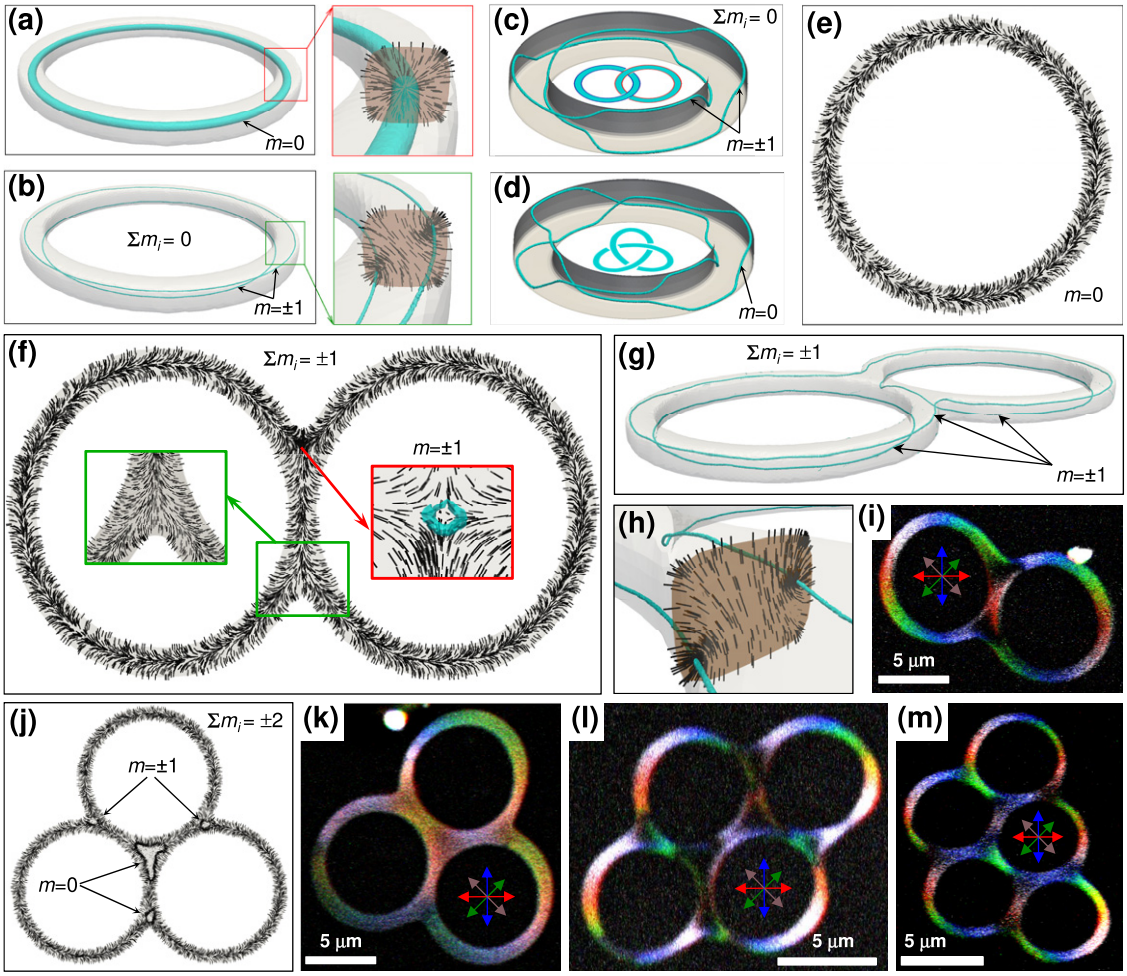

Figure 15. Handlebody-like LC drops with perpendicular boundary conditions. (a) and (b) Genus-one drops with (a) a single $s = 1$ and (b) two $s = 1/2$ disclination unknots, with isosurfaces of the reduced order parameter shown in blue, with the insets depicting $\mathbf{n}(\mathbf{r})$ in the drops' cross-sections. (c) A Hopf link and (d) trefoil $T(3,2)$ torus knot of half-integer disclination loops, with blue isosurfaces depicting regions of the reduced scalar-order parameter. (e) A torus-shaped drop with nonsingular 3D-'escaped' $\mathbf{n}(\mathbf{r})$. (f) Escaped $\mathbf{n}(\mathbf{r})$ structures depicted in the drop's midplane for a $g = 2$ drop. The insets show junction regions and blue tubes depict isosurfaces of the reduced order parameter. Hyperbolic hedgehog defect core and disclination loops with zero (green-framed) and unity (red-framed) topological hedgehog charges. (g) and (h) A $g = 2$ drop with singular defects depicted using blue isosurfaces of the reduced order parameter (g) and the corresponding cross-section of $\mathbf{n}(\mathbf{r})$ (h). (i) Experimental 3D polarized fluorescence texture for a $g = 2$ drop obtained by superimposing images with polarizations of probing light at 0° (red), 45° (green), 90° (blue) and 135° (pink); note the dark areas in junctions, where $\mathbf{n}(\mathbf{r})$ is perpendicular to the image. (j) Escaped $\mathbf{n}(\mathbf{r})$ in the midplane of a $g = 3$ drop. (k)–(m) Texture as in (i) but for $g = 3$, 4 and 5 drops, respectively; dark areas in junctions are regions where $\mathbf{n}(\mathbf{r})$ is perpendicular to the image planes. Reproduced with permission from [144].

rings, one can study linked particles with larger g and larger numbers of linked components. Beyond LCs, one can expect that linking will alter interactions between colloidal components when, for example, interactions originate from electrostatic or depletion forces [130, 131], opening a new avenue for colloidal self-assembly and functionality.

4.4. Knotted vortices in nematic drops

Similar to nematic colloids, LC drops are a useful platform for probing the relationship between surface confinement topology and defect structures in ordered media [55, 132–141]. The genus g of closed surfaces of micrometer-sized nematic drops can be experimentally varied (figure 14). The topological requirement that the net winding number of 2D surface defects in $\mathbf{n}(\mathbf{r})$ tangent to the LC droplet's surface adds to χ is effectively the same as for the colloids discussed above [30, 142]. Also, the hedgehog charges of bulk defects in the drop's interior need to add to $\pm\chi/2$ to compensate for the hedgehog charge of the drop's inner surface of given g [142]. Minimization of the total free energy selects stable and metastable states out of configurations satisfying these constraints. Therefore, by utilizing this interplay of topological invariants characterizing surfaces and fields, similar to what we discussed above for colloids, one can either avoid defect formation for drops of $g = 1$ [142, 143] or generate singular bulk and surface defects with well-defined topological invariants for $g > 1$. We shall see below how this allows for controllably obtaining line and point defects labeled as $\pi_1(\mathbb{S}^2/\mathbb{Z}_2) = \mathbb{Z}_2$ (bulk disclinations in the 3D director field), $\pi_1(\mathbb{S}^1/\mathbb{Z}_2) = \pi_1(\mathbb{S}^1) = \mathbb{Z}$ (surface defects in the 2D director fields at

LC-droplet interfaces) and $\pi_2(\mathbb{S}^2/\mathbb{Z}_2) = \mathbb{Z}$ bulk point defects in 3D $\mathbf{n}(\mathbf{r})$.

Let us start with drops in a polymer matrix imposing tangential boundary conditions for $\mathbf{n}(\mathbf{r})$. Figure 14(a) shows an array of torus-shaped $g = 1$ drops embedded in such a polymer matrix. Most of them contain defect-free concentric $\mathbf{n}(\mathbf{r})$, as expected for the confinement surface with $\chi = 2 - 2g = 0$ (figures 14(a) and (b)), though some drops contain self-compensating defect pairs (figures 14(a) and (c)) [142]. Although the Poincare–Hopf theorem [15] requires that the winding numbers s of defects at the LC–polymer interface add to χ, it does not prescribe particular ways to satisfy this constraint, which explains this diversity of topology-compliant configurations. For $g > 1$, millimeter-sized drops with handles were shown to contain boojums at droplet surfaces [143], in a way closely resembling how the topological constraints are satisfied for handlebody colloids with tangential anchoring (figure 8). Differently, micrometer-sized drops tend to exhibit (figures 14(d)–(g)) [142] half-integer disclinations spanning through the drop's volume. Defects in the inter-tori junctions are half-integer singular lines pinned to opposite parts of handlebody surfaces (figures 14(d)–(m)). Some of the drops contain the minimum numbers of half-integer defects needed for the net winding number to add to χ. For example, $g = 2$ drops have two half-integer bulk defect lines spanning the droplet's volume (figures 14(d)–(g)), so that the LC interface with a polymer matrix contains four such $s = -1/2$ surface defects in $\mathbf{n_s}(\mathbf{r})$ adding to $\chi = -2$ of the confining surface. Drops with $g = 3$ have at least four such half-integer bulk defects (figures 14(h)–(l)) terminating on eight surface defects in $\mathbf{n_s}(\mathbf{r})$, $g = 4$ drops have at least six and $g = 5$ drops at least eight bulk half-integer defects (figures 14(m) and (n)). The winding numbers of defects at the interfaces are thus always twice that of the sum of winding numbers of half-integer disclinations spanning within the LC bulk, always adding to the drop's χ when considering the winding numbers in $\mathbf{n_s}(\mathbf{r})$. In the larger drops with tens-to-hundreds micrometers sizes, boojums and half-integer defect lines can co-exist because they correspond to lower free energy depending on their locations within the drops. As the droplet size increases to millimeters [143], only boojums are stable because of the lower free energy of the corresponding $\mathbf{n}(\mathbf{r})$. The above examples show how, in addition to the appearance of boojums, the nonpolar nature of $\mathbf{n}(\mathbf{r})$ allows for satisfying the Poincare–Hopf and Gauss theorems through the emergence of surface-terminating bulk $\pi_1(\mathbb{S}^2/\mathbb{Z}_2) = \mathbb{Z}_2$ defect lines, which assure that the $\pi_1(\mathbb{S}^1/\mathbb{Z}_2) = \mathbb{Z}$ defects (associated with the end points of bulk defect lines) in the interfacial 2D director field $\mathbf{n_s}(\mathbf{r})$ add to χ. This scenario cannot be realized for vector fields which cannot host bulk defect lines in 3D because $\pi_1(\mathbb{S}^2) = 0$.

Handlebody-shaped nematic drops with perpendicular boundary conditions also reveal a large diversity of configurations, including ones with linked and knotted defect lines that form various knots [144] (figure 15). Singular disclinations shaped as unknots, knots and links, as well as half-skyrmions and other nonsingular structures emerge depending on geometric and material parameters. Surface topology and boundary conditions dictate the net topological hedgehog charge $m = \pm(1 - g)$ of defects in the nematic bulk of such drops, which, to assure the topological charge conservation, compensate the hedgehog charge of the field on the drop's inner confining surface, complying with the Gauss–Bonnet and Poincare–Hopf theorems [30]. One would therefore expect that the nematic interior of a single torus is topologically uncharged, $g = 2$ double-torus-confined drop hosts a defect of $m = \pm 1$ topological charge, and so on, where the sign of m depends on the choice of vectorization direction of $\mathbf{n}(\mathbf{r})$. However, the mathematical theorems again allow for 'flexibility' in satisfying these constraints while also minimizing free energy. This leads to many topologically nontrivial configurations that can be selected as energetically stable and metastable structures [144]. For example, $g = 1$ drop surfaces can induce a single integer-strength disclination loop (topologically unstable, but energetically stabilized), two half-integer disclination loops, or nonsingular solitonic 'escaped' $\mathbf{n}(\mathbf{r})$ (figures 15(a)–(e)), depending on geometric and material parameters. While the hedgehog charges m (marked on figure parts) of disclination loops and knots add to zero (figures 15(b) and (d)), these results illustrate how loops and knots of $s \in \mathbb{Z}_2 = \pi_1(\mathbb{S}^2/\mathbb{Z}_2)$ disclinations can yield different effective $m \in \mathbb{Z} = \pi_2(\mathbb{S}^2/\mathbb{Z}_2)$ hedgehog charges to satisfy topological constraints under different free-energy-minimizing conditions. As examples, figure 15(c) shows a Hopf link of two half-integer disclination loops and figure 15(d) depicts a trefoil knot of a single half-integer defect line, which are both permitted configurations for nonpolar $\mathbf{n}(\mathbf{r})$. For large drops, escaped director structures with nonsingular solitonic $\mathbf{n}(\mathbf{r})$ are energetically favorable (figures 15(e) and (f)). Drops of higher genus stabilize even larger combinations of multiple singular disclination loops and solitonic configurations supplemented with additional point and disclination loop defects (figures 15(f)–(m)). While hedgehog charges always add to $\pm\chi/2$, the particular defects that occur are selected as free-energy minima for given conditions. Three half-integer disclination loops form in small drops of $g = 2$ (figures 15(g) and (h)), with one running along the whole drop's perimeter and the other two encircling the holes. One disclination loop winds around the largest perimeter and g small loops encircle holes for $g > 2$ (figures 15(g) and (h)). For larger $g \geqslant 2$ drops, the 'escaped' director profiles appear instead of defect rings (figures 15(f) and (i)–(m)), yielding point defects or small disclination loops localized in the drop's junction regions.

When droplet dimensions increase to hundreds of micrometers and millimeters, different kinds of behavior are observed, which were recently explored by Fernandez-Nieves and colleagues [143, 145]. For example, double-twisted toroidal configurations arise in drops with $g = 1$ as a result of saddle-splay LC elasticity, and splay and bend deformations are often substituted by twist deformations due to lower energetic costs [143, 145]. When a chiral nematic LC is used, depending on the relative dimensions of droplets and cholesteric pitch, knotted structures of entangled disclination lines can appear, even in spherical drops [140], which can also feature constellations of high-charge point defects with hedgehog charges still adding to ± 1 [146, 147].

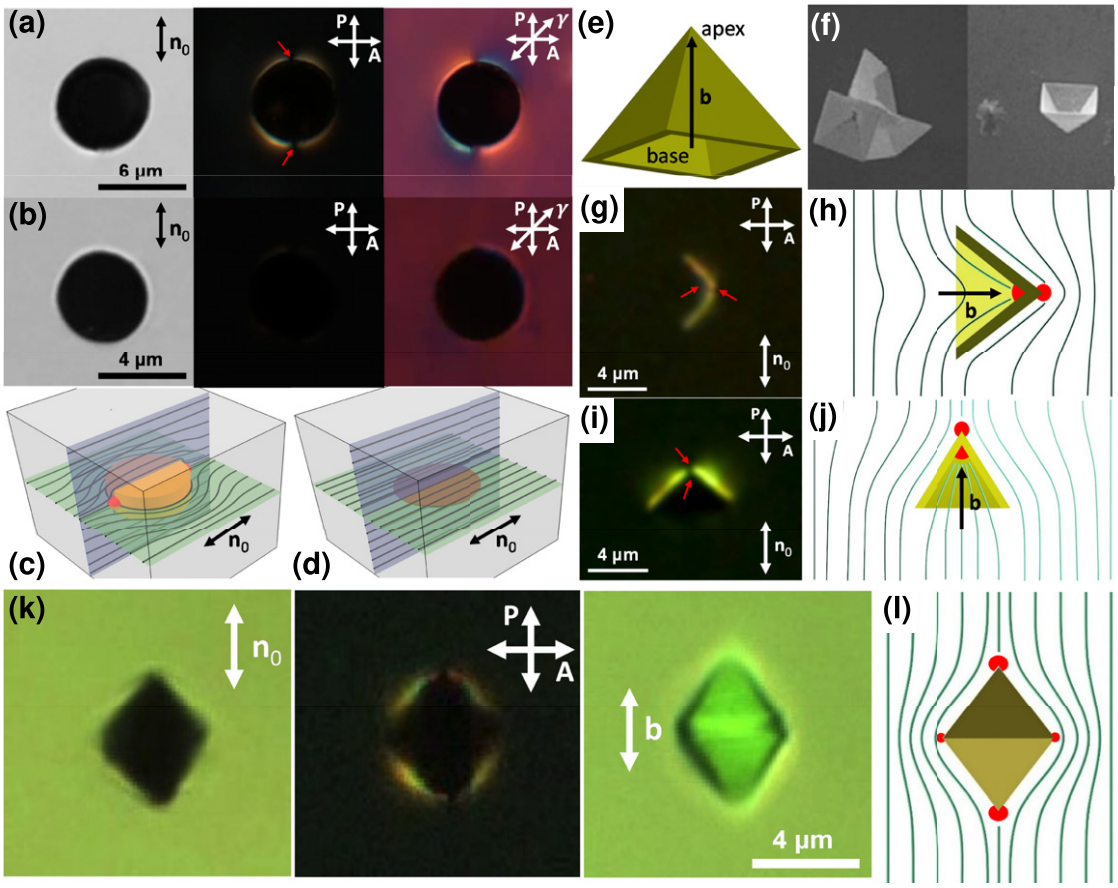

Figure 16. Colloidal analogs of mathematical surfaces with boundaries. (a) and (b) Optical images of discs made of (a) thick foil with thickness $h_f \approx 1$ μm and (b) thin foil with $h_f \approx 100$ nm obtained in (left) bright-field and polarizing imaging modes (middle) without and (right) with a 530 nm retardation plate with a fast axis γ inserted between the crossed polarizer (P) and analyzer (A); red arrows in (a) indicate boojums. (c) and (d) Schematics of $\mathbf{n}(\mathbf{r})$ around (c) thick and (d) thin foils, with boojums in (c) depicted as red hemispheres. (e)–(j) Colloidal pyramidal cones in a nematic LC: (e) a schematic; (f) scanning electron micrographs of pyramids made from gold foil with (left to right) $h_f \approx 100$ nm and 200 nm; (g) a polarizing optical micrograph and (h) a schematic of $\mathbf{n}(\mathbf{r})$ and defects around particles oriented with a base-tip vector $\mathbf{b} \perp \mathbf{n}_0$. (i) A polarizing micrograph and (j) $\mathbf{n}(\mathbf{r})$ and defects around pyramids with $\mathbf{b} \| \mathbf{n}_0$. Red fragments of spheres in (h) and (j) show the fractional boojums; red arrows indicate the boojums in (g) and (i). (k) Bright-field (left), polarizing (middle) and reflection (right) optical micrographs showing a colloidal octahedron formed through the assembly of two pyramidal cones in a nematic LC, with $\mathbf{n}(\mathbf{r})$ and surface defects (red) depicted in (l). Reproduced with permission from [155].

A spectacular property of confined nematic systems is the diversity of structures satisfying topological constraints imposed by mathematical theorems for given topology and boundary conditions, which largely stems from the nonpolar nature of $\mathbf{n}(\mathbf{r})$. All half-integer defect lines would be disallowed in polar systems, thus precluding the appearance of knotted and linked defects and highly reducing the number of topologically admissible structures. The fact that the nature of nematic fields allows for singular linked, knotted and other configurations is important beyond soft matter because nonpolar fields in cosmology and in other physical systems often host defects topologically similar to nematic disclinations (cosmic strings), although much less accessible experimentally [50, 148, 149]. The confined nematic studies could be extended to thin LC shells formed by handlebody surfaces, an emergent research area where most studies so far focus on spherical shells [141, 150–153]. In addition to fundamental importance, this behavior may be of interest for multistate optically addressed topological memory devices [154] that can allow for recording and reading information through laser-writing different topology-satisfying field configurations within drops of controlled genus.

4.5. Surfaces with boundary and surface-bound defects

Surface genus and (related to it) Euler characteristics are not the only topological surface properties defining interactions with LCs [36, 155, 156]. Colloids can also serve as physical analogs of a mathematical surface with boundary [30], interacting with $\mathbf{n}(\mathbf{r})$ without inducing defects [155]. Such colloids were recently experimentally demonstrated in the embodiment of very thin nanofoils [155]. Disc-shaped flat nanofoils with tangential boundary conditions and thickness h_f spontaneously align with large-area faces parallel to $\mathbf{n}_0$ while freely rotating around it (figures 16(a)–(d)). They induce two surface boojums [74, 104, 105, 157] when $h_f \approx 1$ μm (figure 16(a)), but not for $h_f \approx 100$ nm when no defects are optically detectable (figure 16(b)). Overall, the LC–foil

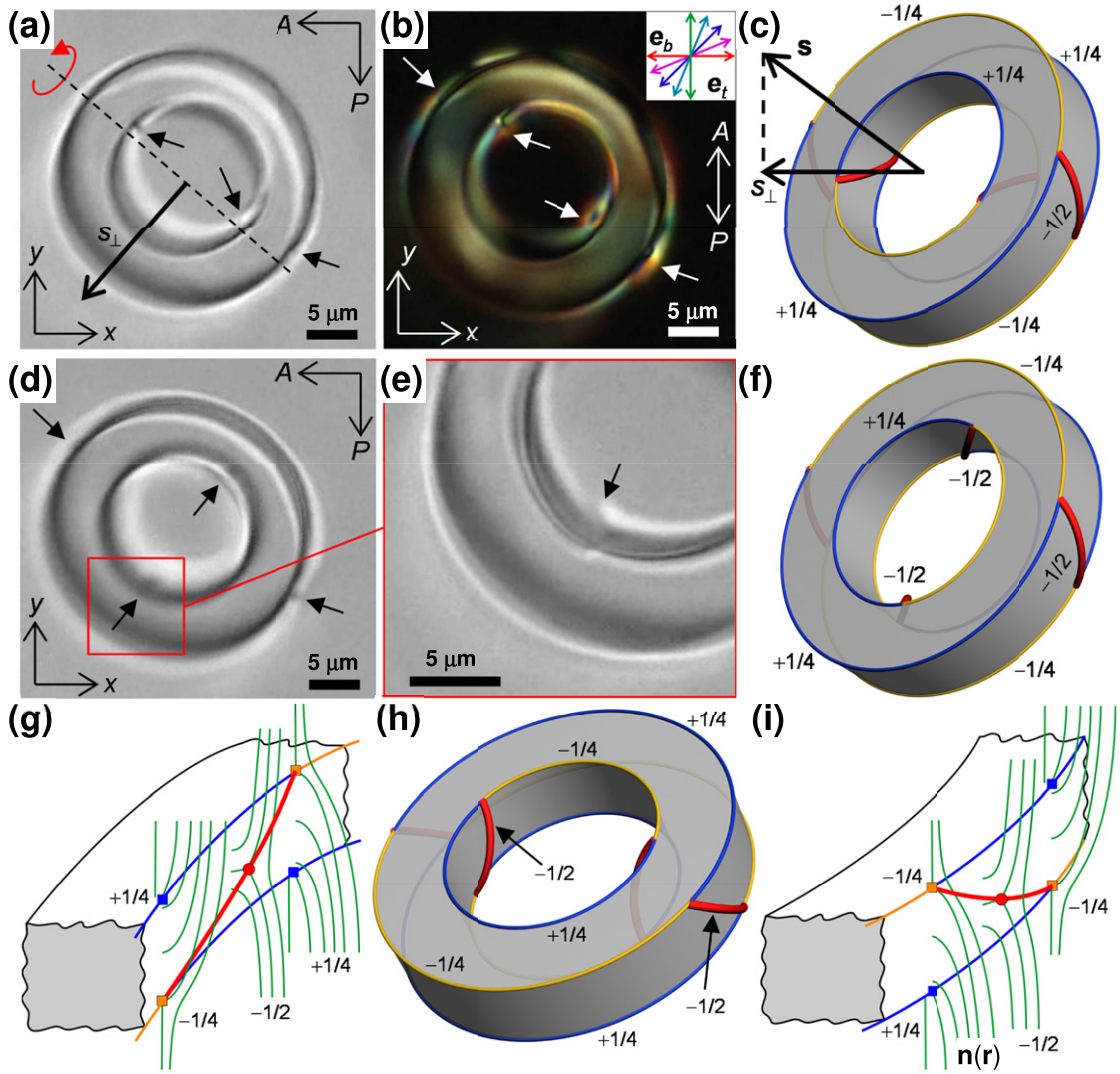

Figure 17. Edge-pinned defect lines induced by a faceted ring particle in a twisted nematic cell. (a), (b), (d) and (e) Optical micrographs obtained between crossed (a), (d) and (e) and parallel (b) polarizers labeled with 'P' and 'A'. A pair of bulk half-integer defects (shown by black arrows) is visible inside the ring. The inset in (b) shows the twist of $\mathbf{n}(\mathbf{r})$ between the orthogonal easy axes $\boldsymbol{e}_b$ and $\boldsymbol{e}_t$ at the confining cell substrates. (e) A zoomed-in view of the bulk defect line seen in (d) while traversing from one particle's edge to another. (c) and (f) Schematics of defects and their transformation corresponding to (a) and (d), respectively. Handle-shaped bulk defect lines are shown as thick red tubes. Quarter-strength edge-bound surface defect lines of opposite strengths (in terms of their 2D cross-sections) are shown using thin blue and orange lines, with strengths of opposite signs marked next to them. (g)–(i) Schematics of $\mathbf{n}(\mathbf{r})$ (green lines) and defects in the region of transformation of disclinations inside the ring opening (g) and outside (i) of a toroidal particle with a faceted square cross-section (h). Thick red lines are handle-shaped bulk defects; blue and orange lines are quarter-strength edge-bound surface defect lines of strengths with opposite signs marked next to them. Reproduced with permission from [70].

interactions are determined by a competition of bulk elastic and surface-anchoring energies at the nanofoil perimeter, which is characterized by the anchoring extrapolation length ξ_e [155]. When $h_f \ll \xi_e$, e.g. for $h_f \leqslant 100$ nm (figure 16(b)), thin-foil particles behave as colloidal analogs of orientable surfaces with boundaries that induce no defects (figures 16(b) and (d)). Interestingly, particle-induced boojums with fractional geometry-defined hedgehog charges of opposite signs are found when these surfaces with a boundary are shaped into hollow pyramids without a base, the pyramidal cones (figures 16(e)–(j)) [155]. The pyramids spontaneously align with the base-tip vectors $\mathbf{b}$, either parallel or perpendicular to $\mathbf{n}_0$ [155]. The particle geometry causes director distortions revealed by polarizing micrographs (figures 16(g)–(j)), with the boojum defects at the apex points of inner and outer surfaces of hollow pyramids. Mapping vectorized $\mathbf{n}(\mathbf{r})$ onto a 2D sphere $\mathbb{S}^2$ does not fully cover it, and the ratio of the covered and total areas of $\mathbb{S}^2$ gives the fractional charge m_b. For these colloidal surfaces with boundaries, one finds self-compensation of hedgehog charges associated with inner and outer boojums (figures 16(h) and (j)) [155]. Colloidal interactions between pairs of nanofoil-based colloidal pyramids emerge from the minimization of elastic free energy, typically resulting in nested assemblies [155, 157–159]. Formation of hollow octahedrons (figures 16(k) and (l)) is an example of colloidal assembly that leads to transformation of two

pyramid-shaped surfaces with a boundary into a single closed surface without a boundary, which then becomes compliant with the Poincare–Hopf theorem. Indeed, winding numbers of boojums at vertices add to the octahedron's $\chi = 2$ (figure 16(i)). Since extensions of the Poincare–Hopf theorem for surfaces with boundaries are known only for special cases [30], experimental embodiments of such surfaces in LC–colloidal systems are fundamentally important. Because all surfaces are characterized (up to homeomorphism) by genus, orientability and the number of boundary components, as stated by the classification theorem [30], these colloids expand the scope of experimental topology. In addition to thin metal foils (figure 16), LC colloids with boundaries can be made out of 2D materials, like graphene and graphene oxide [156].

Another interesting regime of interactions arises between the director field and surface boundary conditions on geometrically and topologically nontrivial particles with sharp corners. Using examples of faceted ring-shaped particles of $g = 1$ [70], figure 17 demonstrates examples of inter-transformation of induced defect lines as they migrate between locations in the bulk of the nematic host and edge-pinned locations at particle surfaces. This behavior, also compliant with topological constraints [70], is enriched by the diversity of surface-pinned defect lines that appear for facetted particles because the winding number of such defect lines at LC surfaces is not constrained to be a half-integer or integer and can be fractional, similar to the fractional boojums induced by pyramidal cones that we discussed above [70]. In addition to common half-integer defect lines encircling and entangling spherical and topologically nontrivial particles, surface quarter-strength defect lines are commonly pinned to sharp edges of faceted particles [70]. Nodes of defect lines with different strengths often form, of which some are pinned to colloidal surfaces while others are the bulk defect lines only adhering to surfaces at their end points. The winding number of individual surface-pinned disclinations around colloidal particles is unconstrained and can be controlled by the geometry of colloidal inclusions while the overall topological characteristics of particle-induced defects comply with topological theorems [70]. A key feature of the particles showing such behavior is that the smallest particle's dimension is much larger than the surface-anchoring extrapolation length [70], yielding strong boundary conditions that cannot be violated at sharp edges of faceted particles. Such nematic colloids exhibit director configurations with splitting and re-connections of singular defect lines, prompted by colloidal particles with sharp edges and strong boundary conditions (figure 17). This shows how the diversity of topological defects can be expanded by invoking fractional surface disclinations patterned with a particle's sharp geometric feature shapes. The transformations of bulk and surface defect lines induced by faceted colloids diversify the elasticity-mediated colloidal interactions and can potentially enrich their controlled reconfigurable self-assembly.

Two examples of colloidal surfaces in this section illustrate the importance of geometry and topology of colloidal surfaces in defining the behavior of nematic colloids and various confined systems. While geometry and topology are also important for conventional colloids [91], their role is truly defining for nematic colloids and drops because of defining the formation of defects, elastic distortions, elasticity-mediated interactions, self-assembly and so on.

5. Topological solitons in LCs and colloids

5.1. 2D skyrmions

Similar to many other branches of physics and cosmology, soft condensed matter systems like LCs and colloids can host a large variety of topological solitons and related spatially localized nonsingular structures. For example, the LCs host a variety of 2D merons (figures 18(a) and (b)) and skyrmions (figure 18(c)) [32, 160–170], where the latter are particle-like low-dimensional analogs of Skyrme solitons in particle physics [7]. When embedded in 3D samples, these 2D Skyrme solitons have topologically protected translationally invariant 2D tube-like structures (figures 18(c) and (d)) that cannot be eliminated from a uniformly oriented background without destroying the order or introducing singular defects. Not enjoying this type of topological protection, tubes of merons, also known as fractional skyrmions (figure 18(a)), have a long history in the LC research field. In fact, some of the earliest reports on LCs dealt with chiral phases in cholesterol derivatives, including the so-called 'blue phase' [12, 171–174]. These phases are various crystalline arrays of double-twist tubes that are fractional skyrmions (merons) [160–170], including cubic and hexagonal lattices [163, 164, 173]. Rod-like molecules in a fractional skyrmion tube are parallel to its axis at the center, twisting radially outwards to form barber-pole-like patterns on concentric cylindrical surfaces (figure 18(a)). Full LC skyrmion tubes, with such a 180° radial twist from the central cylinder's axis to the periphery, contain all possible molecular orientations and embed in a uniform far-field background (figures 18(c) and (d)) [160]. Historically, many structures were found to have such a radial π-twist from center to periphery in certain localized regions, but they were typically not 2D translationally invariant, often transforming into and co-existing with singular defects. Recently, researchers identified conditions needed for the stability of 2D skyrmions as topologically distinct objects with translational invariance [79, 161].

Solitonic LC $\mathbf{n}(\mathbf{r})$ structures can be vectorized to give a smooth vector configuration (figures 18(d)–(f)), which then has the $\mathbb{S}^2$ order parameter space and is similar to skyrmions in the magnetization field of magnets that drive much excitement in spintronics, including for data storage [175–182]. Recent studies have demonstrated that the density of such stored information could be increased using skyrmions with varying topological degrees (whose distinction is topologically protected) [160]. LCs provided insights into how high-degree skyrmionic structures can form [160] as stable chiral composite skyrmion bags. To realize them, one places multiple single antiskyrmions (each with degree $+1$) next to each other within a stretched skyrmion, thus forming the skyrmion bags (figures 18(g)–(j)) [160]. Moreover, multiple nested structures can be formed with, say, antiskyrmion bags within skyrmion

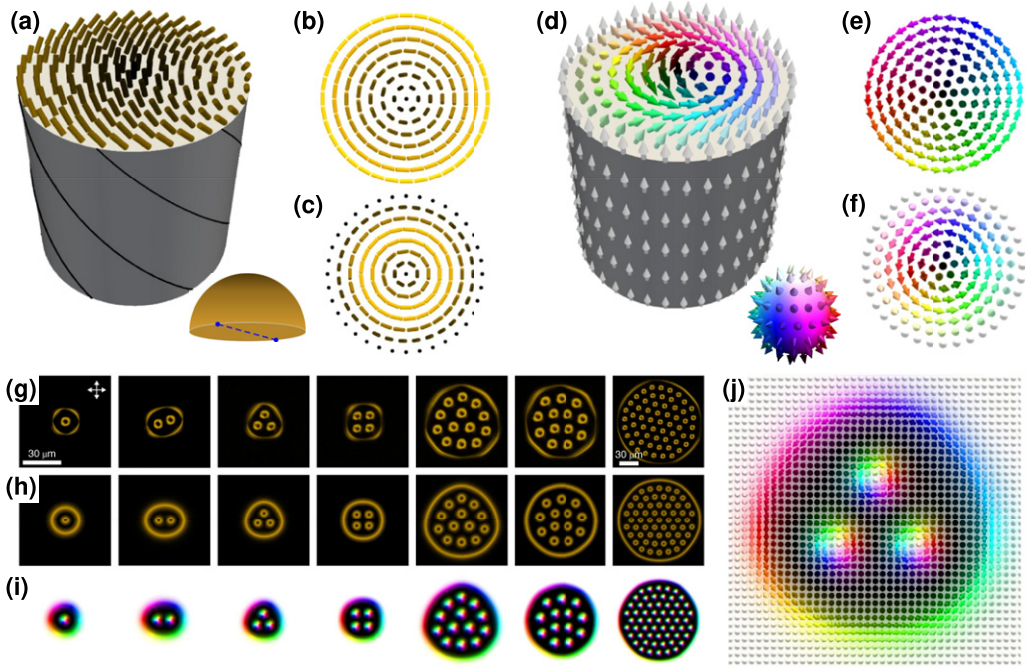

Figure 18. The 2D skyrmions and skyrmion bags. (a) A translationally invariant quarter-skyrmion tube with $\mathbf{n}(\mathbf{r})$ shown by rods colored based on orientations. The inset shows a color scheme for the nonpolar $\mathbf{n}(\mathbf{r})$ used in (a)–(c) and determined by director orientations as mapped to $\mathbb{S}^2/\mathbb{Z}_2$ in the inset of (a). (b) and (c) Top views of a half-skyrmion (b) and an elementary full LC skyrmion (c). (d) A translationally invariant skyrmion tube visualized by colored arrows smoothly decorating $\mathbf{n}(\mathbf{r})$ based on $\mathbb{S}^2$ shown in the bottom-right inset. (e) and (f) Top views of a vectorized-field half-skyrmion (e) and a full skyrmion (f). (g) Polarizing optical micrographs of skyrmion bags with one-to-four antiskyrmions inside, two stable conformations of the bag with 13 antiskyrmions inside and the bag with 59 antiskyrmions within it. (h) and (i) Computer-simulated counterparts of the skyrmion bags in (g) depicted according to the insets in (a) and (d), respectively. Crossed polarizers for (g) and (h) are marked by white double arrows in (g). (j) A close-up view of a computer-simulated bag with three antiskyrmions shown by colored arrows. Reproduced with permission from [160].

bags and skyrmions within them, and so on [160]. This yields nonsingular skyrmionic structures with arbitrary degrees and of both positive and negative signs because this design allows for wrapping and unwrapping $\mathbb{S}^2$ by mapping $\mathbf{n}(\mathbf{r})$ from the sample's 2D plane by controlled numbers of times in a non-alternating fashion [160]. The total degree of a bag with N_A antiskyrmions is $N_A - 1$. More complex structures with antiskyrmion bags inside skyrmion bags have a net degree $N_A - N_S$, where N_S is the total number of skyrmions; counting N_S and N_A also includes the nested skyrmion and antiskyrmion bags. Skyrmions and skyrmion bags in LCs require careful selection of experimental conditions and materials to assure stability [79], where important roles are played by soft but well-defined perpendicular boundary conditions on confining surfaces, elastic anisotropy, confinement, etc.

The relation of 2D skyrmions to knots might not be apparent when examining their structure. After all, the knots reviewed in section 3 are intrinsically 3D in nature. However, skyrmions are topologically protected and, just like knots, cannot be eliminated or inter-transformed without cutting: skyrmions cannot be eliminated without destroying continuity of order within the LC. Moreover, skyrmions and related structures can be part of knotted field configurations. For example, Sutcliffe showed that knotted skyrmions can arise as energy minima in frustrated magnets [26]. On the other hand, the heliknotons (structures emerging within a helical field, which will be discussed below) comprise knots of fractional skyrmions [73]. We will also see below how emergent behavior of chiral LCs leads to various types of knotting as a result of the interplay of skyrmionic configurations with confinements and applied external fields [32, 81, 169]. In the bulk of chiral LCs and magnets, minimization of free energy can also lead to lattices of orthogonally oriented skyrmions in helical and conical backgrounds, which was already observed via direct optical imaging in LCs and for which there is also indirect evidence from neutron scattering experiments in solid-state magnets [183].

5.2. *Torons with skyrmions and knots within them*

In a geometry similar to that used for observing skyrmions and skyrmion bags [79, 160, 161], discussed above, one can also observe structures with both skyrmion-like and Hopf and Seifert fibration features when a chiral LC with a ground-state pitch p_0 is confined by substrates treated for perpendicular alignment [32, 81, 169]. When the separation gap d of the confining planes is approximately equal to p_0, the LC's tendency to twist is incompatible with the strong perpendicular boundary conditions. In this frustrated geometry, numerous localized solitonic configurations emerge within the background of unwound $\mathbf{n}_0$ [32, 79, 81, 184]. These solitonic configurations incorporate energetically-favorable localized twist while meeting boundary conditions, and can be controlled using laser tweezers in both nonpolar chiral LCs [32]

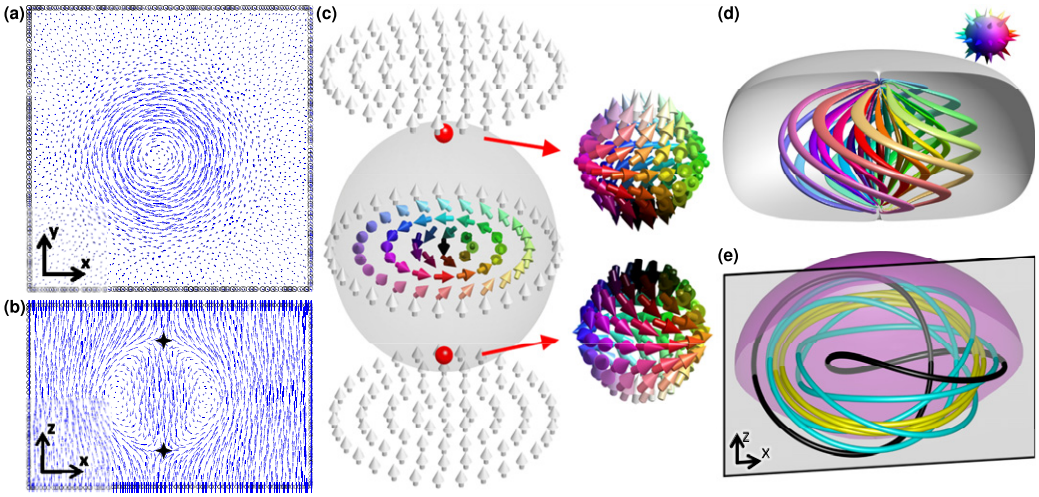

Figure 19. The 3D structure and topology of elementary LC torons. (a) and (b) Computer-simulated cross-sections of an axisymmetric elementary toron shown in (a) a plane orthogonal to $\mathbf{n}_0$ and (b) containing $\mathbf{n}_0$. (Reproduced with permission from [81].) (c) An elementary toron is a skyrmion terminating at the two point defects (red spheres) to meet uniform surface boundary conditions and match the topologically nontrivial skyrmion tube with the uniform far-field background of the 3D LC sample. Detailed field configurations on spheres around the point defects are shown as right-side insets. (Reproduced with permission from [79].) (d) Toron's preimages of $\mathbb{S}^2$-points (inset, shown as cones), with regions where preimages meet corresponding to point defects. (e) Closed-loop $\mathbf{n}(\mathbf{r})$-streamlines within the toron at different distances from its circular axis form different torus knots and links. Reproduced with permission from [81].

and chiral LC ferromagnets [185]. The simplest such configuration is known as an elementary toron (figure 19), which can be thought of as a degree-one skyrmion terminating on point defects near substrates with perpendicular boundary conditions [79]. In the cell midplane between confining substrates, the elementary toron embeds a π-twist of $\mathbf{n}(\mathbf{r})$ radially from the center in all directions (figures 19(a)–(c)) and smoothly meets the $\mathbf{n}_0$-periphery [79]. This skyrmionic configuration within the LC bulk terminates at two singular point defects near substrates (figures 19(b) and (c)). Vectorized $\mathbf{n}(\mathbf{r})$ from the toron's midplane cross-section (figure 19(c)) maps to fully cover $\mathbb{S}^2$ once (inset of figure 19(d)), as for an elementary skyrmion. This skyrmion tube, however, terminates at point defects that match it to the uniform boundary conditions at surfaces (figures 19(b)–(d)). Both top and bottom defects are self-compensating elementary hedgehogs of opposite charge in vectorized $\mathbf{n}(\mathbf{r})$ and, like elementary skyrmions, are labeled by $\pi_2(\mathbb{S}^2) = \mathbb{Z}$ ($\pi_2(\mathbb{S}^2/\mathbb{Z}_2) = \mathbb{Z}$ for the nonpolar case) [79]. It is therefore natural that the elementary skyrmion tube orthogonal to the cell substrates is terminated (embedded in a uniform, topologically trivial background) by the two point singularities, consistent with the notion that the spatial translation of a $\pi_2(\mathbb{S}^2) = \mathbb{Z}$ point singularity can leave a trace of a $\pi_2(\mathbb{S}^2) = \mathbb{Z}$ topological soliton within the locally perturbed background $\mathbf{n}_0$ [74].

Torons have structural features that bring about the resemblance of not only skyrmions, but also the Hopf and Seifert fibrations, which can be seen by probing streamlines tangent to $\mathbf{n}(\mathbf{r})$ (figures 19(e) and 20). These streamlines form various torus knots, like those found in toroidal DNA drops [136, 186]. Regions near the toron's circular axis resemble fragments of $\mathbb{S}^3$ to $\mathbb{R}^3$ stereographic projection [81]. Like in toroidal DNA drops [186], this implements the LC's tendency to twist while forming an axisymmetric configuration. Differently from biopolymer drops, the toron's $\mathbf{n}(\mathbf{r})$-twist rate changes smoothly as one moves away from its axis, accommodating the effects of confinement and presence of the singular defects, so that different torus knots form (figure 19(e)). Incompatible with Euclidian 3D space [186], the 3D twist is inherently frustrated, but the geometry of fiber bundles shows how the LC embeds it into the toron's volume [186]. Knots $T(p_T,q_T)$ can be related to Hopf and Seifert fibrations with different twist properties and can be visualized with a series of streamlines of $\mathbf{n}(\mathbf{r})$. The toron configuration has spatially varying director distortions deviating from the idealized 3D twisted structure that one could obtain by the stereographic projection, so that both the rate of the twist and the formed $T(p_T,q_T)$ knots of streamlines depend on the location within a toron. This is because the toron combines the favorable 3D twisted region with some bend and splay distortions that aid in embedding the twisted director configuration into a uniform far field while minimizing the overall free energy. Within a toron (figure 20), one finds Hopf links $T(1,1)$, trefoil $T(3,2)$, pentafoil $T(5,3)$, quatrefoil $T(3,4)$ and other torus knots formed by the streamlines (figure 20). As the electric field morphs the toron (figures 20(a)–(e)), different knots on torus surfaces never pass through each other (figures 20(e)–(g)), but the contour lengths of the closed-loop knots increase with voltage (figures 20(c)–(e)). While the elementary toron is a skyrmion tube terminated on point defects, it also has an interpretation inspired by the torus-knot-like streamlines tangent to $\mathbf{n}(\mathbf{r})$. One can think of it as a half-skyrmion double-twist tube (or a tube of twist-escaped integer-strength line) forming a circular loop and compensated near substrates by a pair of hyperbolic point defects [32] (figure 20(h)). It has been shown that the point defects within these torons can open up into singular half-integer defect loops [32]. Therefore, within the 2D

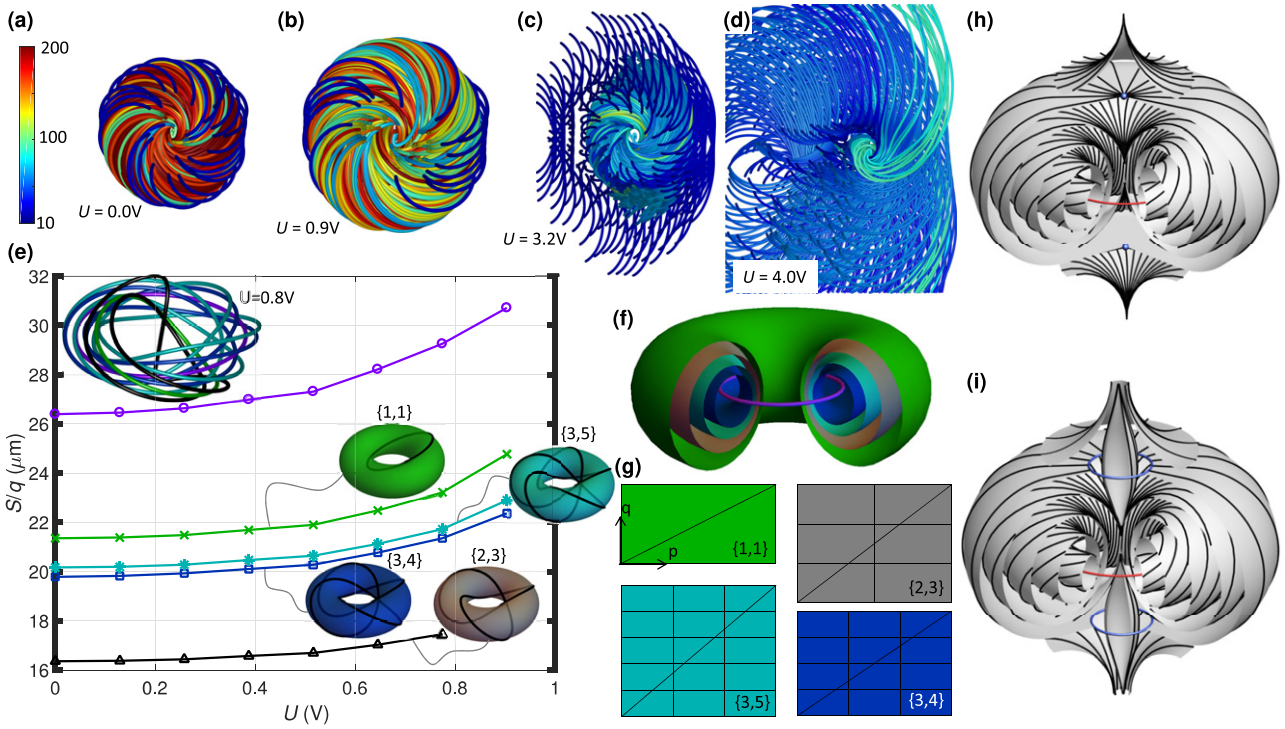

Figure 20. Torus knots in director streamlines within torons. (a)–(d) Streamlines tangent to $\mathbf{n}(\mathbf{r})$ at applied voltages U, with lengths depicted according to the color scheme, with the blue (red) colors representing the short (long) ones. (e) The contour length of streamlines normalized by the winding number of the torus knots S/q versus U. The top-left inset shows examples of tracked torus knots and unknots at $U = 0.8$ V. The top purple curve (circles) is the circumference of the circular axis. Crosses, asterisks, squares and triangles mark the length of the Hopf unknot and pentafoil, quatrefoil and trefoil knots, respectively. The torus knots tracked each have insets representing their topology and the torus-knot winding numbers, with the corresponding U-dependencies of the contour lengths. (f) Torus surfaces where the respective torus knots and unknots are found, including the circular axis. (g) Rectangles schematically represent unwrapped tori shown in (f) with the same colors. Thin black lines indicate the streamlines that loop around the two axes of the torus to form various knots. (a)–(g) Reproduced with permission from [81]. (h) A schematic of a triple-twisted toron configuration consisting of two point defects (blue dots) and a twist-escaped disclination loop (red line in the midplane). (i) A different toron configuration with two half-integer defect rings replacing the point defects compared to that shown in (h). (h) and (i) Reproduced with permission from [32].

axially symmetric cross-section of a toron with two such singular loops (figure 20(i)) [32], the half-skyrmion (also known as meron and also twist-escaped integer-strength line) is compensated by two singular defect lines in a way similar to what has also been shown for individual linear half-skyrmions embedded into a uniform background and periodic lattices [166]. The overall structure of torons evolves with changing parameters and, under different realization conditions, brings about analogies with not only 2D skyrmions and half-skyrmion loops (or double-twist tori as opposed to double-twist tubes), but also with Hopf fibration in the streamlines tangent to $\mathbf{n}(\mathbf{r})$ [169]. Depending on the pitch p_0, sample thickness d, elastic constants and applied fields, the elementary toron's lateral extent relative to p_0 and 3D shape vary, so that one or the other of these mutually equivalent descriptions of torons is used [81].

Torons have been generated by laser tweezers and means such as temperature quenching from an isotropic phase both as individual objects and in periodic arrays [170, 187, 188], with and without lattice defects. Toron lattices have been used as diffractive optical elements, whereas lattices with edge dislocations could be utilized as generators of optical laser vortices [163]. These lattices with and without lattice defects could be reconfigured or erased by applying external electric fields, showing how topologically nontrivial knotted objects in soft matter can be utilized in various photonic, electro-optic and singular optics applications [163]. In addition to chiral LCs, torons have been theoretically predicted to exist in solid-state magnetic systems [189]. While types of torons with loops of half-integer singular lines can exist in LCs with nonpolar $\mathbf{n}(\mathbf{r})$ (figure 20(i)), they are disallowed in vector fields of colloidal and solid-state magnets, where only the structures with point defects have been observed (figures 19(a)–(c) and 20(h)) (which is because half-integer disclinations cannot exist as standalone objects in vector fields, where $\pi_1(\mathbb{S}^2) = 0$) [185, 189]. Another localized topological object, dubbed a 'hopfion' [24], has a fully nonsingular structure spatially confined in 3D and can also exist in both polar and nonpolar fields, as we shall see next.

5.3. Hopfions in ferromagnetic colloidal fluids

The topological Hopf soliton, also called a 'hopfion', was recently observed experimentally and modeled numerically in magnetic fluids formed by colloidal dispersions of magnetically monodomain platelets within a chiral nematic host [24]. This soliton contains knotting of the order parameter that can be described by utilizing the concept of 'preimage', the

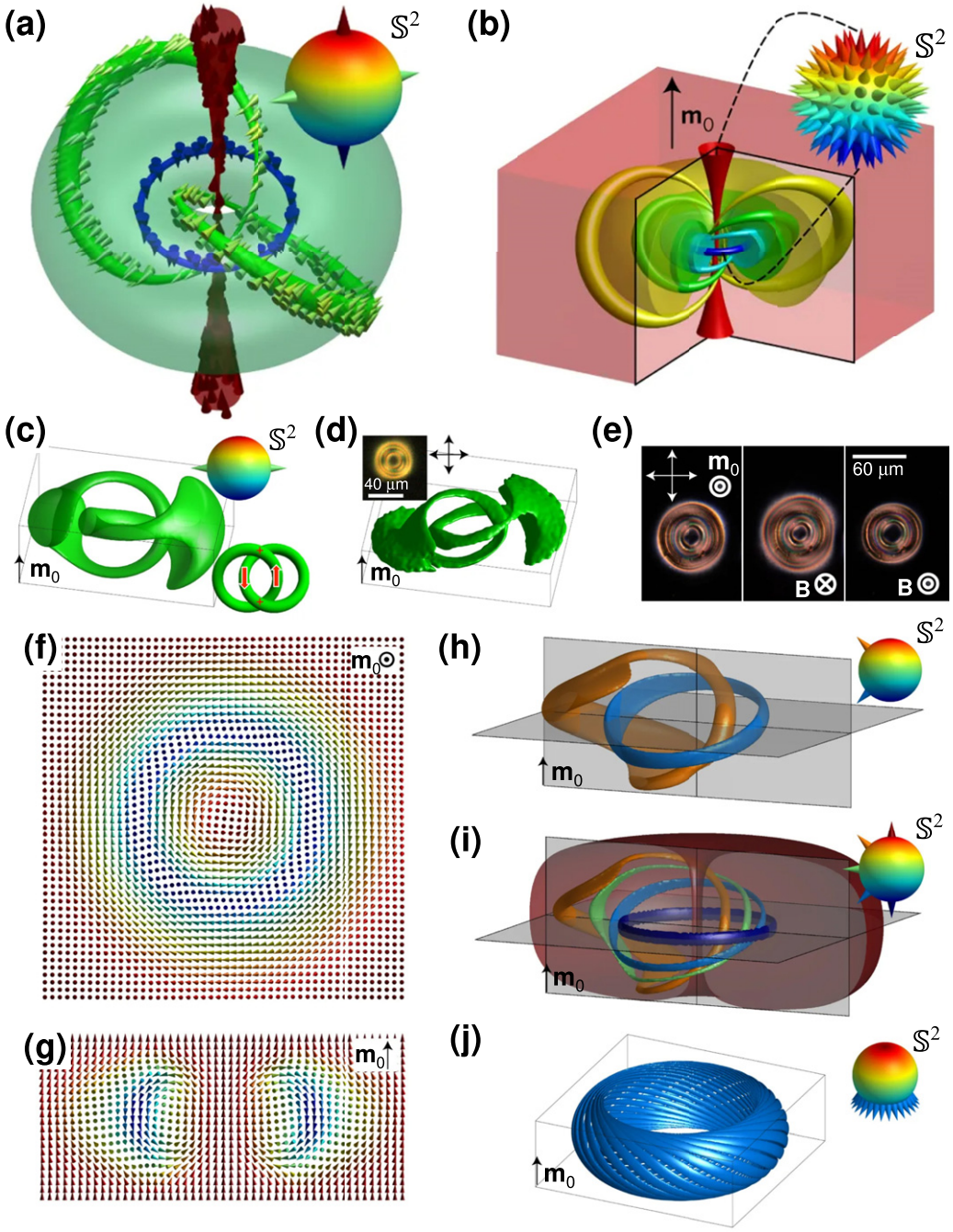

Figure 21. Hopfions in chiral colloidal ferromagnetic LCs. (a) Linking of a hopfion's circle-like closed-loop preimages of points (cones) on $\mathbb{S}^2$. (b) An illustration of a Hopf map of closed-loop preimages of a hopfion embedded in a far field $\mathbf{m}_0$ onto $\mathbb{S}^2$. (c) and (d) Computer-simulated and experimental preimages, respectively, of two diametrically opposite $\mathbb{S}^2$ points (cones) in the top-right inset of (c). The bottom-right inset in (c) shows signs of the crossings and circulation directions that determine the linking of preimages. The inset in (d) is a polarizing optical micrograph of a hopfion. (e) Polarizing optical micrographs showing the polar response of hopfions in a c ferromagnetic LC, which expand (middle) and shrink (right) compared to their zero-field equilibrium size (left) when the magnetic field is antiparallel or parallel to $\mathbf{m}_0$, respectively. (f) and (g) Cross-sections of the hopfion taken in a plane orthogonal to $\mathbf{m}_0$ (f) and in a plane containing $\mathbf{m}_0$ (g), with the vector field shown using cones colored according to $\mathbb{S}^2$ shown in the insets of (a) and (b). (h) and (i) Linking of preimages of (h) two and (i) five representative points on $\mathbb{S}^2$, including south- and north-pole preimages (the latter corresponds to $\mathbf{m}_0$ and is the exterior of the torus confining all other preimages). (j) Preimages of the $\mathbb{S}^2$-points of constant polar but varying azimuthal $\mathbf{m}(\mathbf{r})$ orientations form a torus. Reproduced with permission from [24].

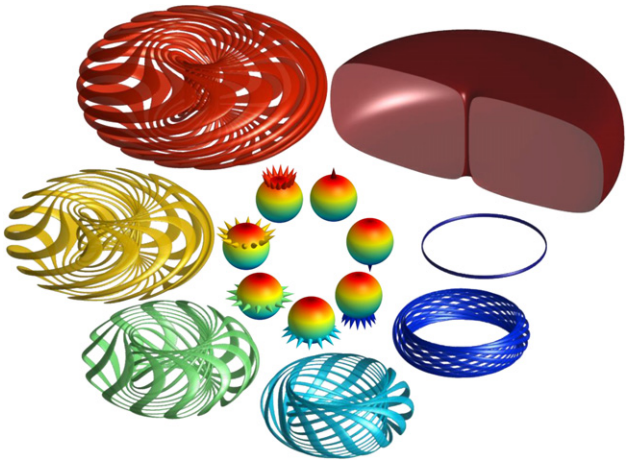

Figure 22. Tiling and linking of preimages of $\mathbb{S}^2$ points within a hopfion. Preimages of different azimuthal $\mathbf{m}(\mathbf{r})$-orientations tile into tori for the same polar angles, with the smaller tori nesting inside bigger tori; the largest torus contains the north-pole preimage in its exterior corresponding to $\mathbf{m}_0$ and the other preimages nested within its interior.

spatial region of the ferromagnet's 3D space with a single unit magnetization field $\mathbf{m}(\mathbf{r})$ orientation corresponding to a single point on $\mathbb{S}^2$ (figure 21(a)). For hopfions, preimages of all $\mathbb{S}^2$ points are closed loops [7] (figures 21(a) and (b)). Imbedding into a uniform $\mathbf{m}_0$ and localizing in three spatial dimensions (figure 22), hopfions are classified on the basis of maps from $\mathbb{R}^3 \cup \{\infty\} \cong \mathbb{S}^3$ to the ground-state manifold $\mathbb{S}^2$ of 3D unit vectors, $\pi_3(\mathbb{S}^2) = \mathbb{Z}$ [7]. Topologically distinct hopfions are characterized by the Hopf index $Q \in \mathbb{Z}$ with a geometric interpretation of the linking number of any two closed-loop preimages. Most of $\mathbb{R}^3$ is occupied by the preimage of the point in $\mathbb{S}^2$ corresponding to $\mathbf{m}_0$ (figure 22) [24], except for the interior of a torus-embedded region, within which all other preimages are smoothly packed. Preimages with the same polar angles but different azimuthal angles tile into tori; then tori corresponding to different polar angles sequentially nest within each other's interior, all imbedded within the biggest torus that has all the preimages in its interior, except for the $\mathbf{m}_0$-preimage that is in its exterior (figure 22) [24]. Stable hopfions in physical systems ranging from elementary particles to cosmology have been predicted by Faddeev, Niemi, Sutcliffe and many others [7, 22, 42], as well as demonstrated experimentally as stable solitons in colloidal ferromagnets and LCs [24, 190, 191]. Nonlinear optical 3D imaging was utilized to unambiguously identify topological solitons, revealing an experimental equivalent of the mathematical Hopf map (figures 21(c) and (d)) and relating experimental and theoretical closed-loop preimages of distinct $\mathbb{S}^2$ points [24]. Agreement of experimental and simulated real-space cross-sectional nonlinear optical images of hopfions and preimages of different points of the order parameter space (figures 21(c) and (d)) confirms the hopfion identity. While nonlinear optical imaging of $\mathbf{m}(\mathbf{r})$ cannot discriminate $\mathbf{m}(\mathbf{r})$ and $-\mathbf{m}(\mathbf{r})$ because of being based on orientations of transition dipole moments of the organic LC molecular host [24], this ambiguity related to telling apart the preimages of diametrically opposite points is lifted by probing the response to applied magnetic fields $\mathbf{B}$ in directions parallel or antiparallel to $\mathbf{m}_0$ (figure 21(e)). $\mathbf{B}$ applied antiparallel to $\mathbf{m}_0$ forces the soliton to grow, with the outer diameter increasing and the inner region shrinking [24], with the opposite response for $\mathbf{B}\|\mathbf{m}_0$ (figure 21(e)). Since the coupling of $\mathbf{B}$ and $\mathbf{m}$ is linear, described by a corresponding free-energy term, this eliminates the $\mathbf{m}$ versus $-\mathbf{m}$ ambiguity, so that the entire structure can be smoothly vectorized [24].

The detailed structure of axisymmetric $\mathbf{m}(\mathbf{r})$ within the static Hopf soliton is depicted in figures 21(f) and (g). It minimizes the Frank–Oseen free energy of a chiral ferromagnetic LC at no applied external fields:

$$F_{\mathrm{CFLCC}} = \int \mathrm{d}\mathbf{r} \left\{ \frac{K_{11}}{2}(\nabla \cdot \mathbf{m})^2 + \frac{K_{22}}{2}[\mathbf{m} \cdot (\nabla \times \mathbf{m})]^2 + \frac{K_{33}}{2}[m \times (\nabla \times \mathbf{m})]^2 + q_0 K_{22} \mathbf{m} \cdot (\nabla \times \mathbf{m}) \right\} \tag{1}$$

For splay, twist and bend Frank elastic constants equal, $K = K_{11} = K_{22} = K_{33}$, within the one-constant approximation [12], the ferromagnetic LC's free-energy functional reduces to a micromagnetic Hamiltonian for non-centrosymmetric chiral magnets for $A = K/2$ and $D = Kq_0$ [24, 165, 175]:

$$F = \int \mathrm{d}\mathbf{r} \left[A(\nabla \mathbf{m})^2 + D\mathbf{m} \cdot (\nabla \times \mathbf{m}) \right] \tag{2}$$

where the coefficients A and D for magnetic solids describe the effective exchange energy and the Dzyaloshinskii–Moriya coupling. Numerical minimization of both free-energy functionals yields minima corresponding to Hopf solitons with linked preimages (figures 21–23) [24, 42, 191]. This linking cannot change without a breakdown of the $\mathbf{m}(\mathbf{r})$ continuum, e.g. through melting or generation of singular defects, further helping to stabilize such topological solitons. Hopfions with different Hopf indices can co-exist in monodomain samples because they can all correspond to local or global free-energy minima. Both the ferromagnetic LC and a Hopf link of any two preimages with consistently defined circulations of a hopfion are chiral, so that taking a mirror image negates the linking number and Q while also transforming a left-handed ferromagnetic LC into its right-handed counterpart [24, 191]. Many-body elastic interactions between individual hopfions in the presence of a lateral confinement lead to hexagonal arrays imbedded into $\mathbf{m}_0$ [24], consistent with their particle-like nature. Self-assembly of hopfions may result in 2D and 3D solitonic condensed matter phases, analogs of the so-called 'A-phase' of 2D skyrmions [175–181], which calls for a detailed study of phase diagrams.

Minimization of free energy given by equation (2) predicts the existence of 3D topological solitons in solid non-centrosymmetric ferromagnets [42] with experimental values of A and D. Like in the chiral term in free energy for ferromagnetic colloidal systems [24], the Dzyaloshinskii–Moriya term in equation (2) helps in overcoming the stability constraints defined by the Derick theorem [193]. Solid-state magnetic hopfions have been predicted to exist in nanodiscs, thin films and nanochannels of non-centrosymmetric magnetic solids with perpendicular surface anisotropy [42] (figures 23(a) and

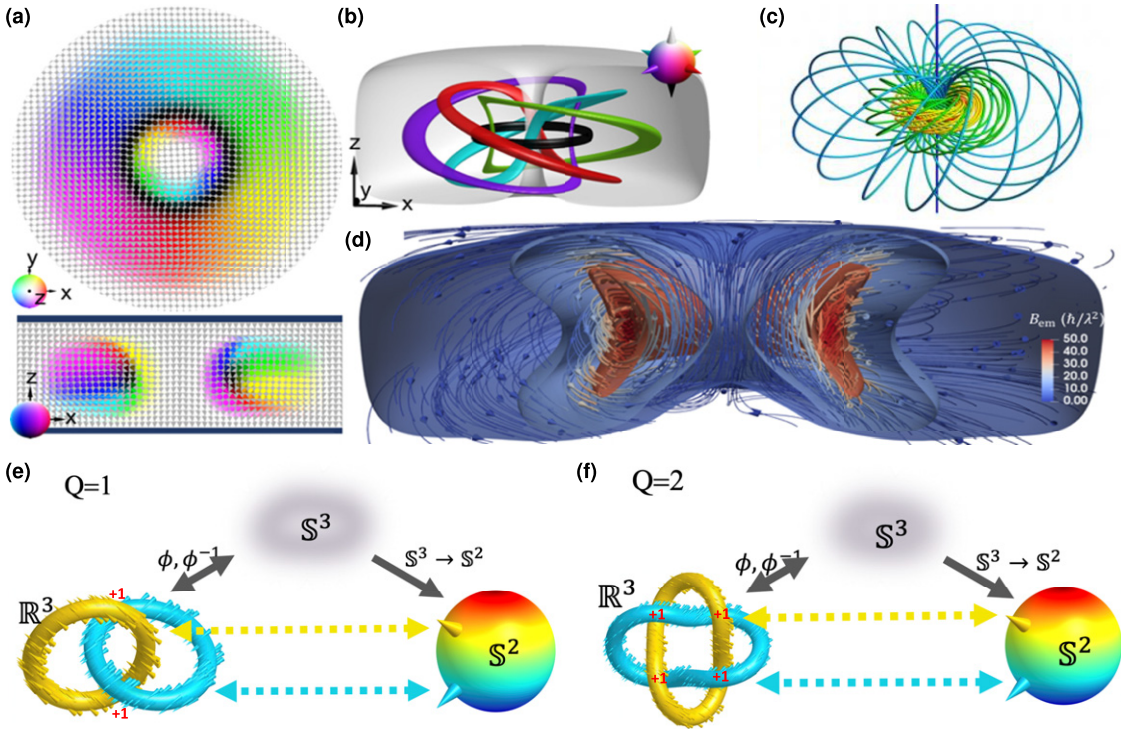

Figure 23. Hopfions in solid-state non-centrosymmetric magnets. (a) Cross-sections of the magnetization field within a hopfion in the plane perpendicular to $\mathbf{m}_0$ (upper) and that containing $\mathbf{m}_0$ (lower) in a magnetic solid material. Magnetization fields are shown with cones colored according to $\mathbb{S}^2$ (lower-left insets). In the x–z cross-section, black stripes at the top and bottom indicate interfaces with boundary conditions achieved using perpendicular surface anisotropy and thin-film confinement. (b) Preimages of $\mathbb{S}^2$ points indicated as cones in the inset. The linking number of preimage pairs is consistent with the Hopf index $Q = 1$. (c) Geometry and topology of the Hopf fibration. (d) Visualization of the emergent magnetic field $\mathbf{B}_{\text{em}}$ by the isosurfaces of constant magnitude and streamlines with cones indicating directions. (a)–(d) Reproduced with permission from [42]. (e) and (f) For hopfions, preimages of $\mathbb{S}^2$ in $\mathbb{R}^3$ (and $\mathbb{S}^3$) form Hopf (e) and Solomon links (f) with linking numbers matching their $Q = 1$ (e) and $Q = 2$ (f) Hopf indices. Since direct (ϕ) and inverse (ϕ^{-1}) stereographic projections relate configurations on $\mathbb{S}^3$ and in $\mathbb{R}^3$ when embedded within $\mathbf{n}_0$ and $\mathbf{m}_0$, these solitons are characterized by $\mathbb{S}^3 \to \mathbb{S}^2$ maps, $\pi_3(\mathbb{S}^2) = \mathbb{Z}$ homotopy group and $Q \in \mathbb{Z}$; crossing signs in (e) and (f) are marked in red. (e) and (f) Reproduced with permission from [191].

(b)), featuring closed-loop preimages of all $\mathbb{S}^2$ points, with each pair linked Q times. Due to the field topology, the emergent magnetic field $(\boldsymbol{B}_{\text{em}}) \equiv \hbar\varepsilon^{ijk}\boldsymbol{m}(\partial_j\boldsymbol{m} \times \partial_k\boldsymbol{m})/2$ of a solid-state elementary hopfion spirals around its symmetry axis with a unit flux quantum (figures 23(c) and (d)) [42]. Streamlines of $\boldsymbol{B}_{\text{em}}$, describing the interaction between conduction electrons and the spin texture, also resemble Hopf fibration [192]. This behavior of $\boldsymbol{B}_{\text{em}}$ mimics the topology of preimages for hopfions (figures 23(e) and (f)). It will be interesting to explore in future whether $\boldsymbol{B}_{\text{em}}$ in solid-state systems can also mimic the behavior of preimages in high-Hopf-index hopfions, like those with $Q = 2$ Solomon link topology (figure 23(f)). The capability of encoding 1, 0, 2, −1 and other states in the topological charges of 3D Hopf solitons in a chiral magnet can lead to data storage and other spintronics applications, with some of them already pursued in modeling [42, 43]. While the stability of 3D solitons like hopfions has always been challenged by the Derrick theorem [43, 190–193], their experimental observation in chiral LCs and colloidal ferromagnets [24, 190] offered insights that led to the predictions of such hopfions in magnetic solid-state materials [42, 43, 191], demonstrating the power of using soft matter as model systems. The insight in this particular case is that the energetic stability of Hopf solitons is enhanced by the medium's chirality, and that such topological objects can be hosted as stable or metastable structures in systems with Hamiltonians like the ones given by equations (1) and (2) of chiral ferromagnetic colloidal LCs and solid-state magnets.

5.4. Hopfions in nonpolar LCs

Hopf solitons in chiral nematics differ from those in vector fields of chiral magnets discussed above in that they are realized in the nonpolar field with the $\mathbb{S}^2/\mathbb{Z}_2$ order parameter space [190]. Shown in figure 24 are elementary LC hopfions with opposite signs of Hopf indices. Rod-like molecules and $\mathbf{n}(\mathbf{r})$ twist by 2π in all radial directions from the central axis to the $\mathbf{n}_0$ periphery within both solitons (figure 24) [190]. By vectorizing $\mathbf{n}(\mathbf{r})$ of the two solitons (figure 24), so that $\mathbf{n}_0$ points in the same direction for both of them and so that circulations of preimages are defined continuously, one finds $Q = 1$ for the soliton shown in figures 24(a)–(e) and $Q = -1$ for that in figures 24(f)–(j). For both hopfions, all $\mathbb{S}^2/\mathbb{Z}_2$ points for the nonpolar director have individual preimages in the form of two linked loops (figure 24) [190]. This is expected since the manifold $\mathbb{S}^2/\mathbb{Z}_2$ is effectively half of $\mathbb{S}^2$, and the smoothly vectorized version of the hopfion has all preimages of $\mathbb{S}^2$ in the form of individualized closed-loop regions. While the handedness of the $\mathbf{n}(\mathbf{r})$ twist is determined by LC chirality and is the

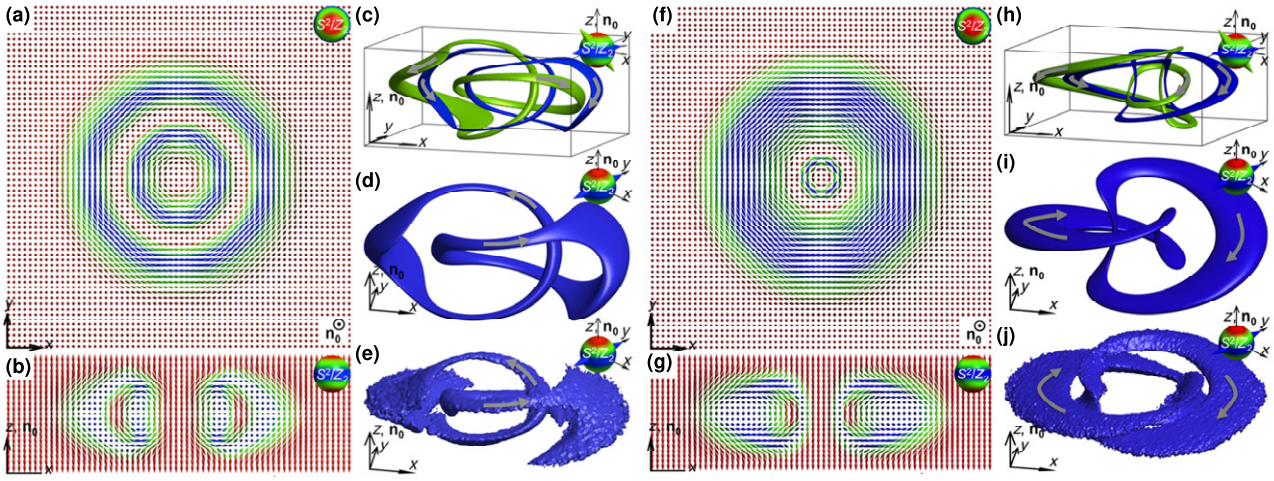

Figure 24. Nematic LC hopfions. (a)–(e) A hopfion with $Q = 1$ determined using the vectorized $\mathbf{n}(\mathbf{r})$. (a) and (b) Computer-simulated (a) in-plane and (b) vertical cross-sections of the axisymmetric $\mathbf{n}(\mathbf{r})$ of the hopfion depicted using double cones and the color scheme that establishes correspondence between director orientations and the points on $\mathbb{S}^2/\mathbb{Z}_2$ (top-right insets). (c) Computer-simulated preimages of the hopfion for two sets of the diametrically opposite points on $\mathbb{S}^2/\mathbb{Z}_2$ marked by double cones in the top-right inset. (d) and (e) A comparison of representative (d) computer-simulated and (e) experimental preimages of the hopfion for two diametrically opposite points on $\mathbb{S}^2/\mathbb{Z}_2$ (top-right insets). Gray arrows in (c-e) show the consistently determined circulation directions of the preimages. (f)–(j) A hopfion with $Q = -1$, with characterizations and visualizations performed analogously to those shown in (a)–(e). Reproduced with permission from [190].

same for the two solitons within the same host material, the localized director configurations yield Hopf links of preimages of opposite handedness (figures 24(c)–(e) and (h)–(j)), both of which, interestingly, correspond to energy minima (though with somewhat different energies) [190]. For both hopfions, experimental preimages closely match their theoretical counterparts (figures 24(d), (e), (i) and (j)). The Q values stay the same upon inverting the vectorization direction $\mathbf{n}(\mathbf{r}) \to -\mathbf{n}(\mathbf{r})$, different from the case of hedgehog charges of point defects in nonpolar LCs that change signs with $\mathbf{n}(\mathbf{r}) \to -\mathbf{n}(\mathbf{r})$ [34]. However, taking a mirror image negates the linking numbers of all preimage links and Q values, again different from hedgehog charges of point defects that would stay unchanged [34]. These properties of LC hopfions also apply to their topological counterparts in chiral magnets discussed above [24, 191].

Interesting soliton configurations arise when increasing the amount of the radial $\mathbf{n}(\mathbf{r})$ twist embedded within $\mathbf{n}_0$. For example, $\mathbf{n}(\mathbf{r})$ twists by 4π in all radial directions from the two solitons' central axes to their periphery in figures 25(a), (b), (h) and (i), yielding two-closed-loop preimages of $\mathbb{S}^2$ points for vectorized $\mathbf{n}(\mathbf{r})$, with preimages of each point on $\mathbb{S}^2/\mathbb{Z}_2$ of nonpolar $\mathbf{n}(\mathbf{r})$ comprising four individual closed loops (figures 25(d)–(g) and (k)–(n)). Preimages for the same polar angle θ of vectorized $\mathbf{n}(\mathbf{r})$ and with different azimuthal $\mathbf{n}(\mathbf{r})$ orientations tile into tori (figures 25(f) and (m)). There are always two such tori for a given θ (figures 25(f) and (m)), which is different from the case of elementary hopfions (figure 24). For all $\mathbb{S}^2$ points of vectorized $\mathbf{n}(\mathbf{r})$ of the soliton shown in figures 25(a)–(g) (figures 25(h)–(n)), the individual preimages are formed by two separate unlinked closed loops while preimages of two separate $\mathbb{S}^2$ points form two Hopf links with the linking number $+1$ (-1) for each of them, as seen in figures 25(d) and (e) (figures 25(k) and (l)). Tori formed by preimages of constant θ remain separate until merging with the far-field background when $\mathbf{n}(\mathbf{r})$ becomes parallel $\mathbf{n}_0$ (figures 25(f), (g), (m) and (n)). The behavior of the individual $\mathbb{S}^2/\mathbb{Z}_2$ preimages of nonpolar $\mathbf{n}(\mathbf{r})$ is reminiscent to that of pairs of $\mathbb{S}^2$ preimages for vectorized $\mathbf{n}(\mathbf{r})$ (figures 25(d)–(g) and (k)–(n)). The preimages of $\mathbb{S}^2$ points in the vicinity of the north pole are two separate tori that characterize $\mathbf{n}(\mathbf{r})$ smoothly transforming to $\mathbf{n}_0$ in their exterior (figures 25(g) and (n)). Thus, one can interpret the two solitonic structures shown in figure 25 as $Q = 2$ and $Q = -2$ hopfions, respectively, each formed by coaxial arrangements of two separate like-charged hopfions of Hopf index $Q = 1$ (figures 25(a)–(g)) and $Q = -1$ (figures 25(h)–(n)). Hopfions that could be thought of as comprising elementary hopfions of opposite signs of Q have been experimentally observed [190], including those with a $Q = 1$ hopfion in the interior and $Q = -1$ hopfion in the exterior of the coaxial hybrid solitons and vice versa [190]. Coaxially arranged hopfions of opposite signs can annihilate and transform into a uniform state, whereas that of like-charged hopfions gives high-index solitons with Q being the sum of Q values of individual structures [190, 191]. While each hopfion is uniquely characterized by Q and the corresponding linking number of preimages, there are different ways to obtain the same linking numbers within a soliton. For example, a hopfion with $Q = 2$ could have two Hopf links for each pair of preimages or a single Solomon link [191]. Analogously, a localized solitonic structure with $Q = 0$ could be comprised of coaxially arranged $Q = -1$ and $Q = 1$ hopfions or simply have no linked closed-loop preimages (even if still featuring closed-loop preimages) [191]. Such variations of interlinking are often found within the same 3D solitons, where, as an example, pairs of some preimages can form a Solomon link, but others form two Hopf links, in each case with the same linking number [190, 191]. Moreover, even individual preimages can have different geometries within different parts of order parameter space for the same soliton, as long as the linking number, which is the topological invariant defining Q,

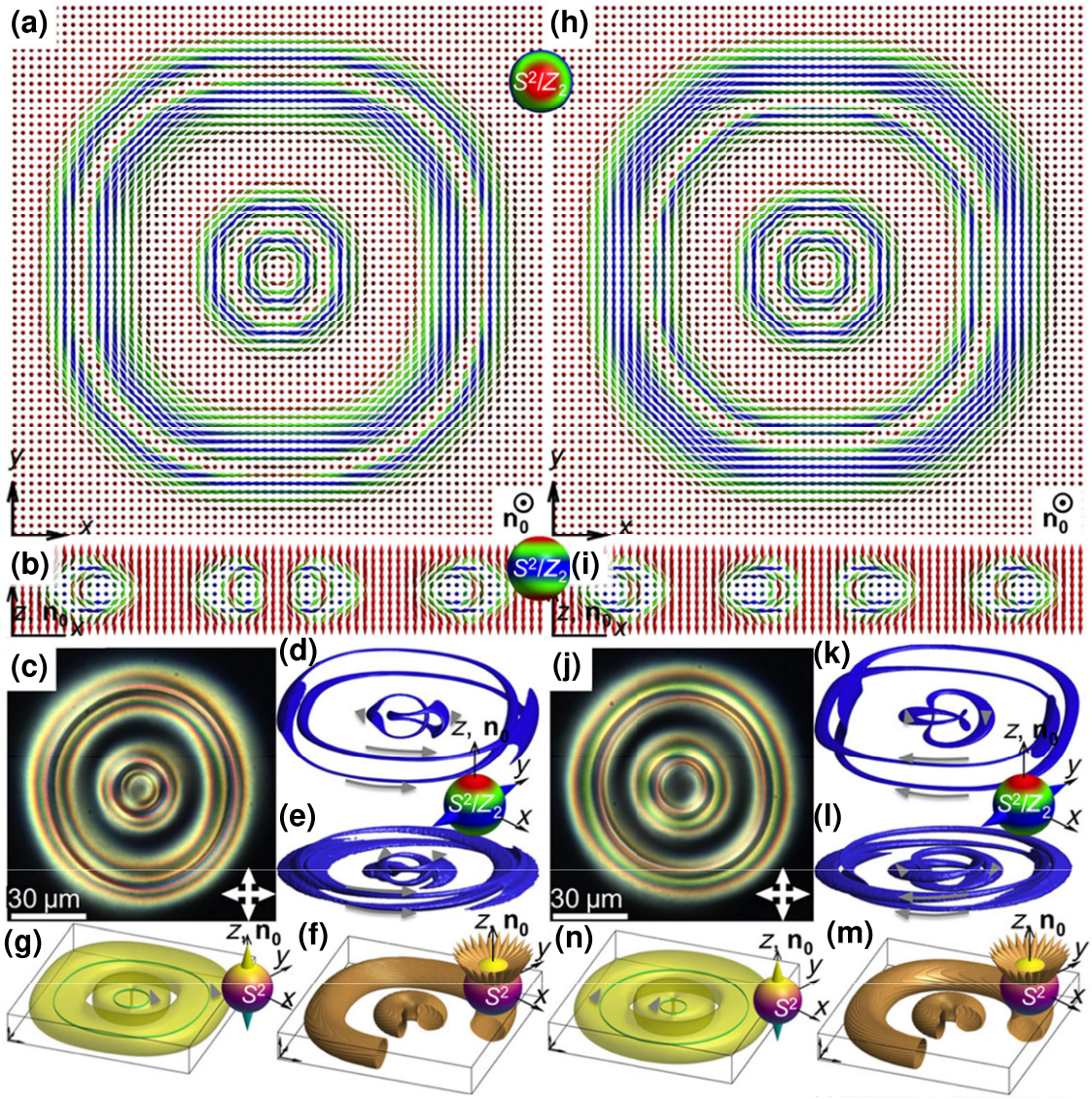

Figure 25. The 3D solitons formed by coaxial arrangement of two elementary hopfions. (a)–(g) A $Q = 2$ topological soliton comprising two coaxially arranged hopfions, each with a Hopf index $Q = 1$ (a) and (b). Computer-simulated (a) in-plane orthogonal to $\mathbf{n}_0$ and (b) vertical containing $\mathbf{n}_0$ cross-sections of the axisymmetric $\mathbf{n}(\mathbf{r})$ of a $Q = 2$ soliton depicted using colored double cones; the color scheme establishes the correspondence between $\mathbf{n}(\mathbf{r})$-orientations and $\mathbb{S}^2/\mathbb{Z}_2$ (insets). (c) A polarizing optical micrograph of such a soliton in a chiral nematic LC. White double arrows show orientations of crossed polarizers. (d) Computer-simulated and (e) experimental preimages of the soliton for the diametrically opposite points on $\mathbb{S}^2/\mathbb{Z}_2$ marked by double cones in the inset. (f) For a constant polar angle (inset), the closed-loop preimages of individual points on $\mathbb{S}^2$ tile into two tori sharing the same vertical axis along $\mathbf{n}_0$. (g) Preimages of the north and south poles of $\mathbb{S}^2$ for the vectorized $\mathbf{n}(\mathbf{r})$. (h)–(n) A $Q = -2$ soliton just like that shown in (a)–(g), but comprising two coaxial hopfions with $Q = -1$ each, with figure parts mirroring those in (a)–(g). Reproduced with permission from [190].

is conserved for all pairs of preimages [191]. The large number of possibilities to realize solitonic structures of given Q (in both experiments and modeling) contributes to the diversity of Hopf solitons [190], which is revealed by simplified topology and graph presentations (figure 26). In these graphs, the closed-loop preimage components are filled circles colored according to the positions of corresponding points on the ground-state manifold, and the individual links are indicated by black edges connecting these circles (figure 26) [190]. Moreover, figures 21–26 illustrate that not only elementary hopfions but entire zoos of $\pi_3(\mathbb{S}^2) = \mathbb{Z}$ and $\pi_3(\mathbb{S}^2/\mathbb{Z}_2) = \mathbb{Z}$ solitons exist in soft matter. The insights into the diversity of structural embodiments of topological Hopf solitons experimentally revealed by LC and colloidal systems are useful for theoretical modeling and experimental discovery of such topological objects in other branches of physics.

5.5. Hybrid torons and twistions

In addition to the elementary torons with π-twist of $\mathbf{n}(\mathbf{r})$ from their central axes to the $\mathbf{n}_0$-periphery in all radial directions (figure 19), torons with larger amounts of such twist exist. For example, torons shown in figures 27(a) and (b) contain 3π twist of $\mathbf{n}(\mathbf{r})$ in all radial directions [190]. Additionally, torons with 5π and larger amounts of twist within axisymmetric toron

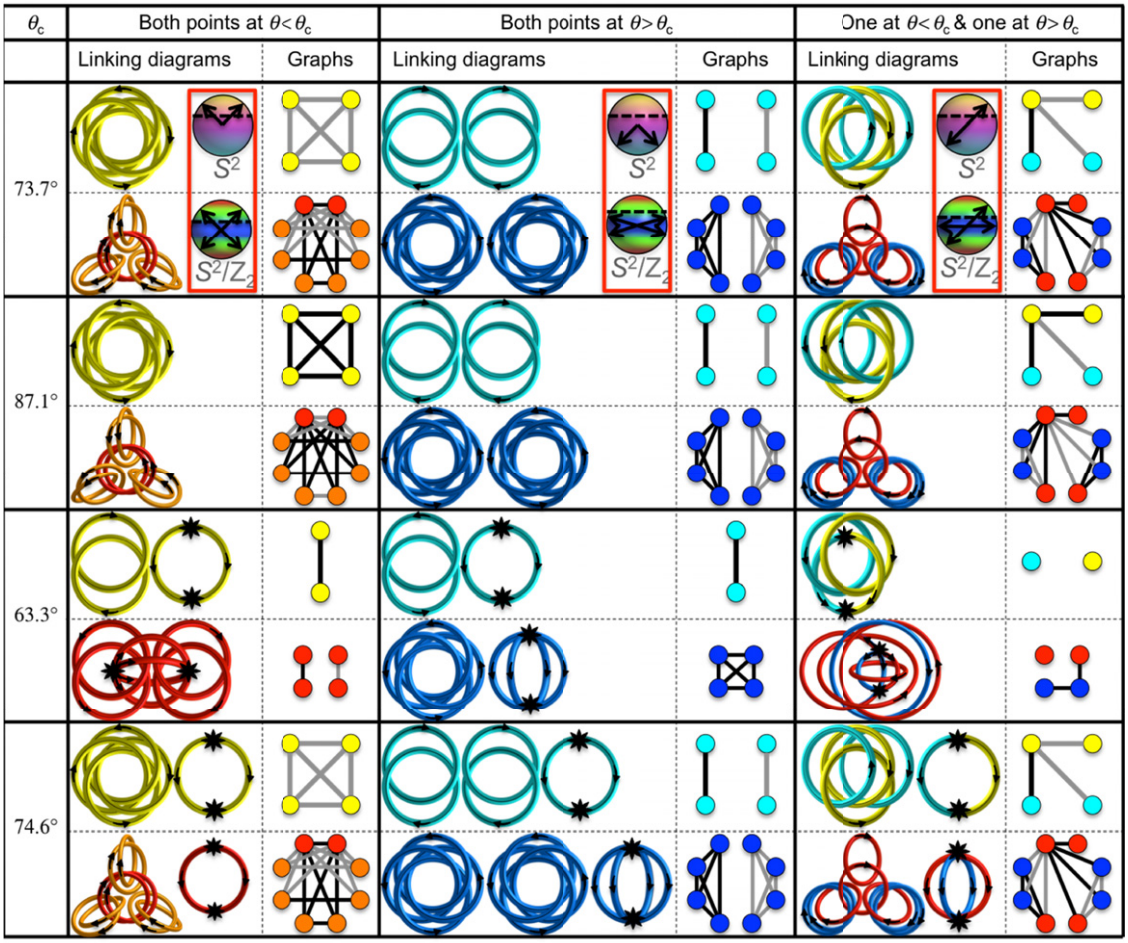

Figure 26. Linking diagrams and graphs of complex 3D topological solitons. The analysis reveals the linking of preimages of two different points on $\mathbb{S}^2$ and $\mathbb{S}^2/\mathbb{Z}_2$ on the basis of both nonpolar and vectorized $\mathbf{n}(\mathbf{r})$. The insets in the red boxes at the top of the columns 'linking diagrams' depict the order parameter spaces of vectorized (top) and nonpolar (bottom) $\mathbf{n}(\mathbf{r})$, with arrows or double arrows indicating the points for which the preimage linking is analyzed. The dashed lines on the $\mathbb{S}^2$ and $\mathbb{S}^2/\mathbb{Z}_2$ separate regions of $\mathbb{S}^2$ and $\mathbb{S}^2/\mathbb{Z}_2$ with $\theta < \theta_c$ (top parts) and $\theta > \theta_c$ (bottom parts), where θ_c is the critical polar angle defining the boundary lines between different subspaces of the order parameter space; θ_c lines separate regions with different individual preimages [190]. Locations of points corresponding to preimages, shown using single and double arrows on $\mathbb{S}^2$ and $\mathbb{S}^2/\mathbb{Z}_2$, are the same for all solitons within the same column. In the graphs, individual links are indicated by black or gray lines connecting the corresponding colored filled circles that represent closed-loop preimages (black lines indicate positive signs of linking of preimages, whereas gray lines correspond to the negative ones). The colors of the filled circles are indicative of the points on $\mathbb{S}^2$ (for schematics shown above the horizontal dashed lines of the table) or $\mathbb{S}^2/\mathbb{Z}_2$ (for schematics shown below the horizontal dashed lines of the table); for $\mathbf{n}(\mathbf{r})$ at $\theta < \theta_c$, two out of eight filled circles of the graphs are shown as red and the rest as orange to distinguish them on the basis of the number of times the corresponding preimages are linked. The mutually linked preimage rings in the simplified topology presentations are also shown in colors corresponding to their locations on $\mathbb{S}^2$ and $\mathbb{S}^2/\mathbb{Z}_2$ and have arrows denoting circulation consistent with the far-field preimage. Point defects of torons within the topological skeletons are shown using black stars. Both the topological skeleton and graph representations of the preimage structures are constructed for the same configurations and are provided next to each other for the vectorized $\mathbf{n}(\mathbf{r})$. Reproduced with permission from [190].

structures were found in recent experiments [190]. Preimages of distinct points on the $\mathbb{S}^2/\mathbb{Z}_2$ or $\mathbb{S}^2$ for such toron–hopfion hybrid structures are either closed loops or bands starting and terminating on the hyperbolic point defects (figures 27(c)–(e)). Such torons can be thought of as a separate elementary hopfion and an elementary toron arranged coaxially so that their symmetry axes coincide. The multicomponent preimages, comprised of closed loops and half-loop bands that terminate on the point singularities, reveal the diversity of topological and structural compositions of such torons (figure 26). Solitonic and singular topological structures also co-exist within hybrid structures called 'twistions', localized configurations that embed spatially localized twisted regions into a uniform $\mathbf{n}_0$ background but lack axial symmetry and (unlike torons) contain more than two point defects [194] (figure 28).Within a structure shown in figure 28, $\mathbf{n}(\mathbf{r})$ twists from its interior to periphery by $\sim\pi$, though twistions with larger amounts of such twist exist too, analogously to what was discussed above for torons [190, 191, 194]. The twistion in figures 28(a)–(c) contains a stretched loop of π-twist of $\mathbf{n}(\mathbf{r})$ and four self-compensating hyperbolic point defects, as revealed with the help of cross-sections. Its topology can again be analyzed using preimages, which are bands spanning between the four point singularities (figures 28(d) and (e)). This example shows

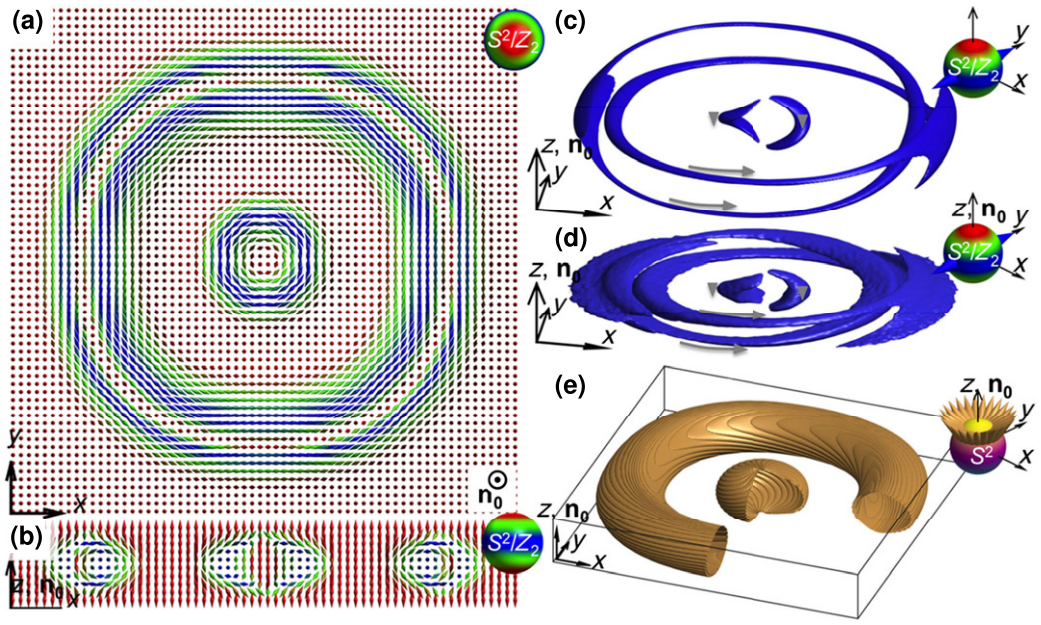

Figure 27. A complex toron structure formed by coaxial arrangement of an elementary toron and hopfion. (a) and (b) Computer-simulated (a) in-plane orthogonal to $\mathbf{n}_0$ and (b) vertical containing $\mathbf{n}_0$ cross-sections of axisymmetric $\mathbf{n}(\mathbf{r})$ structure depicted using colored double cones; the color scheme establishes the correspondence between director orientations and the points on $\mathbb{S}^2/\mathbb{Z}_2$ (insets). (c) Computer-simulated and (d) experimental preimages for the diametrically opposite points on $\mathbb{S}^2/\mathbb{Z}_2$ marked by double cones in the insets. Gray arrows indicate the consistently determined circulations of preimages. (e) For each polar angle, closed-loop preimages of individual points on $\mathbb{S}^2$ tile into a torus and a sphere, with the sphere having two small holes at poles corresponding to the two point defects. Reproduced with permission from [190].

that localized skyrmion-, toron- and hopfion-like field configurations in confined chiral nematic LCs are not restricted to hosting none (as in skyrmions and hopfions) or only pairs (as in the torons) of self-compensating singular defects. Such self-compensation can occur in a number of other more complex ways, e.g. with four hyperbolic point defects shown in addition to various solitonic components with band-like or closed-loop preimages (figure 28). Similar multi-point-defect configurations with solitonic $\mathbf{n}(\mathbf{r})$ in-between have also been reported for cholesteric LC drops [147].

5.6. *Topological inter-transformations of solitons*

LCs are known for their facile responses to external fields, though this switching typically involves topologically trivial structures [12]. Switching of solitonic structures in chiral nematic and ferromagnetic LCs has been explored too, demonstrating both topology-preserving morphing and topological transformations (involving changes of topological invariants) driven by electric and magnetic fields [191]. The far-field director $\mathbf{n}_0$ and magnetization $\mathbf{m}_0$ were fixed to assure compactification of $\mathbb{R}^3$ to $\mathbb{S}^3$ for the 3D solitonic structures during switching. Since ferromagnetic LC is polar, $\mathbf{m}(\mathbf{r})$ responds differently to external magnetic fields $\mathbf{H}$ and $-\mathbf{H}$, making magnetically driven transformations of solitons especially rich (figure 29) [191]. As an example, an axisymmetric soliton with complex linking of preimages but net $Q = 0$ at zero field is shown in figures 29(a) and (b) [191]. $\mathbf{H}$ applied parallel or antiparallel to $\mathbf{m}_0$ drives this soliton's $\mathbf{m}(\mathbf{r})$ through a series of continuous and discontinuous deformations (figures 29(c) and (d)), where the distinct types of encountered preimage linking are shown schematically in the insets [191]. A structural diagram in the coordinates of thickness-to-pitch ratio d/p and applied magnetic field (figure 29(d)) encompasses a wealth of knotted configurations, where the Hopf index Q stays unchanged within some parameter ranges, but changes discontinuously at the boundaries of the diagram between the topologically distinct states with different Q. Within a broad range of parameters, solitons morph without changing topology (figure 29(d)) [191]. The $\mathbb{S}^2$ ground-state manifold splits into two subspaces (figure 29(b)) separated by a boundary at a critical polar angle θ_c dependent on $\mathbf{H}$ (figure 29(c)). Different preimages of points on $\mathbb{S}^2$ not only coexist within the same knot soliton, smoothly embedding within a localized volume in $\mathbb{R}^3$, but are also magnetically inter-transformed while remaining nonsingular, as long as the linking number of all preimage pairs for a given soliton stays conserved. Outside of the central parts of the diagram, with changing d/p and $\mathbf{H}$, $Q = 0$ solitons with complex preimage linking discontinuously inter-transform into $Q = -1$ solitons, torons and other structures (figure 29(d)) [191]. Since both chiral LCs and colloidal ferromagnets are optically birefringent, different Hopf index values can be associated with optical signatures, such as polarization rotation, phase retardation, and light transmission when the sample is placed between polarizers, which could potentially expand the wealth of current electro-optic applications of these soft matter systems [12]. The illustrative example of a structural diagram (figure 29(d)) with the topological soliton switching is just one of many that have been

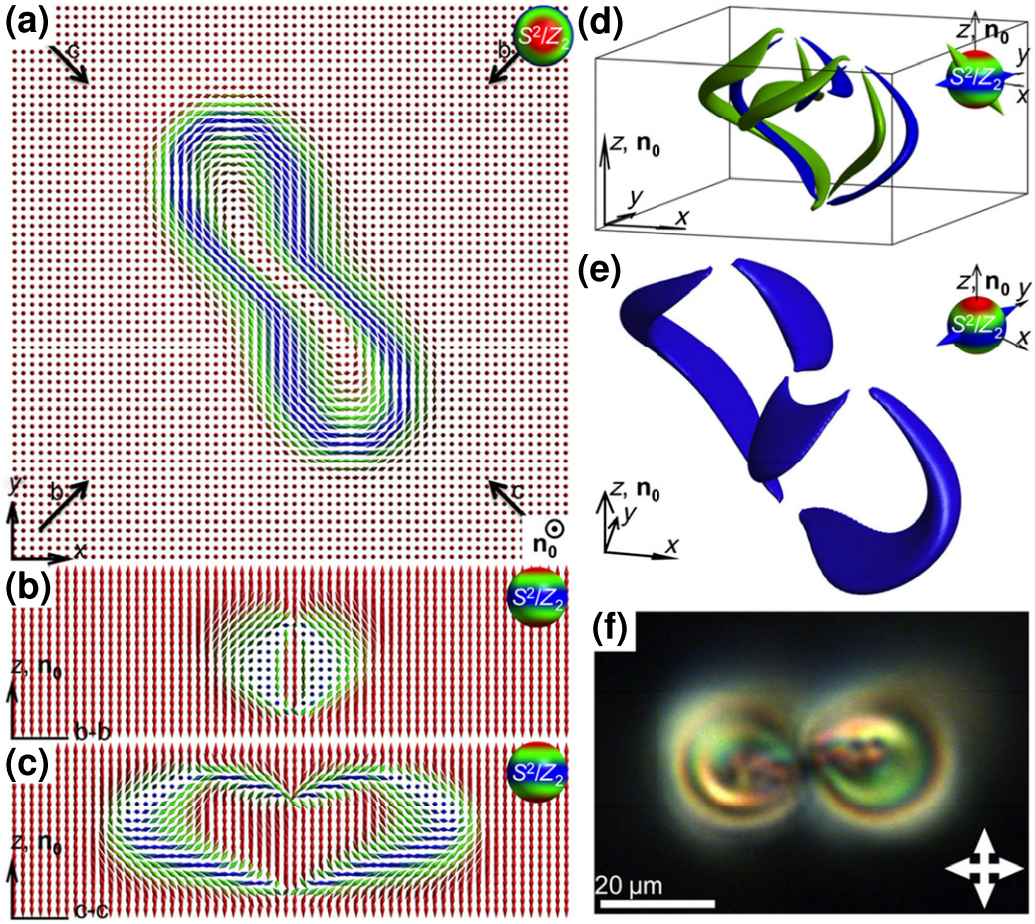

Figure 28. A twistion structure in a chiral nematic LC. (a)–(c) Computer-simulated (a) in-plane and (b) and (c) vertical cross-sections of the 3D $\mathbf{n}(\mathbf{r})$ of the twistion shown with double cones and the color scheme of director orientations according to $\mathbb{S}^2/\mathbb{Z}_2$ (insets). Locations of vertical cross-sections (b) and (c) are depicted in (a) using arrows. (d) Computer-simulated preimages of the twistion for points on $\mathbb{S}^2/\mathbb{Z}_2$ marked by double cones in the inset. (e) Computer-simulated preimages of the twistion for points on the 'equator' of $\mathbb{S}^2/\mathbb{Z}_2$ (top-right inset). (f) A polarizing optical micrograph of the twistion, with the white double arrows showing crossed polarizers. Reproduced with permission from [190].

reported, including examples of magnetic- and electric-field-controlled stability diagrams of solitons in LC, colloidal and solid-state magnetic systems [42, 44, 73, 191]. The similarity of findings in physical behavior (including switching) of solitons in soft and hard chiral condensed matter systems [42, 44, 73, 191] once again shows how LCs and colloids can be used as model systems in the studies of solitons in other fields.

5.7. Heliknotons and crystals of knots

Recently, stable micrometer-sized knots, called 'heliknotons', have been demonstrated in helical fields of chiral nematic LCs [73]. The helical fields comprise a triad of orthonormal fields (figure 30(a)): the molecular $\mathbf{n}(\mathbf{r})$ field, the helical axis $\boldsymbol{\chi}(\mathbf{r})$ field and $\boldsymbol{\tau}(\mathbf{r})\perp\mathbf{n}(\mathbf{r})\perp\boldsymbol{\chi}(\mathbf{r})$. Heliknotons are topological solitons with linked closed-loop $\mathbf{n}(\mathbf{r})$ preimages (figure 30(b)), while their $\boldsymbol{\chi}(\mathbf{r})$ and $\boldsymbol{\tau}(\mathbf{r})$ contain half-integer singular vortex lines forming knots (figure 30(c)). Therefore, the heliknoton is a hybrid embodiment of both preimage and vortex knots [73]. These knot solitons embed in a helical background and form spontaneously after the transition from the isotropic to LC phase when an electric field $\mathbf{E}$ is applied to a positive-dielectric-anisotropy chiral LC along the far-field helical axis $\boldsymbol{\chi}_0$. These structures comprise localized regions (depicted in gray in figures 30(b) and (c)) of perturbed helical fields and twist rate [73]. They display 3D particle-like properties, with anisotropic pair interaction potential varying from attractive to repulsive and from tens to thousands of k_BT [73], depending on the choice of LC, applied voltage U, sample thickness, equilibrium cholesteric pitch p_0, etc. The inter-heliknoton interactions arise from sharing long-range perturbations of the fields and minimizing the overall free energy for different relative positions [73]. These interactions enable a plethora of crystals, including 2D and 3D low-symmetry and open lattices (figure 30) [73], with tunable crystallographic symmetries and lattice parameters [73]. The 3D crystals of heliknotons emerge in samples of thickness $>4p_0$, when anisotropic interactions yield triclinic pedial lattices (figure 30(d)), whereas 2D crystals form in thinner samples. Besides the $Q = 1$ elementary heliknotons, $Q = 2$ and $Q = 3$ topological solitons were observed as well [73], with preimages in the material field $\mathbf{n}(\mathbf{r})$ linked twice and three times, respectively. For $Q = 2$ ($Q = 3$) heliknotons, singular vortex lines in $\boldsymbol{\chi}(\mathbf{r})$ and $\boldsymbol{\tau}(\mathbf{r})$ form closed 5_1 (7_1) knots co-located with the same knot of a meron in $\mathbf{n}(\mathbf{r})$.

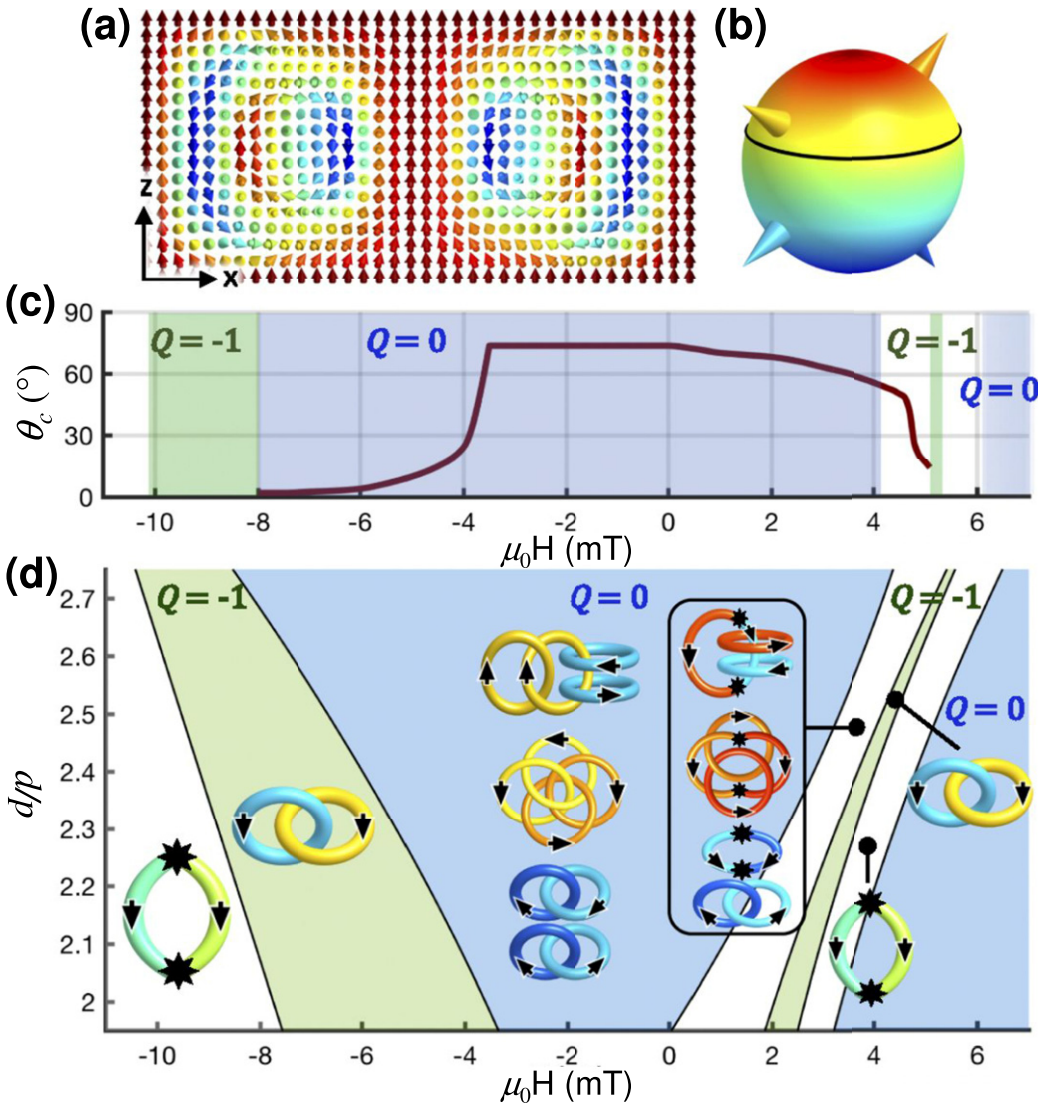

Figure 29. Control of localized topological structures by confinement and magnetic fields. (a) A computer-simulated cross-section of a stable axisymmetric $Q = 0$ soliton at $H = 0$ and thickness-over-pitch ratio $d/p = 2.7$. (b) Ground-state manifold $\mathbb{S}^2$ with four points (colored cones) corresponding to preimages of the same color schematically shown in the insets of (d). The black circle shows the θ_c-boundary line separating subspaces of $\mathbb{S}^2$ with different types of individual preimages, double unlinked loops for $\theta > \theta_c$ and a Hopf link of closed loops for $\theta < \theta_c$. (c) The critical angle θ_c and Q vs $\mu_0 H$ at $d/p = 2.7$. Q values are indicated atop of the colored regions of constant $Q = -1$ (green regions) and $Q = 0$ (blue regions). Singular point defects (depicted by stars in the insets) accompany the nonsingular solitons, forming elementary torons, within the diagram's white regions. Here, $\mu_0 H$ is defined as positive when $\mathbf{H}$ is parallel to $\mathbf{m}_0$ and negative when antiparallel to it. (d) A stability diagram of the solitons vs d/p and $\mu_0 H$. The insets depict the diverse topology of two-point preimages and their links for a family of hopfions with $Q = 0, -1$, and the two different types of torons that emerge in different regions of the diagram. Reproduced with permission from [191].

These and other heliknotons with even larger Q can be ground-state and metastable structures [73], behaving like particles. However, unlike the atomic, molecular and colloidal crystals, heliknoton crystals exhibit giant electrostriction and dramatic symmetry transformations under <1 V voltage changes. The closed-loop preimages of heloknotons are interlinked with the torus knot of vortices within the orthonormal fields [73], showing how remarkably beautiful and complex knotting of helical fields can be and calling for their search in other physical systems. For example, they can potentially emerge in solid-state non-centrosymmetric magnets and ferromagnetic LCs with helical fields and Hamiltonians similar to those of chiral LCs, as recently predicted theoretically [44].

6. Topological, solitonic and knotted active matter

6.1. Solitons as active particles in passive LCs

The examples showing the role of topology in the LC and colloidal soft matter behavior presented so far relate to equilibrium or metastability conditions, but an even richer interplay of topology, ordering and fluidity can emerge under the out-of-equilibrium conditions. Topological structures of defects

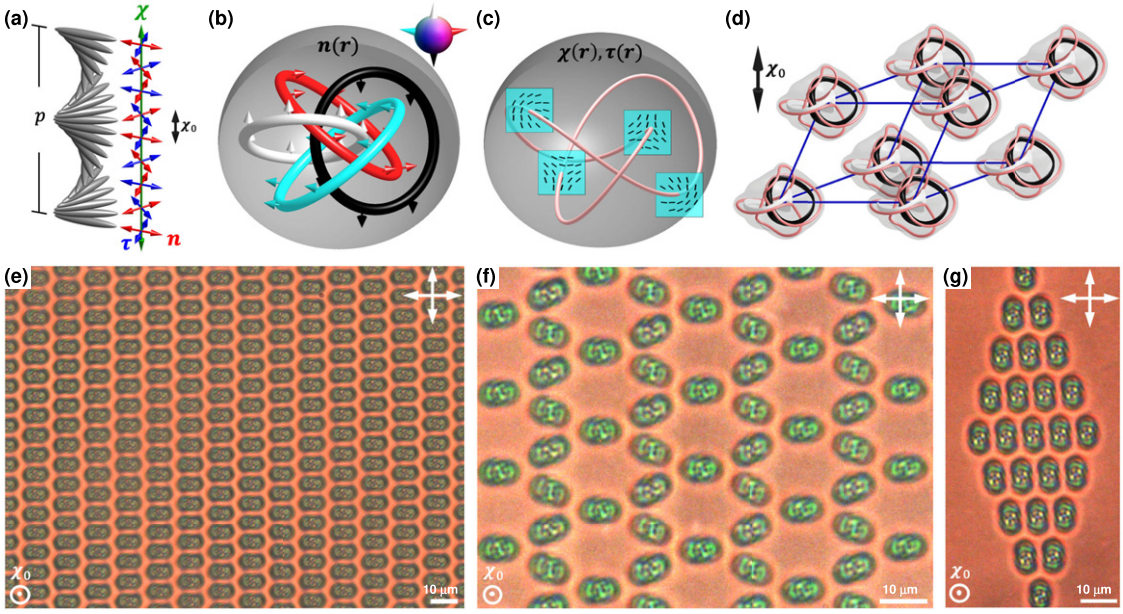

Figure 30. Topology and self-assembled crystals of heliknotons. (a) A helical field comprising a triad of orthonormal $\mathbf{n}(\mathbf{r})$, $\boldsymbol{\chi}(\mathbf{r})$ and $\boldsymbol{\tau}(\mathbf{r})$. (b) Preimages in $\mathbf{n}(\mathbf{r})$ of a heliknoton colored according to their orientations on $\mathbb{S}^2$ for vectorized $\mathbf{n}(\mathbf{r})$ (inset). (c) Knotted co-located half-integer vortex lines in $\boldsymbol{\chi}(\mathbf{r})$ and $\boldsymbol{\tau}(\mathbf{r})$. Gray isosurfaces in (b) and (c) show the localized regions of the distorted helical background. (d) The primitive cell of a 3D triclinic heliknoton crystal. Isosurfaces (gray) of heliknotons with a distorted helical background are co-located with both vortex knots (red) and preimages of antiparallel vertical orientations in $\mathbf{n}(\mathbf{r})$ (black and white). (e) and (g) Closed rhombic and (f) open heliknoton lattices obtained at $U = 1.9$ V and $U = 1.7$ V, respectively. Reproduced with permission from [73].

and solitons in LCs and nematic colloidal particles can be effectively 'activated' by supplying energy [80, 81, 194–198], just like this was done in the past with granular particles by shaking them [121, 199, 201], as an example. When supplied to LC and colloidal samples on macroscopic scales under well-controlled conditions, the external energy can be converted into motion on the individual soliton or singular defect basis; this can lead to various types of emergent active matter behavior, differing from classic effects like electrophoresis and dielectrophoresis, where external fields predictably predetermine motions of particles. As we shall see below while focusing on examples that involve skyrmions and torons, this enables synthetic active matter with rich varieties of collective motions of particle-like topological solitons and defects. While Skyrme solitons have been used historically as physical models of subatomic particles [7] and a variety of other topologically protected field configurations are commonly utilized as models of particles in different branches of physics, the significance of the active-matter-like behavior of topological solitons and defects in soft matter directly shows the utility of such topological models in active matter. We shall review how periodic pulses of an applied field lead to squirming motion of individual skyrmions and torons [80, 81], and then how this enables collective schooling and orderly motions of hundreds-to-millions of such topologically protected particle-like structures, with all motion directions selected spontaneously and arising from emergent behavior, uncorrelated with directions of the oscillating fields [195–198]. While in active nematics topological defects behave as active particles themselves [121, 199, 202], the active topological solitons that we will focus on here can be understood as active particle-like objects within an effectively passive medium, behaving as active topological excitations [80, 81, 195–198]. With fluid flows and complex hydrodynamics being an important part of the conventional active nematics and behavior of defects within them [121, 199, 202], the situation can be very different in the case of active topological solitons in passive nematics that rely mostly on the rotational director dynamics to move [80, 81]. Various backflow effects can be present (though typically not strong) during such dynamics [80, 81], but they are localized and not instrumental in defining motions that arise from non-reciprocity of rotations of $\mathbf{n}(\mathbf{r})$. The way topological solitons move when invoking this nonreciprocal rotational director dynamics could be paralleled with stadium waves (which move around the stadium without people actually leaving their seats) and concert-wave dance dynamics in response to music that can propagate with the speed of sound without carrying the dancers with them. The LC soliton motions also resemble the dynamics of topologically similar skyrmions in spin textures in solid-state magnets that can move through rotations of spins within solid films with up to kilometer-per-second speeds, being of interest for spintronics applications like in racetrack memory devices [160, 178–183]. However, the most fascinating feature of topological soliton behavior in soft matter is that their emergent collective motions can mimic that found in biological systems, like in schools of fish, though happening here without advection but rather through rotational dynamics in the order parameter field [197].

The facile response of LCs to periodically varying fields can cause local conversion of electric, magnetic, mechanical or other forms of energy into elastic energy stored within solitonic $\mathbf{n}(\mathbf{r})$ deformations and then into a soliton's translational

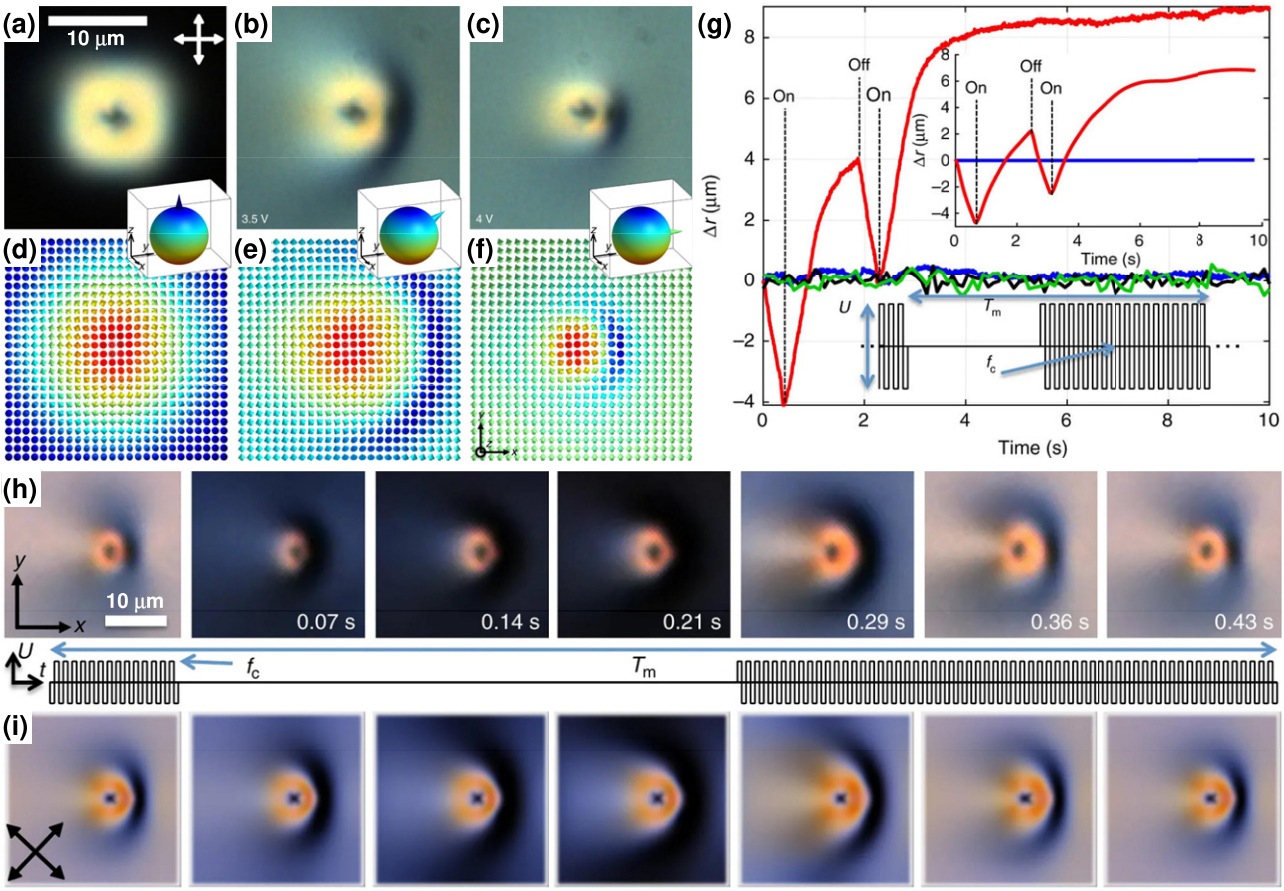

Figure 31. Translational skyrmion motions powered by an oscillating electric field. (a)–(f) Topology and electric switching (topology-preserving morphing) of 2D baby skyrmions: (a)–(c) polarizing optical micrographs of a 2D skyrmion at (a) no fields and (b) and (c) at voltages U indicated on the images. The electric field applied to negative-dielectric-anisotropy LC is perpendicular to the images. (d)–(f) Computer-simulated vectorized $\mathbf{n}(\mathbf{r})$ corresponding to (a)–(c), shown using arrows colored according to corresponding points on $\mathbb{S}^2$ (insets), with the far-field orientations depicted using cones. (g) Translation of a skyrmion in response to switching U on and off, with corresponding computer-simulated results shown in the top-right inset. The bottom inset illustrates the square waveform voltage driving with the carrier frequency $f_c = 1$ kHz and the modulation period T_m. Motion of the skyrmion is compared to that of a tracer nanoparticle at zero field (black solid line) and at $U = 4$ V (green solid line). (h) Experimental and (i) computer-simulated polarizing optical micrographs of a skyrmion when moving along a vector connecting the south- and north-pole preimages (positive x direction). The schematic in the inset between experimental and computer-simulated micrographs shows the timing of turning U on and off within the elapsed time equal to T_m, correlated with the micrographs in (h) and (i). Reproduced with permission from [80].

motion [80, 81, 195–198]. In the electric field case, dielectric coupling of $\mathbf{n}(\mathbf{r})$ with the electric field $\mathbf{E}$ morphs a soliton (figures 31(a)–(f)) and elastic free-energy costs associated with this deformation tend to drive relaxation of $\mathbf{n}(\mathbf{r})$ back to the initial state that minimizes energy at zero applied field. The nonreciprocal nature of $\mathbf{n}(\mathbf{r})$ rotation in response to switching voltage U on and off causes translation of solitons in lateral directions (figures 31(g)–(i)). Within each voltage modulation period T_m, the solitons are asymmetrically squeezed during the 'field-on' cycle and relax to minimize the elastic free energy during the 'field-off' cycle of T_m (figures 31(h) and (i)) [80]. This periodic nonreciprocal asymmetric morphing of the localized $\mathbf{n}(\mathbf{r})$ resembles squirming in biological systems, albeit LC solitons have no cell boundaries, density gradients or interfaces, so that the similarity is limited, mainly just in terms of the nonreciprocal character [81]. Like for active colloidal or granular particles [122, 123, 199–201], the energy conversion happens at the scale of individual particle-like solitons. Although the oscillating energy-supplying field is applied globally to the entire sample, its direction is not related to the emergent motion direction [80]. Depending on the applied voltage, this morphing of LC solitons by voltage pulses can take place below or slightly above the threshold of switching of the LC director in the background far away from the solitons [80, 196, 197], though in both cases the LC host medium features no or very minimal macroscopic flows, so that the LC stays passive (practically no advection) while the topological solitons start exhibiting active-particle-like emergent motions.

6.2. Out-of-equilibrium elastic interactions and schooling of skyrmions

Out-of-equilibrium elastic interactions between moving skyrmions emerge to reduce the free-energy costs of $\mathbf{n}(\mathbf{r})$ distortions around the topological solitons, albeit without the dynamic $\mathbf{n}(\mathbf{r})$ reaching equilibrium because of the periodic voltage modulation and soliton motions [197].

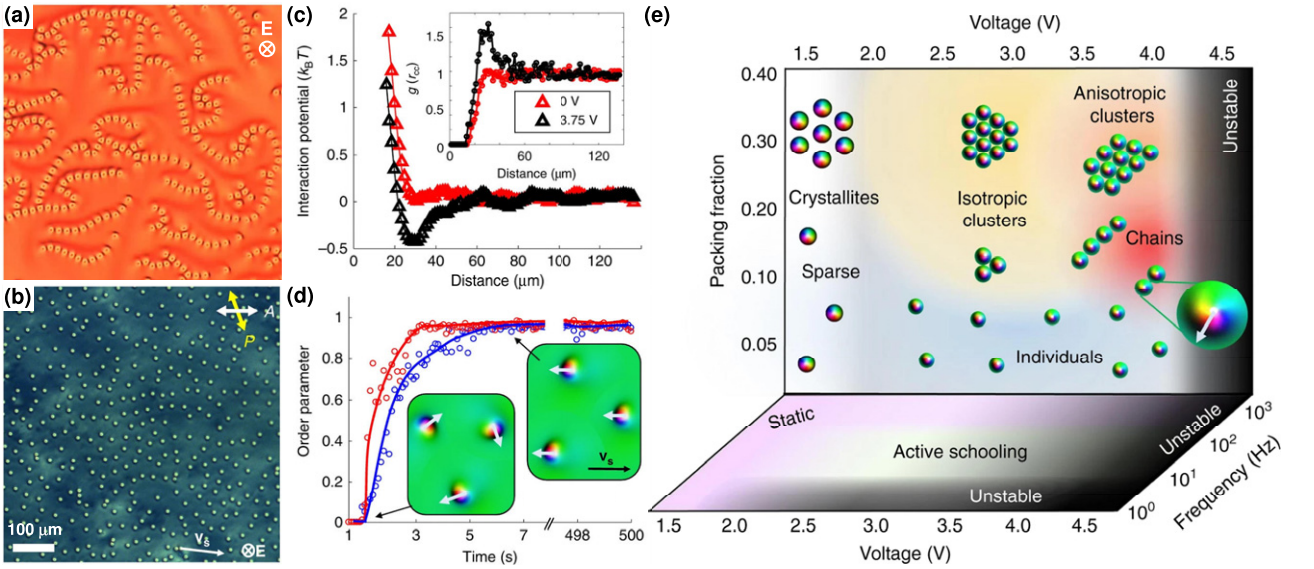

Figure 32. Schools of skyrmions. (a) and (b) Frames from videos of (a) moving chains and (b) a school of moving skyrmions without clustering. Directions of the electric field **E** are marked on (a) and (b). Polarizer (P) and analyzer (A) orientations and the skyrmion school motion velocity vector ($\mathbf{v}_s$) are marked in (b). (c) The interaction potential, extracted from the radial distribution function $g(r_{cc})$ shown in the inset, versus center-to-center distances r_{cc} for schooling skyrmions under conditions like those depicted in (b). (d) Evolution of velocity S_v (blue data points and eye-guiding curve) and polar S_p (red data points and eye-guiding curve) preimage vector order parameters with time. The insets schematically show the corresponding field configurations. (e) A diagram of static and dynamic skyrmion assemblies and schools versus packing fraction, frequency f and voltage U. The configurations shown in the insets are consistent across all f at which skyrmions are stable. Reproduced with permission from [197].

These interactions, at least partially, define the collective behavior of skyrmions while they move (figures 32(a) and (b)). The elastic interactions between skyrmions confined to a 2D plane have a dipolar nature (note also that the director configuration around a skyrmion in an applied field is of the dipolar type, figures 31(c) and (f)), though the complex temporal evolution of $\mathbf{n}(\mathbf{r})$ with modulated U effectively changes their tilt relative to the 2D sample plane within each T_m [197]. Such dynamic dipolar skyrmions mutually repel at small U, but exhibit anisotropic dipolar-like interactions, including attractions, when the oscillating field **E** prompts symmetry breaking and motions [197]. **E** rotates preimage dipoles (connecting preimages of $\mathbb{S}^2$ poles of the vectorized $\mathbf{n}(\mathbf{r})$) from being orthogonal to the sample plane at $U = 0$ to being tilted or in-plane when U increases. Since the response of $\mathbf{n}(\mathbf{r})$ to oscillating U is fast (10–100 ms) compared to the timescales of skyrmion motions at $\sim$1 μm s^{-1}, tuning $\mathbf{n}(\mathbf{r})$ by U and frequency f modifies elastic forces and prompts cohesion within schools of skyrmions. The emergent behavior and orientational-elasticity-mediated pair and many-body interactions of such topological solitons can be understood as that of elastic dipoles with periodically oscillating tilt with respect to the 2D sample plane (figure 32) [197]. The nature of instantaneous interactions between continuously morphing solitons effectively changes within each T_m, but the overall collective behavior then arises from the cumulative effects of T_m-averaged instantaneous interactions (figures 32(a)–(c)). This behavior gives origin to a variety of emergent types of behavior of moving solitonic assemblies (figure 32(a)) and schools of solitons (figures 32(b)–(e)).

In the presence of thousands-to-millions of skyrmions, applied **E** initially induces random tilting of the director around individual skyrmions, so that their south–north preimage unit vectors $\mathbf{p}_i = \mathbf{P}_i/|\mathbf{P}_i|$ initially point in random in-plane directions. Individual skyrmions exhibit translational motions with velocity vectors $\mathbf{v}_i$ roughly antiparallel to their $\mathbf{p}_i$. With time, coherent directional motions emerge, with schooling of skyrmions either individually dispersed (figures 32(b) and (c)) or within various cluster-like assemblies [197]. Velocity and polar order parameters $S_v = |\sum_i^N \mathbf{v}_i|/(N v_s)$ and $S_p = |\sum_i^N \mathbf{p}_i|/N$ characterize degrees of ordering of $\mathbf{v}_i$ and $\mathbf{p}_i$ within the moving schools, where N is the number of skyrmionic particles and v_s is the absolute value of velocity of a coherently moving school. Both order parameters increase from zero to $\sim$0.9 within seconds (figure 32(d)), indicating the emergence of coherent unidirectional motion of particle-like solitons. The dynamic elasticity-mediated assembly of multi-skyrmions within schools (figure 32) echoes nuclear physics models (where subatomic particles with high baryon numbers are modeled as clusters of elementary skyrmions [7]), with each skyrmion cluster characterized by a net total skyrmion number corresponding to a sum of topological invariants of elementary solitons within it [80, 81, 197]. Interestingly, one often observes dynamic fission and fusion of such clusters during the active schooling [197]. Figure 32(e) summarizes the schooling behavior of skyrmions within a structural diagram, showing electric reconfigurability of this emergent behavior [197]. It is surprising and unexpected that relatively simple topological solitons, the 2D skyrmions, exhibit such complex out-of-equilibrium behavior when powered by oscillating

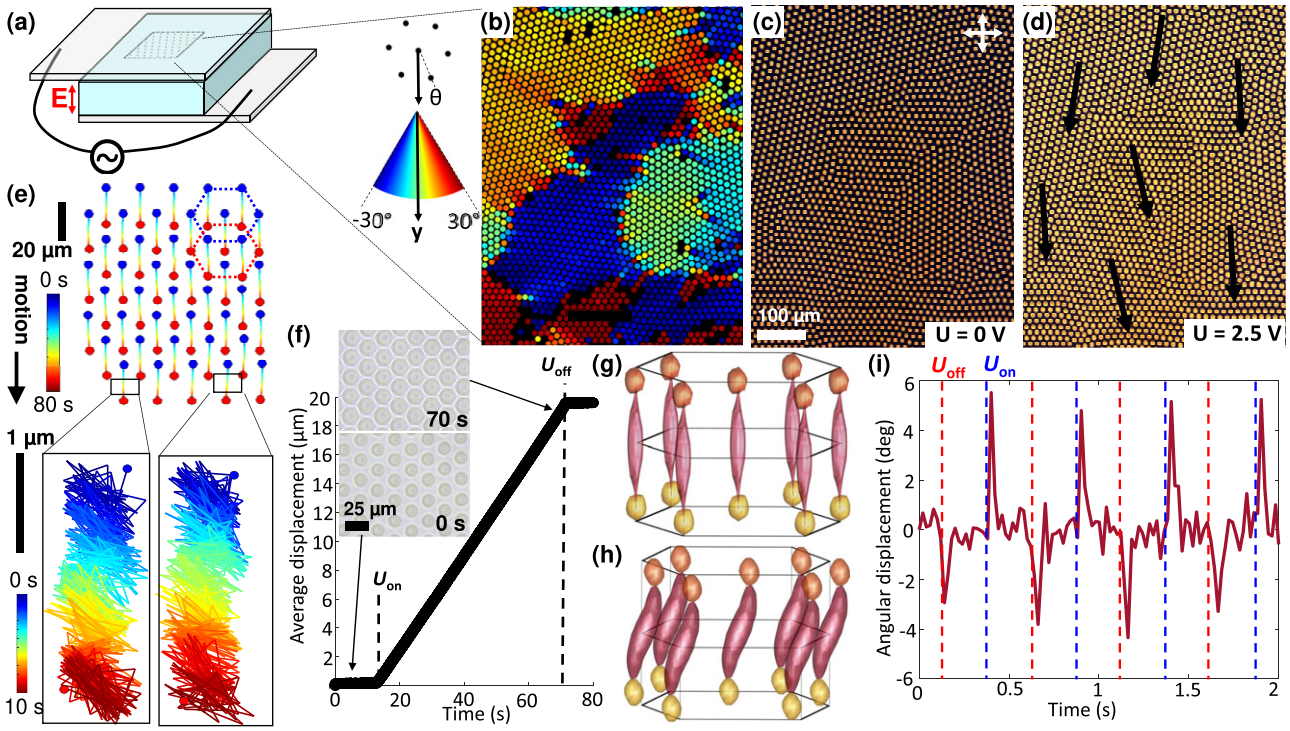

Figure 33. Dynamics of 2D crystallites of torons. (a) A schematic of crystallite motions powered by an electric field orthogonal to the cell substrates. (b)–(d) Crystallites of torons colored according to orientations relative to the average motion direction (b) and shown in polarizing micrographs at zero applied voltage (c) and at $U = 2.5$ V (d); black arrows in (d) denote crystallite motion directions. The color scheme for visualizing crystallite orientations in (b) is shown in the inset between (a) and (b). (e) Trajectories of crystallite motions at $U = 2.5$ V, $f = 10$ Hz, progressively zooming in on the details of translations, colored according to elapsed time (with the maximum elapsed time marked in each part); dashed hexagons indicate the unit cell shift during motion, colored according to the color-coded timescale. (f) Average displacement of the hyperbolic point defects near the confining substrate, analyzed with bright-field microscopy (video frames in insets). (g) and (h) South-pole preimages (magenta) and point defects (orange and yellow) of a hexagonal unit cell of torons shown (g) before and (h) during motion. (i) Nonreciprocal angular rotations of torons within crystallites upon voltage modulation, with the times of turning instantaneous voltage on and off marked by the blue and red dashed vertical lines. Reproduced with permission from [196].

electric fields. How can this behavior be altered further by increasing the number density of the solitons and by the presence of singular point defects co-existing with the skyrmions (e.g. within the elementary toron structures)? This question is addressed below.

6.3. *Crystals of moving torons*

Let us now consider an experimental geometry similar to that discussed above for skyrmions (figure 33(a)), but with dense polycrystalline arrays of torons (figures 33(b) and (c)). An oscillating field **E** applied to a chiral LC with such polycrystalline arrangements of torons prompts motions of crystallites and lattice defects (figure 33(d)), showing behavior very different from that of the skyrmions discussed above [196]. **E** is again applied orthogonally to cell substrates, and motions emerge along a spontaneously selected direction in a plane orthogonal to **E** (figures 33(a)–(d)). The crystallites have different orientations of crystallographic axes of the quasi-hexagonal lattice relative to the average motion direction before and during motion (figures 33(b)–(d)). The temporal evolution of deformations of the complex director field upon turning U on and off is not invariant upon time reversal, prompting lateral translations of torons, which synchronize to yield coherent motions of the crystallites of torons within quasi-hexagonal periodically deformed lattices (figure 33) [196]. Although the average direction of motion of toron crystallites is well defined, individual torons within the lattices execute rather elaborate 'dancing-like' dynamics (figure 33(e)), where local translations in directions other than motion direction average out over longer periods of time. As a result, the primitive cells of crystals of torons are translated along the average motion direction (figure 33(e)) with velocities approaching a micrometer per second range (figure 33(f)). While there is no net displacement of toron lattices and both skyrmions and singular point defects within them at zero applied field (though thermal fluctuations of toron positions are present), this displacement becomes linear in time soon after the periodically oscillating voltage is applied (figure 33(f)). Numerical modeling and experiments reveal that this motion is accompanied by voltage U-dependent lateral shifts of hyperbolic point defects and tilts/deformations of preimages compared to those at $U = 0$ (figures 33(g) and (h)). This electrically powered self-shearing of torons is apparent when visualizing the south-pole preimages and lateral shifts of the singular point defects at opposite confining surfaces (figure 33(h)), as well as it can be inferred from tracking point defects in bright-field microscopy (insets of figure 33(f)). Furthermore, all the preimages also rotate

around an axis normal to the sample plane [196] (figure 33(i)). As voltage is effectively turned on and off within each period of square-wave modulation, the toron's preimages rotate counterclockwise and clockwise (figure 33(i)), so that the director evolution that is manifested through such textural changes is not invariant upon reversal of time (figure 33(i)). Collective motions of crystallites of these solitons prompt fascinating evolution of grain boundaries and 5–7 defects [196], which are not generated by external stresses (like this would be the case, for example, during mechanical deformation of crystalline solids) but rather emerge from collective motions of crystallites of topological solitons within the material's interior, powered by the conversion of energy on an individual soliton basis. Furthermore, these complex dynamics arise from facile responses of the LC to external fields, which can be related to periodic morphing of knotted director streamlines within each toron [81], like those depicted in figure 20 [196], further enriched by electrically powered periodic shearing and dynamics of lattice defects. The collective dynamics of torons within lattices increases the hexatic order parameter and also causes polar ordering of asymmetrically sheared solitons, as well as leads to rather high-velocity order parameters, which are all rather unexpected emergent properties [196]. These findings show that, being 'activated' by supplying energy that is converted into motion locally, singular point defects, torons, skyrmions and various other knotted solitonic field configurations can emerge as a new breed of topological active matter [80, 81, 196, 197, 202–205].

6.4. Utility of the activated solitonic matter

While motion of individual solitons and their schools or crystals can take place with no or very little advection, these dynamic textures of $\mathbf{n}(\mathbf{r})$ can be used for transporting colloidal micro-cargo with well-defined surface boundary conditions by coupling the localized director textures with the solid particles through surface-anchoring boundary conditions [81]. It is tempting to again draw an analogy of such particle transportation with the so-called 'crowd surfing' typically enjoyed by concert performers, where the relatively static crowd transports the artist with localized dynamics of moving hands. However, it is important to note that the soliton-assisted transportation of colloidal particles throughout the LC generates more significant (though still localized) fluid flows [81]. Considering that the 'activated' topological solitons can be realized in very diverse synthetic material systems under geometry and sample preparation conditions similar to those of LC displays [197], their out-of-equilibrium emergent behavior might be of interest for technological applications, ranging from microfluidics to dynamic diffraction gratings and singular optics. For example, one can envisage their use in generating emergent patterns of polarization and intensity of light (including optical vortices and knots made from them) by exploiting optical properties of the uniaxial LC host media. Since torons and skyrmions can also be pinned to surfaces in desired locations using laser tweezers, further control of their out-of-equilibrium behavior like jamming was recently achieved by combining static (often serving as obstacles) and dynamic topological solitons [80, 195, 198]. In general, the combination of topological protection, reconfigurability and the facile response of the optically anisotropic LC host medium makes the topological solitons ideal for applications in various emergent technologies and as model systems in fundamental research.

7. Open questions, opportunities and perspectives

While the study of knotted and other topological structures in soft matter attracts a great deal of interest, many fundamental questions remain to be answered, including a systematic classification of these configurations, the allowed transformations between them, their physical stability and how to use one form of knotted fields to create and imprint other forms. The large variety of symmetries accessible within the selection of soft matter host media (figure 1) [13] will allow one to gain insights into stability, transformation and dynamics of fully nonsingular and singular knotted fields. The open questions to be answered include the following. What restrictions do different material symmetries impose on the knot types that can be realized? Which knot invariants have physical significance for each knotted field realization? How do soliton-type and singular knotted fields co-exist with each other and with other topological defects, colloids and confining surfaces? How do director fields switch between different knotted states? What new knotted condensed matter phases are possible for different symmetries? What are the mechanisms by which knotted fields are stabilized? When knots decay or emerge within a uniform background, what are the topological cascades of knot types in different systems? What is the relation between topological complexity and energy landscapes? Can turbulence be engineered in LC fluids through imprinting knotted flow structures, like in microfluidics embodiments [205, 206]? How do knotted structures in a complex soft matter medium interact? What types of dynamics and active-particle-like motion of singular knots [206, 207] of line defects and topological solitons in 3D active nematics can be realized? Can interaction of knotted structures and confining surfaces be controlled [208]? What are the implications of knotting of vortex lines in LCs on the structure of their cores [209–212]? How extensions of topological concepts to dynamical phenomena can lead to entanglement of dynamic and static material properties. Could active nematics or passive nematics with activated dynamics of defects host soft matter analogs of instantons [7]? Can knotted optical fields act as templates to excite knotted LC and ferromagnetic states, and vice versa? Orientationally ordered soft matter provides unique opportunities for integrating analytical, numerical and analog modeling with experiments to answer the above questions.

While topologically protected knotted solitons and vortices can exhibit behavior similar to that of particles, with effective dimensions in nanometer and micrometer ranges, it is of interest to explore how such structures interact and coexist with colloidal particles in LC colloidal dispersions, gels and emulsions [213–218]. Preliminary studies in this direction have appeared already [219, 220], demonstrating that colloidal particles immersed in LCs can be accompanied by combinations of solitonic and singular structures, but more extensive

research explorations are still needed. For example, 3D solitons like heliknotons could effectively bond with colloidal objects to form hybrid soliton–colloidal crystals, or instead new breeds of hybrid structures could arise from their interactions. These studies could lead to sparse but ordered open and closed 2D and 3D lattices of colloidal superstructures [73, 221], or may also diversify our abilities to knott nematic field configurations. If thinking about both colloids and solitons as 'big atoms', this may also significantly expand our abilities to model atomic and molecular systems with soft matter, as well as going beyond what is accessible to atomic and molecular building blocks in terms of symmetries of organization, responses to external stimuli, etc.

Throughout the article, relations between topological structures in soft matter and those in other branches of science have been mentioned. Experimental realizations and a deeper understanding of, for example, hopfions and heliknotons in solid-state magnetic systems may be aided by explorations of such structures in LCs and colloids [24, 42, 44, 73]. Indeed, the synergy in studies of these solitons in different systems is even beyond just the topological equivalence and analogy, and can build on the similarity of free-energy functionals, various types of surface and bulk anisotropies, field couplings, etc [42, 44]. In many other physical systems, like elementary particle physics and cosmology, structures of fields are not experimentally accessible and, thus, ordered soft matter media can provide much needed model systems and deeper insights [7]. On the other hand, synergy can be developed in explorations of topological configurations, even within different soft matter systems. For example, Petit-Garrido and others [222, 223] demonstrated how vortices within molecular monolayers can imprint arches of singular disclinations within LCs in contact with them, but such study could also involve topological solitons and knotted vortices. Having self-assembled monolayers made of photo-responsive molecules, e.g. those containing azobenzene, may enable interesting dynamics, similar to what was observed for spiraling 1D solitons [224], but now this could be extended to higher-dimensional solitons, like skyrmions and hopfions.

In addition to the most common examples discussed above, more complex LCs and colloids can be characterized by a variety of other types of order parameters and the corresponding order parameter spaces (figures 1(c) and (d)). For example, particularly interesting high-dimensional order parameter spaces in these soft matter systems are $\mathrm{SO}(3) = \mathbb{S}^3/\mathbb{Z}_2$ of the monoclinic biaxial colloidal ferromagnets [225] (figure 1(d)) and $\mathrm{SO}(3)/D_2 = \mathbb{S}^3/Q_8$ of the orthorhombic biaxial nematics (figure 1(c)) [226]. The types of anticipated/allowed defects and solitons in these systems are understood on the basis of homotopy theory, with one particularly interesting example being the nonabelian line defects in the orthorhombic biaxial nematic LC, $\pi_1(\mathbb{S}^3/Q_8) = Q_8$ [227], but little is known about the interactions of these soft matter systems with confining and colloidal surfaces of complex topology, and even the fundamental properties of these defects have not been probed experimentally. What types of solitonic and singular knotted field configurations can exist in these biaxial low-symmetry nematics and colloidal ferromagnets? For example, $\pi_3(\mathbb{S}^3/Q_8) = \mathbb{Z}$ and $\pi_3(\mathbb{S}^3/\mathbb{Z}_2) = \mathbb{Z}$ topological solitons in biaxial nematics and ferromagnetic LCs would be rather interesting analogs of the Skyrme solitons in high-energy physics, but can they emerge as global or local free-energy minima in these soft matter systems? What would be the fate of various solitonic and singular knots during monoclinic–orthorhombic, orthorhombic–uniaxial nematic and various other phase transitions involving these mesophases? It is only now that researchers can start addressing such fundamentally important questions because these soft matter systems have become experimentally accessible [225, 226]. The recent demonstration of 3D active nematics [207] also promises a variety of new opportunities in realizing various out-of-equilibrium knotted vortices and solitons. For example, both active [207, 228–234] and out-of-equilibrium passive LCs with 'activated' dynamic defects [80, 81, 195–198] could reveal various analogs of topological instantons and nontrivial topological connectivity, where the dynamics of defects and topological solitons could even lead to the formation of topological field configurations in a different class, including various knotted field configurations. Although topological objects in soft matter can be realized only in 1D-to-3D physical configuration spaces (figure 5), time in certain cases can be treated as an additional spatial dimension (say $\mathbb{R}^{3+1}$ for a 3D configuration space with certain special temporal dynamics and the corresponding $\mathbb{S}^4$ compactification) [7, 235], so that an interesting question arises if topological objects predicted by the homotopy theory and labeled as $\pi_4(\mathbb{S}^2) = \mathbb{Z}_2$ and $\pi_4(\mathbb{S}^3) = \mathbb{Z}_2$ could be potentially realized in out-of-equilibrium soft matter systems. At the same time, active matter behavior, curvatures of confining surfaces and orientational polar or nematic order could interplay to yield interesting topological effects that are analogous to topology-enabled phenomena recently widely studied in quantum materials [1, 234], with many new interesting possibilities arising and in need of exploration.

While recent advances in the study of topologically nontrivial structures in soft matter have primarily fundamental importance, they could also be useful in various applications, extending the scope of what is done already in relation to more classic types of topological defects. For example, controlled patterning of defects in thin photo- and thermally-responsive LC elastomeric films recently enabled tuning surface topography, e.g. inducing cone- and saddle-like deformations of thin films and oscillating surface profiles [236–238]. These ideas can be extended to skyrmions, hopfions and heliknotons, where the topologically protected nature of these field configurations can be utilized to produce well-defined localized mechanical responses, much like with singular defects [236–238], but now with a considerably larger inventory of possibilities. Conversely, topographic features at LC interfaces can be used to define and pattern spatial positions of various knot solitons by harnessing interactions mediated by the LC's orientational elasticity, much like colloidal particles in nematic LCs could be attracted by topographic features like pyramids [239]. On the other hand, optical effective refractive index patterns associated with various arrays of solitons with and without lattice defects can be utilized to generate tunable diffraction patterns and optical vortices in laser beams [162, 163, 240, 241],

where 3D topological solitons like heliknotons [73] within crystalline arrays may again allow for much needed reconfigurability in defining these diffractive elements and optical vortex generators. It will be interesting to explore how various linear and nonlinear optical interactions within LCs can be exploited to use topological solitons in guiding laser beams of light and optical solitons like nematicons [242, 243], as well as how these interactions can potentially be controlled by nanoconfinement [244] and enable practical applications in beam steering and telecommunications.

Acknowledgments

IIS is grateful to M Bowick, J-S B Tai Shokef Y and B Senyuk for helpful discussions. The author would like to thank his students and postdocs at the University of Colorado, Boulder who have been working on research topics related to this review, including P J Ackerman, H Mundoor, C Meng, A J Hess, H R O Sohn, J-S B Tai, B Senyuk, J Brewer, Z Chen, J S Evans, M G Campbell, J Bourgeois, T Boyle, J-S Wu, C D Liu, Q Liu, A Martinez, H C Mireles, Y Wang, A J Funk, M J Laviada, I Klevets, C Lapointe, J Giller, S Park, O Puls, D Glugla, M C M Varney, Q Zhang, R Voinescu, C Twombly, G H Sheetah, A J Seracuse, M B Pandey, R P Trivedi, N P Garido, R Visvanathan, O Trushkevych. IIS acknowledges the financial support of the fundamental research on colloids (the U.S. Department of Energy, Office of Basic Energy Sciences, Division of Materials Sciences and Engineering, under Award ER46921, contract DE-SC0019293 with the University of Colorado in Boulder) and topological solitons (the U.S. National Science Foundation grant DMR-1810513), examples of which have been highlighted within this review. IIS also acknowledges the hospitality of the Kavli Institute for Theoretical Physics at the University of California, Santa Barbara, where he was working on this review during his extended stay and where his research was supported in part by the U.S. National Science Foundation under Grant No. NSF PHY-1748958.

ORCID iDs

Ivan I Smalyukh https://orcid.org/0000-0003-3444-1966

References

[1] Wen X-G 2019 Choreographed entanglement dances: topological states of quantum matter *Science* **363** eaal3099

[2] Mao X and Lubensky T C 2018 Maxwell lattices and topological mechanics *Annu. Rev. Condens. Matter Phys.* **9** 413–33

[3] Silver D 2006 Scottish physics and knot theory's odd origins (expanded version of Silver D 2006 Knot theory's odd origins *Am. Sci.* **94** 158–165) available from: https://southalabama.edu/mathstat/personal_pages/silver/scottish.pdf

[4] Turner J C and van de Griend P (ed) 1996 *History and Science of Knots* (Singapore: World Scientific)

[5] Thomson W 1867 II. On vortex atoms *London, Edinburgh Dublin Philos. Mag. J. Sci.* **34** 15–24

[6] Kauffman L H 2001 *Knots and Physics* (Singapore: World Scientific)

[7] Manton N and Sutcliffe P 2004 *Topological Solitons* (Cambridge: Cambridge University Press)

[8] Adams C 2004 *The Knot Book: An Elementary Introduction to the Mathematical Theory of Knots* (Providence, RI: American Mathematical Society)

[9] Collins G 2006 Computing with quantum knots *Sci. Am.* **294** 56–63

[10] Hoste J 2005 The enumeration and classification of knots and links *Handbook of Knot Theory* ed W Menasco and M Thistlethwaite (Amsterdam: Elsevier)

[11] Lickorish W B R 1997 *An Introduction to Knot Theory* (*Graduate Texts in Mathematics*) (Berlin: Springer)

[12] de Gennes P G and Prost J 1993 *The Physics of Liquid Crystals* 2nd edn (Oxford: Clarendon)

[13] Chaikin P M and Lubensky T C 1995 *Principles of Condensed Matter Physics* (Cambridge: Cambridge University Press)

[14] Hunter R J 2001 *Foundations of Colloid Science* (New York: Oxford University Press)

[15] Crawford G P and Žumer S 1996 *Liquid Crystals in Complex Geometries Formed by Polymer and Porous Networks* (London: Taylor and Francis)

[16] The Nobel Prize in Physics 2016 NobelPrize.org Nobel Media AB 2020 [online] available from: https://nobelprize.org/prizes/physics/2016/summary/ [accessed 4 Jan 2020]

[17] Kosterlitz J M 2016 Kosterlitz-Thouless physics: a review of key issues *Rep. Prog. Phys.* **79** 026001

[18] Fisher M E and Nagaosa N 2017 Profile of David J. Thouless, J. Michael Kosterlitz, and F. Duncan M. Haldane, 2016 Nobel laureates in physics *Proc. Natl Acad. Sci. USA* **114** 626–8

[19] Kleckner D and Irvine W T M 2013 Creation and dynamics of knotted vortices *Nat. Phys.* **9** 253–8

[20] Kleckner D, Kauffman L H and Irvine W T M 2016 *Nat. Phys.* **12** 650–5

[21] Skyrme T H R 1961 A non-linear field theory *Proc. R. Soc.* A **260** 127–38

[22] Faddeev L and Niemi A J 1997 Stable knot-like structures in classical field theory *Nature* **387** 58–61

[23] Krause S and Wiesendanger R 2016 Spintronics: skyrmionics gets hot *Nat. Mater.* **15** 493–4

[24] Ackerman P J and Smalyukh I I 2017 Static three-dimensional topological solitons in fluid chiral ferromagnets and colloids *Nat. Mater.* **16** 426–32

[25] Buniy R V and Kephart T W 2005 Glueballs and the universal energy spectrum of tight knots and links *Int. J. Mod. Phys.* A **20** 1252–9

[26] Sutcliffe P 2017 Skyrmion knots in frustrated magnets *Phys. Rev. Lett.* **118** 247203

[27] Kedia H, Bialynicki-Birula I, Peralta-Salas D and Irvine W T M 2013 Tying knots in light fields *Phys. Rev. Lett.* **111** 150404

[28] Dennis M R, King R P, Jack B, O'Holleran K and Padgett M J 2010 Isolated optical vortex knots *Nat. Phys.* **6** 118–21

[29] Liu X and Ricca R L 2016 Knots cascade detected by a monotonically decreasing sequence of values *Sci. Rep.* **6** 24118

[30] Milnor J W 1965 *Topology from the Differentiable Viewpoint* (Charlottesville, VA: University Press of Virginia)
[31] Herges R 2006 Topology in chemistry: designing mobius molecules *Chem. Rev.* **106** 4820–42
[32] Smalyukh I I, Lansac Y, Clark N and Trivedi R 2010 Three-dimensional structure and multistable optical switching of triple twist toron quasiparticles in anisotropic fluids *Nat. Mater.* **9** 139–45
[33] Tkalec U, Ravnik M, Čopar S, Žumer S and Muševič I 2011 Reconfigurable knots and links in chiral nematic colloids *Science* **333** 62–5
[34] Senyuk B, Liu Q, He S, Kamien R D, Kusner R, Lubensky T C and Smalyukh I I 2013 Topological colloids *Nature* **493** 200–5
[35] Martinez A, Ravnik M, Visvanathan R, Lucero B, Žumer S and Smalyukh I I 2014 *Nat. Mater.* **13** 258–63
[36] Machon T and Alexander G P 2013 Knots and nonorientable surfaces in chiral nematics *Proc. Natl Acad. Sci. USA* **110** 14174–9
[37] Irvine W and Bouwmeester D 2008 Linked and knotted beams of light *Nat. Phys.* **4** 716–20
[38] Larocque H, Sugic D, Mortimer D, Taylor A J, Fickler R, Boyd R W, Dennis M R and Karimi E 2018 Reconstructing the topology of optical polarization knots *Nat. Phys.* **14** 1079–82
[39] Kedia H, Foster D, Dennis M R and Irvine W T M 2016 Weaving knotted vector fields with tunable helicity *Phys. Rev. Lett.* **117** 274501
[40] Hall D S, Ray M W, Tiurev K, Ruokokoski E, Gheorghe A H and Möttönen M 2016 Tying quantum knots *Nat. Phys.* **12** 478–83
[41] Lee W, Gheorghe A H, Tiurev K, Ollikainen T, Möttönen M and Hall D S 2018 Synthetic electromagnetic knot in a three-dimensional skyrmion *Sci. Adv.* **4** eaao3820
[42] Tai J-S B and Smalyukh I I 2018 Static Hopf solitons and knotted emergent fields in solid-state noncentrosymmetric magnetic nanostructures *Phys. Rev. Lett.* **121** 187201
[43] Wang X S, Qaiumzadeh A and Brataas A 2019 Current-driven dynamics of magnetic hopfions *Phys. Rev. Lett.* **123** 147203
[44] Voinescu R, Tai J-S B and Smalyukh I I 2020 Hopf solitons in helical and conical backgrounds of chiral magnetic solids *Phys. Rev. Lett.* **125** 057201
[45] Bornschlögl T, Anstrom D M, Mey E, Dzubiella J, Rief M and Forest K T 2009 Tightening the knot in phytochrome by single-molecule atomic force microscopy *Biophys. J.* **96** 1508–14
[46] Ricca R L and Berger M A 1996 Topological ideas and fluid mechanics *Phys. Today* **49** 28–34
[47] Moffatt H K, Bajer K and Kimura Y (ed) 2013 Topological fluid dynamics, theory and applications *Procedia IUTAM* vol 7 1–260
[48] Hasan M Z and Kane C L 2010 Colloquium: topological insulators *Rev. Mod. Phys.* **82** 3045–67
[49] de Gennes P-G 1992 Soft matter (Nobel lecture) *Angew. Chem., Int. Ed.* **31** 842–5
[50] Bowick M J, Chandar L, Schiff E A and Srivastava A M 1994 The cosmological Kibble mechanism in the laboratory: string formation in liquid crystals *Science* **263** 943–5
[51] Han Y, Alsayed Y A M, Nobili M, Zhang J, Lubensky T C and Yodh A G 2006 Brownian motion of an ellipsoid *Science* **314** 626–30
[52] Solomon M J 2011 Directions for targeted self-assembly of anisotropic colloids from statistical thermodynamics *Curr. Opin. Colloid Interface Sci.* **16** 158–67
[53] Poulin P, Stark H, Lubensky T C and Weitz D A 1997 Novel colloidal interactions in anisotropic fluids *Science* **275** 1770–3
[54] Smalyukh I I, Lavrentovich O D, Kuzmin A, Kachynski A and Prasad P N 2005 Elasticity-mediated self-organization and colloidal interactions of solid spheres with tangential anchoring in a nematic liquid crystal *Phys. Rev. Lett.* **95** 157801
[55] Smalyukh I I 2018 Liquid crystal colloids *Annu. Rev. Condens. Matter Phys.* **9** 207–26
[56] Beer R 1999 *The Encyclopedia of Tibetan Symbols and Motifs* (Boston: Shambhala Publications, Inc.)
[57] Ashley C W 1944 *The Ashley Book of Knots* (New York: Doubleday)
[58] Patil V P, Sandt J D, Kolle M and Dunkel J 2020 Topological mechanics of knots and tangles *Science* **367** 71–5
[59] Skyrme T H R 1988 The origins of skyrmions *Int. J. Phys.* A **3** 2745–51
[60] Adkins G S, Nappi C R and Witten E 1983 Static properties of nucleons in the Skyrme model *Nucl. Phys.* B **228** 552–66
[61] Witten E 1989 Quantum field theory and the Jones polynomial *Commun. Math. Phys.* **121** 351–99
[62] Dauxois T and Peyrard M 2006 *Physics of Solitons* (Cambridge: Cambridge University Press)
[63] Ablowitz M J 2011 *Nonlinear Dispersive Waves, Asymptotic Analysis and Solitons* (Cambridge: Cambridge University Press)
[64] Kuei S, Słowicka A M, Ekiel-Jeżewska M L, Wajnryb E and Stone H A dynamics and topology of a flexible chain: knots in steady shear flow *New J. Phys.* **17** 053009
[65] Stolz R, Yoshida M, Brasher R, Flanner M, Ishihara K, Sherratt D J, Shimokawa K and Vazquez M 2017 Pathways of DNA unlinking: a story of stepwise simplification *Sci. Rep.* **7** 12420
[66] Klotz A R, Soh B W and Doyle P S 2018 Motion of knots in DNA stretched by elongational fields *Phys. Rev. Lett.* **120** 188003
[67] Virnau P, Mirny L A and Kardar M 2006 Intricate knots in proteins: function and evolution *PLoS Comput. Biol.* **2** e122
[68] Lua R C and Grosberg A Y 2006 Statistics of knots, geometry of conformations, and evolution of proteins *PLoS Comput. Biol.* **2** e45
[69] Liu Q, Senyuk B, Tasinkevych M and Smalyukh I I 2013 Nematic liquid crystal boojums with handles on colloidal handlebodies *Proc. Natl Acad. Sci. USA* **110** 9231–6
[70] Senyuk B, Liu Q, Yuan Y and Smalyukh I I 2016 Edge pinning and transformation of defect lines induced by faceted colloidal rings in nematic liquid crystals *Phys. Rev.* E **93** 062704
[71] Yuan Y and Smalyukh I I 2015 Topological nanocolloids with facile electric switching of plasmonic properties *Opt. Lett.* **40** 5630–3
[72] Martinez A, Hermosillo L, Tasinkevych M and Smalyukh I I 2015 Linked topological colloids in a nematic host *Proc. Natl Acad. Sci. USA* **112** 4546–51
[73] Tai J-S B and Smalyukh I I 2019 Three-dimensional crystals of adaptive knots *Science* **365** 1449–53
[74] Mermin N D 1979 The topological theory of defects in ordered media *Rev. Mod. Phys.* **51** 591–648
[75] Toulouse G and Kléman M 1976 Principles of a classification of defects in ordered media *J. Phys. Lett.* **37** 149–51
[76] Finkelstein D J 1966 Kinks *Math. Phys.* **7** 1218–25
[77] Armstrong M A 1979 *Basic Topology* (Berlin: Springer)
[78] Hazewinkel M (ed) 1994 *Homotopy, Encyclopedia of Mathematics* (Berlin: Springer)
[79] Tai J-S B and Smalyukh I I 2020 Surface anchoring as a control parameter for stabilizing torons, skyrmions, twisted walls, fingers and their hybrids in chiral nematics *Phys. Rev.* E **191** 042702
[80] Ackerman P J, Boyle T and Smalyukh I I 2017 Squirming motion of baby skyrmions in nematic fluids *Nat. Commun.* **8** 673
[81] Sohn H R O, Ackerman P J, Boyle T J, Sheetah G H, Fornberg B and Smalyukh I I 2018 Dynamics of topological solitons,

knotted streamlines, and transport of cargo in liquid crystals *Phys. Rev.* E **97** 052701
[82] Jänich K 1987 Topological properties of ordinary nematics in 3-space *Acta. Appl. Math.* **8** 65–74
[83] Sethna J P 2006 *Statistical Mechanics: Entropy, Order Parameters, and Complexity* (Oxford: Oxford University Press)
[84] Machon T 2019 The topology of knots and links in nematics *Liq. Cryst. Today* **28** 58–67
[85] Čopar S and Žumer S 2011 Nematic braids: topological invariants and rewiring of disclinations *Phys. Rev. Lett.* **106** 117801
[86] Čopar S 2014 Topology and geometry of nematic braids *Phys. Rep.* **538** 1–37
[87] Lubensky T C, Pettey D, Currier N and Stark H 1998 Topological defects and interactions in nematic emulsions *Phys. Rev.* E **57** 610–25
[88] Gu Y and Abbott N L 2000 Observation of saturn-ring defects around solid microspheres in nematic liquid crystals *Phys. Rev. Lett.* **85** 4719–22
[89] Ramaswamy S, Nityananda R, Raghunathan V A and Prost J 1996 Power-law forces between particles in a nematic *Mol. Cryst. Liq. Cryst.* **288** 175–80
[90] Kléman M 1983 *Points, Lines, and Walls: Liquid Crystals, Magnetic Systems, and Various Ordered Media* (New York: Wiley)
[91] Manoharan V N 2015 Colloidal matter: packing, geometry, and entropy *Science* **349** 1253751
[92] Senyuk B, Puls O, Tovkach O M, Chernyshuk S B and Smalyukh I I 2016 Hexadecapolar colloids *Nat. Commun.* **7** 10659
[93] Zhou Y, Senyuk B, Zhang R, Smalyukh I I and de Pablo J J 2019 Degenerate conic anchoring and colloidal elastic dipole-hexadecapole transformations *Nat. Commun.* **10** 1000
[94] Sheetah G H, Liu Q, Senyuk B, Fleury B and Smalyukh I I 2018 Electric switching of visible and infrared transmission using liquid crystals co-doped with plasmonic gold nanorods and dichroic dyes *Opt. Express* **26** 22264–72
[95] Sheetah G H, Liu Q and Smalyukh I I 2016 Self-assembly of pre-designed optical materials in nematic codispersions of plasmonic nanorods *Opt. Lett.* **41** 4899–902
[96] Jiang L, Mundoor H, Liu Q and Smalyukh I I 2016 Electric switching of fluorescence decay in gold-silica-dye nematic nanocolloids mediated by surface plasmons *ACS Nano* **10** 7064–72
[97] Mundoor H and Smalyukh I I 2015 Mesostructured composite materials with electrically tunable upconverting properties *Small* **11** 5572–80
[98] Zhang Y, Liu Q, Mundoor H, Yuan Y and Smalyukh I I 2015 Metal nanoparticle dispersion, alignment and assembly in nematic liquid crystals for applications in switchable plasmonic color filters and E-polarizers *ACS Nano* **9** 3097–108
[99] Kachynski A V, Kuzmin A N, Prasad P N and Smalyukh I I 2008 Realignment-enhanced coherent anti-Stokes Raman scattering (CARS) and three-dimensional imaging in anisotropic fluids *Opt. Express* **16** 10617–32
[100] Kachynskii A, Kuzmin A, Prasad P N and Smalyukh I I 2007 Coherent anti-Stokes Raman scattering (CARS) polarized microscopy of three-dimensional director structures in liquid crystals *Appl. Phys. Lett.* **91** 151905
[101] Trivedi R P, Lee T, Bertness K and Smalyukh I I 2010 Three dimensional optical manipulation and structural imaging of soft materials by use of laser tweezers and multimodal nonlinear microscopy *Opt. Express* **18** 27658–69
[102] Lee T, Trivedi R P and Smalyukh I I 2010 Multimodal nonlinear optical polarizing microscopy of long-range molecular order in liquid crystals *Opt. Lett.* **35** 3447–9
[103] Tai J-S B and Smalyukh I I 2018 Super-resolution stimulated emission depletion microscopy of director structures in liquid crystals *Opt. Lett.* **43** 5158–61
[104] Mermin N D 1981 E Pluribus Boojum: the physicist as neologist *Phys. Today* **34** 46–53
[105] Mermin N D 1990 *Boojums All the Way Through: Communicating Science in a Prosaic Age* (Cambridge: Cambridge University Press)
[106] Lavrentovich O D 1998 Topological defects in dispersed liquid crystals, or words and worlds around liquid crystal drops *Liq. Cryst.* **24** 117–25
[107] Fang J, Teer E, Knobler C M, Loh K-K and Rudnick J 1997 Boojums and the shapes of domains in monolayer films *Phys. Rev.* E **56** 1859–68
[108] Takeuchi H and Tsubota M 2006 Boojums in rotating two-component Bose–Einstein condensates *J. Phys. Soc. Japan* **75** 063601
[109] Tasinkevych M, Silvestre N M and Telo da Gama M M 2012 Liquid crystal boojum-colloids *New J. Phys.* **14** 073030
[110] Kralj S, Rosso R and Virga E G 2008 Fingered core structure of nematic boojums *Phys. Rev.* E **78** 031701
[111] Tran L, Lavrentovich M O, Beller D A, Ningwei L, Stebe K J and Kamien R D 2016 Lassoing saddle splay and the geometrical control of topological defects *Proc. Natl Acad. Sci. USA* **113** 7106–11
[112] Martinez A, Lee T, Asavei T, Rubinsztein-Dunlop H and Smalyukh I I 2012 Multi-photon self-fluorescence imaging of director structures induced by low-symmetry two-photon-polymerized particles in liquid crystals *Soft Matter* **8** 2432–7
[113] Hashemi S M and Ravnik M Nematic colloidal knots in topological environments *Soft Matter* **14** 4935–45
[114] Ravnik M, Čopar S and Žumer S 2015 Particles with changeable topology in nematic colloids *J. Phys. Condens. Matter* **27** 354111
[115] Jampani V S R, Škarabot M, Ravnik M, Čopar S, Žumer S and Muševič I 2011 Colloidal entanglement in highly twisted chiral nematic colloids: twisted loops, Hopf links, and trefoil knots *Phys. Rev.* E **84** 031703
[116] Machon T and Alexander G P 2014 Knotted defects in nematic liquid crsytals *Phys. Rev. Lett.* **113** 027801
[117] Yuan Y, Liu Q, Senyuk B and Smalyukh I I 2019 Elastic colloidal monopoles and out of equilibrium interactions in liquid crystals *Nature* **570** 214–8
[118] Yuan Y, Abuhaimed G N, Liu Q and Smalyukh I I 2018 Light-driven spinning of colloidal micro-wheels *Nat. Commun.* **9** 5040
[119] Senyuk B, Liu Q, Bililign E, Nystrom P D and Smalyukh I I 2015 Geometry-guided colloidal interactions and self-tiling of elastic dipoles formed by truncated pyramid particles in liquid crystals *Phys. Rev.* E **91** 040501
[120] Dontabhaktuni J, Ravnik M and Žumer S 2014 Quasicrystalline tilings with nematic colloidal platelets *Proc. Natl Acad. Sci. USA* **111** 2464–9
[121] Ramaswamy S 2010 The mechanics and statistics of active matter *Annu. Rev. Condens. Matter Phys.* **1** 323–45
[122] Simmchen J, Katuri J, Uspal W E, Popescu M N, Tasinkevych M and Sanchez S 2016 Topographical pathways guide chemical microswimmers *Nat. Commun.* **7** 10598
[123] Baraban L, Tasinkevych M, Popescu M N, Sanchez S, Dietrich S and Schmidt O G 2012 Transport of cargo by catalytic Janus micro-motors *Soft Matter* **8** 48–52
[124] Trivedi R P, Engstrom D and Smalyukh I I 2011 Optical manipulation of colloids and defect structures in anisotropic liquid crystal fluids *J. Opt.* **13** 044001
[125] Senyuk B, Behabtu N, Martinez A, Lee T, Tsentalovich D E, Ceriotti G, Tour J M, Pasquali M and Smalyukh I

I 2015 Three-dimensional patterning of solid microstructures through laser reduction of colloidal graphene oxide in liquid-crystalline dispersions *Nat. Commun.* **6** 7157
[126] Varney M C M, Zhang Q and Smalyukh I I 2015 Stick-slip motion of surface point defects prompted by magnetically controlled colloidal-particle dynamics in nematic liquid crystals *Phys. Rev.* E **91** 052503
[127] Smalyukh I I, Kuzmin A, Kachynski A, Prasad P N and Lavrentovich O D 2005 Optical trapping of colloidal particles and measurement of the defect line tension and colloidal forces in a thermotropic nematic liquid crystal *Appl. Phys. Lett.* **86** 021913
[128] Smalyukh I I, Kachynski A V, Kuzmin A N and Prasad P N 2006 Laser trapping in anisotropic fluids and polarization-controlled particle dynamics *Proc. Natl Acad. Sci. USA* **103** 18048–53
[129] Martinez A, Mireles H C and Smalyukh I I 2011 Large-area optoelastic manipulation of colloidal particles in liquid crystals using photoresponsive molecular surface monolayers *Proc. Natl Acad. Sci. USA* **108** 20891–6
[130] Everts J C and Ravnik M 2018 Complex electric double layers in charged topological colloids *Sci. Rep.* **8** 14119
[131] Sacanna S, Irvine W, Chaikin P and Pine D J 2010 Lock and key colloids *Nature* **464** 575–8
[132] Stein D L 1979 Topological theorem and its applications to condensed matter systems *Phys. Rev.* A **19** 1708–11
[133] Volovik G E 1978 Topological singularities on the surface of an ordered system *JETP Lett.* **28** 59–62
[134] Volovik G E and Lavrentovich O D 1983 Topological dynamics of defects: boojums in nematic drops *Zh. Eksp. Teor. Fiz.* **85** 1997–2010
[135] Hud N V, Downing K H and Balhorn R 1995 A constant radius of curvature model for the organization of DNA in toroidal condensates *Proc. Natl Acad. Sci. USA* **92** 3581–5
[136] Kulic I M, Andrienko D and Deserno M 2004 Twist-bend instability for toroidal DNA condensates *Europhys. Lett.* **67** 418–24
[137] Michalet X and Bensimon D 1995 Observation of stable shapes and conformal diffusion in genus 2 vesicles *Science* **269** 666–8
[138] Jülicher F 1996 The morphology of vesicles of higher topological genus: conformal degeneracy and conformal modes *J. Phys. II* **6** 1797–824
[139] Hsu L, Kusner R and Sullivan J 1992 Minimizing the squared mean curvature integral for surfaces in space forms *Experiment. Math* **1** 191–207
[140] Seč D, Čopar S and Žumer S 2014 Topological zoo of free-standing knots in confined chiral nematic fluids *Nat. Commun.* **5** 3057
[141] Lopez-Leon T, Koning V, Vitelli V and Fernandez-Nieves A 2011 Frustrated nematic order in spherical geometries *Nat. Phys.* **7** 391–4
[142] Campbell M, Tasinkevych M and Smalyukh I I 2014 Topological polymer dispersed liquid crystals with bulk nematic defect lines pinned to handlebody surfaces *Phys. Rev. Lett.* **112** 197801
[143] Pairam E, Vallamkondu J, Koning V, van Zuiden B C, Ellis P W, Bates M A, Vitelli V and Fernandez-Nieves A 2013 Stable nematic droplets with handles *Proc. Natl Acad. Sci. USA* **110** 9295–300
[144] Tasinkevych M, Campbell M and Smalyukh I I 2014 Splitting, linking, knotting, and solitonic escape of topological defects in homeotropic nematic drops with handles *Proc. Natl Acad. Sci. USA* **111** 16268–73
[145] Ellis P, Pearce D, Chang Y, Goldsztein G, Giomi L and Fernandez-Nieves A 2018 Curvature-induced defect unbinding and dynamics in active nematic toroids *Nat. Phys.* **14** 85–90
[146] Mur U, Čopar S, Posnjak G, Muševič I, Ravnik M and Žumer S 2017 Ray optics simulations of polarized microscopy textures in chiral nematic droplets *Liq. Cryst.* **44** 679–87
[147] Posnjak G, Čopar S and Muševič I 2017 Hidden topological constellations and polyvalent charges in chiral nematic droplets *Nat. Commun.* **8** 14594
[148] Vilenkin A and Shellard E P S 1994 *Cosmic Strings and Other Topological Defects* (Cambridge: Cambridge University Press)
[149] De Vega H J, Khalatnikov I M and Sanchez N G 2001 *Phase Transitions in the Early Universe: Theory and Observations* (Dordrecht: Kluwer)
[150] Lopez-Leon T and Fernandez-Nieves A 2011 Drops and shells of liquid crystal *Colloid Polym. Sci.* **289** 345–59
[151] Urbanski M, Reyes C G, Noh J, Sharma A, Geng Y, Jampani V S R and Lagerwall J P F 2017 Liquid crystals in micron-scale droplets, shells and fibers *J. Phys. Condens. Matter* **29** 133003
[152] Nelson D R 2002 Toward a tetravalent chemistry of colloids *Nano Lett.* **2** 1125–9
[153] Giomi L, Bowick M J, Ma X and Majumdar A 2012 Molecular tilt on monolayer-protected nanoparticles *Europhys. Lett.* **97** 36005
[154] Araki T, Buscaglia M, Bellini T and Tanaka H 2011 Memory and topological frustration in nematic liquid crystals confined in porous materials *Nat. Mater.* **10** 303–9
[155] Park S, Liu Q and Smalyukh I I 2016 Colloidal surfaces with boundaries, apex boojums, and nested elastic self-assembly of nematic colloids *Phys. Rev. Lett.* **117** 277801
[156] Twombly C W, Evans J S and Smalyukh I I 2013 Optical manipulation of self-aligned graphene flakes in liquid crystals *Opt. Express* **21** 1324–34
[157] Lapointe C P, Mason T G and Smalyukh I I 2009 Shape-controlled colloidal interactions in nematic liquid crystals *Science* **326** 1083–6
[158] Pergamenshchik V M and Uzhunova V A 2011 Dipolar colloids in nematostatics: tensorial structure, symmetry, different types, and their interaction *Phys. Rev.* E **83** 021701
[159] Trivedi R P, Klevets I I, Senyuk B, Lee T and Smalyukh I I 2012 Reconfigurable interactions and three-dimensional patterning of colloidal particles and defects in lamellar soft media *Proc. Natl Acad. Sci. USA* **109** 4744–9
[160] Foster D, Kind C, Ackerman P J, Tai J-S B, Dennis M R and Smalyukh I I 2019 Two-dimensional skyrmion bags in liquid crystals and ferromagnets *Nat. Phys.* **15** 655–9
[161] Ackerman P J, Trivedi R P, Senyuk B, van de Lagemaat J and Smalyukh I I 2014 Two-dimensional skyrmions and other solitonic structures in confinement-frustrated chiral nematics *Phys. Rev.* E **90** 012505
[162] Ackerman P J, Qi Z, Lin Y, Twombly C W, Laviada M J, Lansac Y and Smalyukh I I 2012 Laser-directed hierarchical assembly of liquid crystal defects and control of optical phase singularities *Sci. Rep.* **2** 414–22
[163] Ackerman P J, Qi Z and Smalyukh I I 2012 Optically guided self-assembly of crystalline lattices of torons for defect patterning in liquid crystals and phase of laser beams *Phys. Rev.* E **86** 021703
[164] Fukuda J and Žumer S 2011 Quasi-two-dimensional skyrmion lattices in a chiral nematic liquid crystal *Nat. Commun.* **2** 246
[165] Leonov A O, Dragunov I E, Rößler U K and Bogdanov A N 2014 Theory of skyrmion states in liquid crystals *Phys. Rev.* E **90** 042502
[166] Nych A, Fukuda J, Ognysta U, Žumer S and Muševič I 2017 Spontaneous formation and dynamics of half-skyrmions in a chiral liquid-crystal film *Nat. Phys.* **13** 1215–20
[167] Afghah S and Selinger J V 2017 Theory of helicoids and skyrmions in confined cholesteric liquid crystals *Phys. Rev.* E **96** 012708

[168] Duzgun A, Nisoli C, Reichhardt C J O and Reichhardt C 2020 Commensurate states and pattern switching via liquid crystal skyrmions trapped in a square lattice *Soft Matter* **16** 3338–43

[169] Ackerman P J, van de Lagemaat J and Smalyukh I I 2015 Self-assembly and electrostriction of arrays and chains of hopfion particles in chiral liquid crystals *Nat. Commun.* **6** 6012

[170] Trushkevych O, Ackerman O, Crossland W A and Smalyukh I I 2010 Optically generated adaptive localized structures in confined chiral liquid crystals doped with fullerene *Appl. Phys. Lett.* **97** 201906

[171] Planner J 1861 Note about cholesterol *Ann. Chem. Pharm.* **118** 25–7

[172] Reinitzer F 1888 Beiträge zur Kenntniss des Cholesterins *Monatsh. Chem.* **9** 421–41

[173] Hornreich R M and Shtrikman S Field-induced hexagonal blue phases in positive and negative dielectric anisotropy systems: phase diagrams and topological properties *Phys. Rev.* A **41** 1978–89

[174] Ravnik M, Alexander G P, Yeomans J M and Žumer S 2011 Three-dimensional colloidal crystals in liquid crystalline blue phases *Proc. Natl Acad. Sci. USA* **108** 5188–92

[175] Bogdanov A and Yablonskii D 1989 Thermodynamically stable 'vortices' in magnetically ordered crystals. The mixed state of magnets *Zh. Eksp. Teor. Fiz.* **95** 178–82

[176] Muhlbauer S, Binz B, Jonietz F, Pfleiderer C, Rosch A, Neubauer A, Georgii R and Boni P 2009 Skyrmion lattice in a chiral magnet *Science* **323** 915–9

[177] Yu X, Onose Y, Kanazawa N, Park J H, Han J H, Matsui Y, Nagaosa N and Tokura Y 2010 Real-space observation of a two-dimensional skyrmion crystal *Nature* **465** 901–4

[178] Fert A, Cros V and Sampaio J 2013 Skyrmions on the track *Nat. Nanotechnol.* **8** 152–6

[179] Iwasaki J, Mochizuki M and Nagaosa N 2013 Current-induced skyrmion dynamics in constricted geometries *Nat. Nanotechnol.* **8** 742–7

[180] Schulz T *et al* 2012 Emergent electrodynamics of skyrmions in a chiral magnet *Nat. Phys.* **8** 301–4

[181] Yu X Z 2012 Skyrmion flow near room temperature in an ultralow current density *Nat. Commun.* **3** 988

[182] Zhang X, Ezawa M and Zhou Y 2015 Magnetic skyrmion logic gates: conversion, duplication and merging of skyrmions *Sci. Rep.* **5** 9400

[183] Sohn H R O, Vlasov S M, Uzdin V M, Leonov A O and Smalyukh I I 2019 Real-space observation of skyrmion clusters with mutually orthogonal skyrmion tubes *Phys. Rev.* B **100** 104401

[184] Smalyukh I I, Senyuk B I, Palffy-Muhoray P, Lavrentovich O D, Huang H, Gartland E C Jr, Bodnar V H, Kosa T and Taheri B 2005 Electric-field-induced nematic-cholesteric transition and three-dimensional director structures in homeotropic cells *Phys. Rev.* E **72** 061707

[185] Zhang Q, Ackerman P J, Liu Q and Smalyukh I I 2015 Ferromagnetic switching of knotted vector fields in liquid crystal colloids *Phys. Rev. Lett.* **115** 097802

[186] Mosseri R 2008 Geometrical frustration and defects in condensed matter systems *C. R. Chimie* **11** 192–7

[187] Smalyukh I I, Kaputa D, Kachynski A V, Kuzmin A N, Ackerman P J, Twombly C W, Lee T, Trivedi R P and Prasad P N 2012 Optically generated reconfigurable photonic structures of elastic quasiparticles in frustrated cholesteric liquid crystals *Opt. Express* **20** 6870–80

[188] Durey D, Sohn H R O, Ackerman P J, Brasselet E, Smalyukh I I and Lopez-Leon T 2020 Topological solitons, cholesteric fingers and singular defect lines in Janus liquid crystal shells *Soft Matter* **16** 2669–82

[189] Leonov A O and Inoue K 2018 Homogeneous and heterogeneous nucleation of skyrmions in thin layers of cubic helimagnets *Phys. Rev.* B **98** 054404

[190] Ackerman P J and Smalyukh I I 2017 Diversity of knot solitons in liquid crystals manifested by linking of preimages in torons and hopfions *Phys. Rev.* X **7** 011006

[191] Tai J-S, Ackerman P J and Smalyukh I I 2018 Topological transformations of Hopf solitons realized in chiral ferromagnets and liquid crystals *Proc. Natl Acad. Sci. USA* **115** 921–6

[192] Hopf H 1931 Über die Abbildungen der dreidimensionalen Sphäre auf die Kugelfläche *Math. Ann.* **104** 637–65

[193] Derrick G H 1964 Comments on nonlinear wave equations as models for elementary particles *J. Math. Phys.* **5** 1252–4

[194] Ackerman P J and Smalyukh I I 2016 Reversal of helicoidal twist handedness near point defects of confined chiral liquid crystals *Phys. Rev.* E **93** 052702

[195] Sohn H R O, Voinescu R, Chen Z, Wang Y and Smalyukh I I 2020 Optically enriched and guided dynamics of solitons in chiral liquid crystals *Opt. Express* **28** 6306–19

[196] Sohn H R O and Smalyukh I I 2020 Electrically powered motions of toron crystallites in chiral liquid crystals *Proc. Natl Acad. Sci. USA* **117** 6437–45

[197] Sohn H R O, Liu D and Smalyukh I I 2019 Schools of skyrmions with electrically tunable elastic interactions *Nat. Commun.* **10** 4744

[198] Sohn H R O, Liu C D, Wang Y and Smalyukh I I 2019 Light-controlled skyrmions and torons as reconfigurable particles *Opt. Express* **27** 29055–68

[199] Marchetti M C, Joanny J F, Ramaswamy S, Liverpool T B, Prost J, Rao M and Simha R A 2012 Hydrodynamics of soft active matter *Rev. Mod. Phys.* **85** 1143–89

[200] Vicsek T, Czirók A, Ben-Jacob E, Cohen I and Shochet O 1995 Novel type of phase transition in a system of self-driven particles *Phys. Rev. Lett.* **75** 1226–9

[201] Narayan V, Ramaswamy S and Menon N 2007 Long-lived giant number fluctuations in a swarming granular nematic *Science* **317** 105–8

[202] Decamp S J, Redner G S, Baskaran A, Hagan M F and Dogic Z 2015 Orientational order of motile defects in active nematics *Nat. Mater.* **14** 1110–5

[203] Saw T B *et al* 2017 Topological defects in epithelia govern cell death and extrusion *Nature* **544** 212–6

[204] Kawaguchi K, Kageyama R and Sano M 2017 Topological defects control collective dynamics in neural progenitor cell cultures *Nature* **545** 327–31

[205] Giomi L, Kos Ž, Ravnik M and Sengupta A 2017 Cross-talk between topological defects in different fields revealed by nematic microfluidics *Proc. Natl Acad. Sci. USA* **114** E5771–7

[206] Čopar S, Aplinc J, Kos Ž, Žumer S and Ravnik M 2019 Topology of three-dimensional active nematic turbulence confined to droplets *Phys. Rev.* X **9** 031051

[207] Duclos G *et al* 2020 Topological structure and dynamics of three dimensional active nematics *Science* **367** 1120–4

[208] Smalyukh I I and Lavrentovich O D 2003 Anchoring-mediated interaction of edge dislocations with bounding surfaces in confined cholesteric liquid crystals *Phys. Rev. Lett.* **90** 085503

[209] Mori H and Nakanishi H 1988 On the stability of topologically non-trivial point defects *J. Phys. Soc. Japan* **57** 1281–6

[210] Schopohl N and Sluckin T J 1987 Hedgehog structure in nematic and magnetic systems *Phys. Rev. Lett.* **59** 2582–4

[211] Čopar S and Žumer S 2012 Topological and geometric decomposition of nematic textures *Phys. Rev.* E **85** 031701

[212] Schopohl N and Sluckin T J 1988 Hedgehog structure in nematic and magnetic systems *J. Phys. France* **49** 1097–101

[213] Poulin P and Weitz D 1998 Inverted and multiple nematic emulsions *Phys. Rev.* E **57** 626–37

[214] Wood T A, Lintuvuori J S, Schofield A B, Marenduzzo D and Poon W C K 2011 A self-quenched defect glass in a colloid-nematic liquid crystal composite *Science* **334** 79–83

[215] Loudet J C, Barois P and Poulin P 2000 Colloidal ordering from phase separation in a liquid-crystalline continuous phase *Nature* **407** 611–3
[216] Liu Q, Yuan Y and Smalyukh I I 2014 Electrically and optically tunable plasmonic guest-host liquid crystals with long-range ordered nanoparticles *Nano Lett.* **14** 4071–7
[217] Woltman S J, Jay D G and Crawford G P 2007 Liquid-crystal materials find a new order in biomedical applications *Nat. Mater.* **6** 929–38
[218] Koenig G M, Lin I-H and Abbott N L 2010 Chemo-responsive assemblies of microparticles at liquid crystalline interfaces *Proc. Natl Acad. Sci. USA* **107** 3998–4003
[219] Pandey M B, Porenta T, Brewer J, Burkart A, Čopar S, Žumer S and Smalyukh I I 2014 Self-assembly of skyrmion-dressed chiral nematic colloids with tangential anchoring *Phys. Rev.* E **89** 060502(R)
[220] Porenta T, Čopar S, Ackerman P J, Pandey M B, Varney M C M, Smalyukh I I and Žumer S 2014 Topological switching and orbiting dynamics of colloidal spheres dressed with chiral nematic solitons *Sci. Rep.* **4** 7337
[221] Mundoor H, Senyuk B and Smalyukh I I 2016 Triclinic nematic colloidal crystals from competing elastic and electrostatic interactions *Science* **352** 69–73
[222] Petit-Garrido N, Trivedi R P, Ignes-Mullol J, Claret J, Lapointe C, Sagues F and Smalyukh I I 2011 Healing of defects at the interface of nematic liquid crystals and structured Langmuir–Blodgett monolayers *Phys. Rev. Lett.* **107** 177801
[223] Petit-Garrido N, Trivedi R P, Sagués F, Ignés-Mullol J and Smalyukh I I 2014 *Soft Matter* **10** 8163–70
[224] Martinez A and Smalyukh I I 2015 Light-driven dynamic Archimedes spirals and periodic oscillatory patterns of topological solitons in anisotropic soft matter *Opt. Express* **23** 4591–604
[225] Liu Q, Ackerman P J, Lubensky T C and Smalyukh I I 2016 Biaxial ferromagnetic liquid crystal colloids *Proc. Natl Acad. Sci. USA* **113** 10479–84
[226] Mundoor H, Park S, Senyuk B, Wensink H and Smalyukh I I 2018 Hybrid molecular-colloidal liquid crystals *Science* **360** 768–71
[227] Ranganath G S 1998 On defects in biaxial nematic liquid crystals *Curr. Sci.* **57** 1–6
[228] Needleman D and Dogic Z 2017 Active matter at the interface of materials science and cell biology *Nat. Rev. Mater.* **2** 1–14
[229] Smalyukh I I, Butler J, Shrout J D, Parsek M R and Wong G C L 2008 Elasticity-mediated nematic-like bacterial organization in model extracellular DNA matrix *Phys. Rev.* E **78** 030701(R)
[230] Peng C, Turiv T, Guo Y, Wei Q-H and Lavrentovich O D 2016 Command of active matter by topological defects and patterns *Science* **354** 882–5
[231] Bukusoglu E, Pantoja M B, Mushenheim P C, Wang X and Abbott N L 2016 Design of responsive and active (soft) materials using liquid crystals *Annu. Rev. Chem. Biomol. Eng.* **7** 163–96
[232] Dhakal N P, Jiang J, Guo Y and Peng C 2020 Self-assembly of aqueous soft matter patterned by liquid-crystal polymer networks for controlling the dynamics of bacteria *ACS Appl. Mater. Interfaces* **12** 13680–5
[233] Doostmohammadi A, Ignés-Mullol J, Yeomans J M and Sagués F 2018 Active nematics *Nat. Commun.* **9** 1–13
[234] Shankar S, Bowick M J and Marchetti M C Topological sound and flocking on curved surfaces *Phys. Rev.* X **7** 031039
[235] Shnir Y M 2018 *Topological and Non-topological Solitons in Scalar Field Theories* (Cambridge: Cambridge University Press)
[236] McConney M E, Martinez A, Tondiglia V P, Lee K M, Langley D, Smalyukh I I and White T J 2013 Topography from topology: photoinduced surface features generated in liquid crystal polymer networks *Adv. Mater.* **25** 5880–5
[237] Ware T H, McConney M E, Wie J J, Tondiglia V P and White T J 2015 Voxelated liquid crystal elastomers *Science* **347** 982–4
[238] Gelebart A H, Mulder D J, Varga M, Konya M, Vantomme G, Meijer E W, Selinger R L B and Broer D J 2017 Making waves in a photoactive polymer film *Nature* **546** 632–6
[239] Silvestre N M, Liu Q, Senyuk B, Smalyukh I I and Tasinkevych M 2014 Towards template-assisted assembly of nematic colloids *Phys. Rev. Lett.* **112** 225501
[240] Senyuk B I, Smalyukh I I and Lavrentovich O D 2005 Switchable two-dimensional gratings based on field-induced layer undulations in cholesteric liquid crystals *Opt. Lett.* **30** 349–51
[241] Varanytsia A, Posnjak G, Mur U, Joshi V, Darrah K, Muševič I, Čopar S and Chien L-C 2017 Topology-commanded optical properties of bistable electric-field-induced torons in cholesteric bubble domains *Sci. Rep.* **7** 16149
[242] Hess A J, Poy G, Tai J-S B, Žumer S and Smalyukh I I 2020 Control of light by topological solitons in soft chiral birefringent media *Phys. Rev.* X **10** 031042
[243] Assanto G, Minzoni A A and Smyth N F 2014 Deflection of nematicon-vortex vector solitons in liquid crystals *Phys. Rev.* A **89** 013827
[244] Sutcliffe P 2018 Hopfions in Chiral Magnets *J. Phys. A: Math. Theor.* **51** 375401 https://iopscience.iop.org/article/10.1088/1751-8121/aad521